SURFACE FLUX MEASUREMENTS BY EDDY COVARIANCE OVER A BLACK SPRUCE STAND

Jonathan M. Massheder

Doctor of Philosophy

University of Edinburgh

February 1999

Declaration

I declare that this thesis has been composed by myself and has not been submitted in any previous application for a degree. The work described is my own except where stated otherwise.

Jonathan M. Massheder

February 1999.

ABSTRACT

A "real-time" eddy covariance (EC) system (*EdiSol*) was developed to measure fluxes of CO_2, momentum, sensible heat and latent heat of a boreal black spruce stand as part of the BOReal Ecosystem-Atmosphere Study (BOREAS). BOREAS is a multi-scale study using satellites, aircraft, tower and leaf-scale measurements over the major vegetation types of the Canadian boreal forest. The measurements reported in this thesis are an essential component of BOREAS being the stand scale (tower) measurements over one of the major vegetation types.

EdiSol uses a commercially available three-axis ultrasonic anemometer and a closed path infrared gas analyser (air is ducted from close to the anemometer to the optical bench). Software was written to acquire the output data from the anemometer and gas analyser and concurrently calculate CO_2, water vapour, momentum, sensible heat and latent heat fluxes. The high frequency, primary, data is stored for further analysis. The calculations made by the software and the instruments and their connection are described. The corrections for frequency response of the system and tests of the software output are presented.

The observations were made from 25 March to 28 November 1996 over the black spruce stand. There was no CO_2 assimilation when soil temperature at 5 cm and 10 cm depth was less than *ca* 0 °C (corresponding to an air temperature of –3 °C on average). Under these conditions, carbon exchange averaged 0.8 g C m^{-2} day^{-1} (0.77 μmol CO_2 m^{-2} s^{-1}). Mean half-hourly net ecosystem flux reached –14 μmol m^{-2} s^{-1} in June during the day and 10 μmol m^{-2} s^{-1} at night when the atmosphere was well mixed ($u_* > 0.4$ m s^{-1}). The optimum temperature for CO_2 assimilation was 30 °C, close to the maximum air temperature observed at 26 m. When the soil temperature above 10 cm depth was less than 0 °C assimilation was zero but quantum efficiency of assimilation (α) reached 0.066 in July. Assimilation followed photosynthetic photon flux density (PPFD) closely when $\alpha > 0.0$ and decreased when vapour pressure deficit (VPD) exceeded 1.3 kPa. Temperature was the limiting environmental variable over the year. Respiration estimated from night fluxes when $u_* > 0.4$ m s^{-1} showed an exponential response to temperature that differed with

season. Storage of CO_2 in the air below the EC sensors did not account adequately for respiration on nights with stable conditions so respiration on such nights was modelled. The CO_2 exchange from 29 November 1995 to 25 March 1996 was not measured and was also modelled. The annual carbon exchange from 29 November 1995 to 28 November 1996 was -15 gC m^{-2} (uptake by the surface) and 271 mm of water were evaporated.

The albedo showed little seasonal variation with values of 0.2 when there was some snow on the trees and 0.1when there was not. Net longwave radiation in cloudless conditions was consistently *ca* –200 W m^{-2} (lost from the surface). Net radiation was 73 % of incoming shortwave radiation or 80 % of net shortwave radiation with a root mean squared error of 23.0 and 22.5 W m^{-2} respectively. The energy balance closure on a half-hour basis was good, $(H + \lambda E) / (R_n - G - S - B) = 0.94$, except under stable conditions at night and the daytime closure was also improved by excluding observations when $u_* < 0.4$ m s^{-1}. The mid-day Bowen ratios varied from 16 when the system was frozen in March to 1.0 in July but were typically 1.0 to 2.5 from the beginning of May to the end of September. Storage of latent and sensible heat in the air below the EC sensors was negligible. Heat storage in the biomass was the largest component after sensible and latent heat fluxes and on a half-hour basis accounted for 3 % of the energy balance over the whole period and 10 % when the stand was warming or cooling at the beginning and end of the day

Contents

Acknowledgements

I would like to thank my supervisors Prof. Paul Jarvis and Dr. John Moncrieff for their help and support and giving me the opportunity to pursue this study. Thanks also to my colleagues: Peter McCracken, Sophie Hale, Steven Scott, and Mark Rayment for help and comradeship directly involved with this work, to Peter Levy, Bart Kruijt, Ford Cropley, Yadvinder Malhi, Mike Perks, Andrew Morse and Dennis Lousteau for help maintaining the Old Black Spruce site. Thanks also to Craig Barton my office mate of many years for putting up with me for so long and his different and sometimes similar points of view.

Thanks to Sophie Hale for the work she did in putting the 1994 weather station together, calibrating the weather station sensors, and typing a proportion of the equations I have used in this thesis. The weather station was extended in 1996 by Mark Rayment who also designed and maintained the profile systems. Thanks to Steve Scott for designing and building EdiBox, supplying the EdiBox gas flow diagram and his support during fieldwork. Thanks also to my father, Peter Massheder, for help with proof-reading.

Chapter 1 Introduction and aims

1.1 Background

Global air temperature has increased by ~0.5 °C over the last 100 years (Jones, 1994; Nicholls *et al.*, 1996). The increase in global temperature has been caused by the absorption of long wave radiation by the atmosphere that, in turn, radiates energy as long wave radiation back to the surface. This positive forcing has increased with increased concentrations of "greenhouse gases" (Houghton *et al.*, 1990). Energy input to the surface has been increased by 1.56, 0.5 and 0.1 W m^{-2} by the principal "green house gases" CO_2, CH_4 and NO_2, respectively, since pre-industrial times to the present (Houghton *et al.*, 1995). The increase in global concentration driving the forcing by CO_2 is from 280 μmol mol^{-1} in pre-industrial times to 360 μmol mol^{-1} at present caused by the burning of fossil fuels (Conway *et al.*, 1994).

Besides an increase in average global temperature, the change in radiative forcing will cause local effects. One of these predicted local effects is enhanced heating of the mid to high latitudes (45 to 65 degrees N) coinciding with the boreal forest biome (Mitchell, 1983). Warming and drying could modify the composition and functioning of the boreal forest (Davis and Botkin, 1985; Solomon and Webb, 1985).

Given the importance of CO_2 in the radiative forcing of the earth's climate it is vital that controls of atmosphere CO_2 concentrations are understood. Evidence from the global CO_2 monitoring network indicate that there may be a sink of CO_2, as yet not identified, in the mid-latitudes of the northern hemisphere (Tans *et al.*, 1990). The boreal forest biome is a possible site of this "missing" sink and in any case, its role in the global carbon and energy cycles may be important to our understanding and prediction of global change.

1.2 BOREAS

The BOReal Ecosystem-Atmosphere Study (BOREAS) is an international study of the exchanges of radiative energy, sensible heat, water, CO_2 and trace gases between the boreal forest and the lower atmosphere. The overall objective of BOREAS is to

improve our understanding of the important processes controlling these exchanges, thereby improving predictions of the effects of global change, principally altered temperature and precipitation patterns, on the biome. The principal issues addressed are (Sellers *et al.*, 1995):

- Sensitivity of the boreal forest biome to changes in the physical climate system.
- The sensitivity of the carbon cycle to environmental change.
- Biophysical feedbacks on the physical climate system. Albedo, surface roughness and the biophysical control of evapotranspiration may have feedback effects on temperature, humidity, precipitation and cloudiness.

BOREAS is a multi-scale study as were previous field studies, e.g. FIFE (*Sellers et al.*, 1992) and HAPEX-Sahel (Goutorbe *et al.*, 1994) where satellite, airborne, stand scale and leaf scale observations were made.

A *region* 1000 km by 1000 km in central Canada was chosen encompassing the southern and northern boundaries of the boreal forest (Figure 1-1). Inside this *region* two study areas were selected one in mid-Saskatchewan at the southern edge of the boreal forest and another in northern Manitoba at the northern edge, to allow the investigation of the variables determining these boundaries.

Major vegetation types were identified in each study area: black spruce *(Picea mariana)*, jack pine *(Pinus banksiana)* and fen in the north and black spruce, jack pine, fen and aspen *(Populus tremuloides)* in the south. Stands of each of these types (including both young and mature stands of jack pine and aspen) have been selected for measurement of surface fluxes using tower-mounted eddy covariance systems in both Northern and Southern Study Areas. At these sites, a Tower Flux (TF) group measured the stand scale fluxes between the vegetation and the lower atmosphere using eddy covariance. Also at these sites, and some auxiliary sites, Terrestrial Ecology (TE), Hydrology (HYD) and Trace Gas Biochemistry (TGB) worked to characterise ecological processes within the stands.

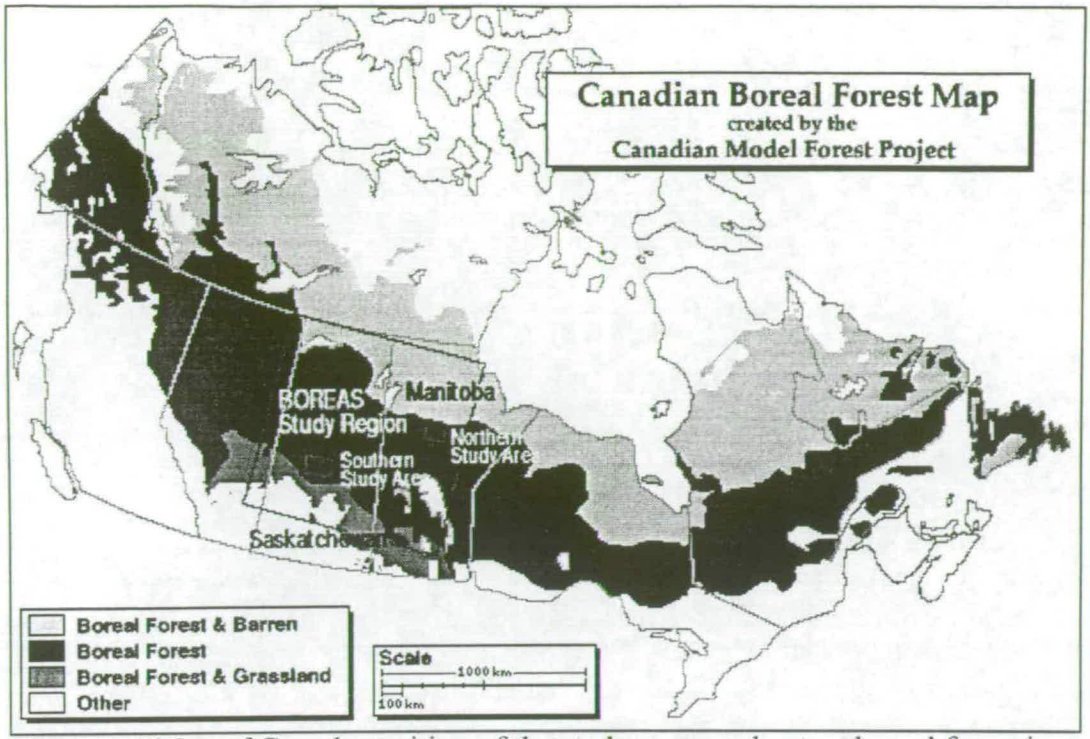

Figure 1-1 Map of Canada position of the study areas and extent boreal forest in Canada.

Aircraft Flux and Meteorology (AFM) groups used aircraft to measure large area surface-atmosphere fluxes with footprints encompassing a mixture of vegetation types within the region. Flux measurements made using aircraft mounted sensors were compared with those measured using tower-mounted sensors.

Satellite, airborne and surface data were used to link surface processes and states to remotely sensed data to increase the usefulness of satellite data in extrapolations to regional and global scales.

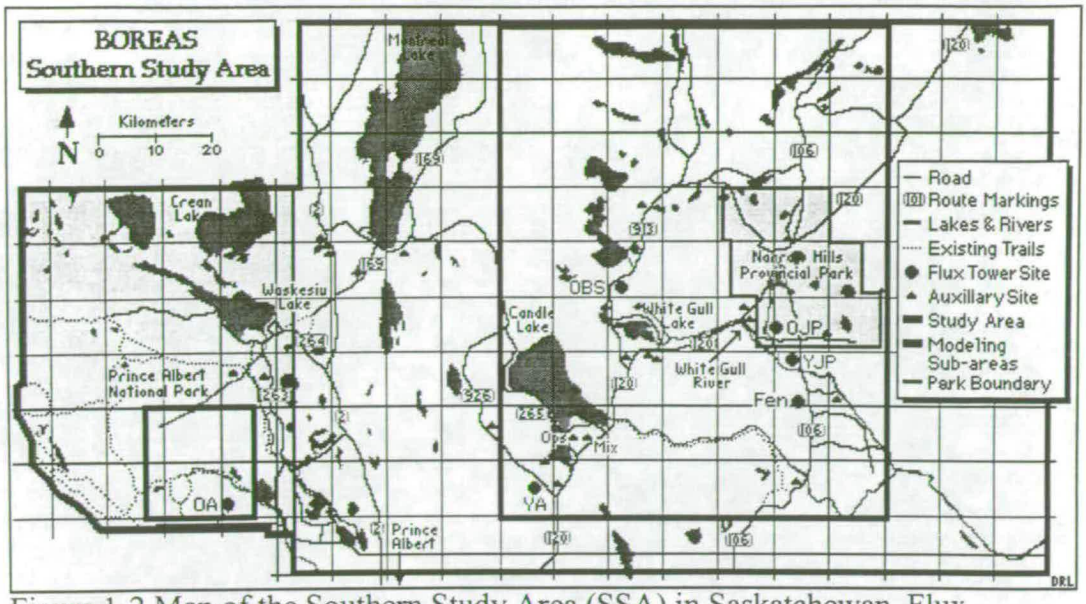

Figure 1-2 Map of the Southern Study Area (SSA) in Saskatchewan. Flux Tower Sites are: Old Aspen (OA), Young Aspen (YA), Old Black Spuce (OBS), Fen, Old Jack Pine (OJP) and Young Jack Pine (YJP).

1.3 General objectives

The major objectives of BOREAS were:

1. to measure and model the exchanges of radiation, heat, CO_2, water vapour and trace gases between the boreal forest and the atmosphere,
2. to determine the controls of these exchange processes,
3. to develop and test remote sensing techniques,
4. to improve understanding of global scale processes with improved understanding of the local scale.

My objectives as part of BOREAS were items 1. and 2. in relation to the exchanges of radiation, heat, CO_2 and water vapour between the forest and atmosphere for one of the major vegetation types at the Southern Study Area Old Black Spruce site (SSA OBS).

1.4 Specific Objectives

The specific objectives in doing the work described in this thesis were:

- to design and implement an eddy covariance system to measure the fluxes of sensible and latent heat, CO_2, water vapour and momentum between the surface and the atmosphere,
- to use this system at SSA OBS to measure those fluxes, together with radiation fluxes, other heat fluxes, temperature, humidity and wind velocity,
- and to examine the measurements to elucidate controls of the meteorological and physiological processes.

1.5 Thesis structure

Chapter 1 is this chapter. It introduces the overall problem of global change and BOREAS, a large international study devised to investigate the role of boreal forest in the global energy and carbon cycles. Also described are the specific aims in producing this thesis and how the work is a component of BOREAS.

Chapter 2 describes the topography, vegetation and turbulence characteristics of the experimental site. The instrumentation used to make the measurements is also described with the theory behind the eddy covariance measurements.

Chapter 3 describes the design and implementation of the eddy covariance flux measuring system: EdiSol.

Chapter 4 shows the processing of covariance data obtained from EdiSol. Routine corrections to the output of EdiSol are presented with some data quality tests.

Chapter 5 is the analysis of the CO_2 flux and evaporation data in respect to its sensitivity to environmental variables and arrives at an estimate of an annual carbon and water vapour exchange for the study site.

Chapter 6 describes the energy and radiation balance at the study site. The sizes of the energy balance components are compared. The energy balance closure, meteorological resistances to the energy (heat) fluxes and partitioning between sensible and latent heat fluxes are examined. In addition, the relationships between radiation fluxes are described with the solar radiation and photon reflectances.

Chapter 7 concludes this thesis with conclusions and recommendations for further study.

Chapter 2 Site and instrumentation

2.1 Introduction

This chapter describes the background theory, the experimental site and instrumentation used in this study. The first section deals with the meteorological theory for measuring exchanges between the surface and the atmosphere. The structure of the atmospheric boundary layer (ABL) is introduced with the equation for the conservation of an atmospheric scalar quantity. The equation for eddy covariance is derived and the assumptions underpinning it are explored. Scaling up from a point measurement to an areal average is discussed. The surface fluxes depend on the vegetation and soil but also on the aerodynamic properties of the surface and these are described. Finally, the eddy covariance, CO_2 and water vapour concentration profiles systems and weather station are described.

2.2 Theory

2.2.1 Atmospheric boundary layer

Measurements of surface fluxes are made in the atmospheric boundary layer (ABL) and its structure determines how the fluxes are measured. The ABL can be divided into two layers: the outer and inner (surface) layers (Figure 2-1) (Garratt, 1992). The outer layer is influenced by the Coriolis force (the apparent force caused by the rotation of the earth) but influences by the surface are small. In contrast, the converse is true for the inner layer where the major influence is by the surface (by momentum exchange and surface heating). The inner layer can then be sub-divided into the roughness (interfacial) layer, which is within and just above the roughness elements, and the constant flux (inertial) layer where the shearing stress (momentum flux) is roughly constant. During the day surface forcing by heating and momentum exchange causes turbulence and the inner layer extends up to over 1 km in height. Under these conditions the inner layer is also called the mixed layer (Stull, 1988). At night, the bottom of the inner layer is chilled by the radiatively cooled surface and a temperature inversion occurs when the temperature decreases towards the ground

and the bottom of the inner layer becomes the stable boundary layer. The height of the stable boundary layer is much lower than the mixed layer and maybe only about 500 m. When dealing with surface fluxes it is the surface (or inner) layer with which we are concerned.

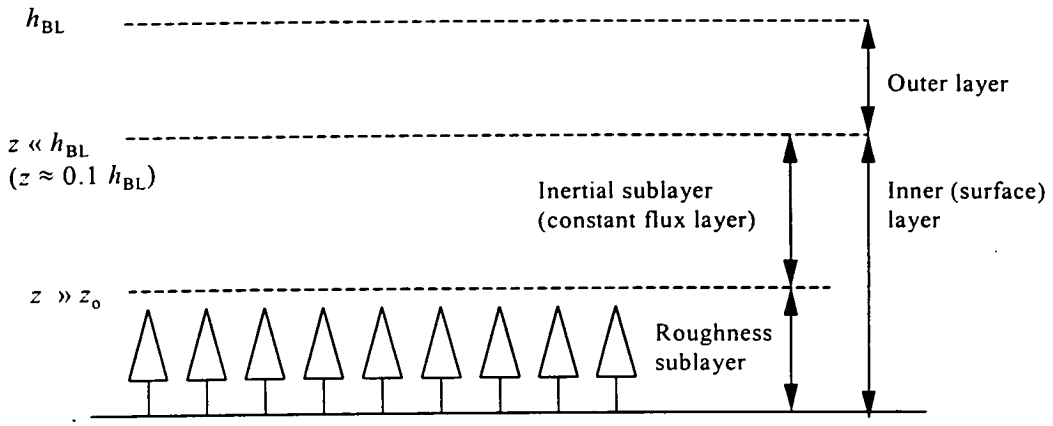

Figure 2-1 Structure of the atmospheric boundary layer for an aerodynamically rough surface (e.g. forest), where z is height, h_{BL} is the height of the atmospheric boundary layer and z_o is the aerodynamic roughness length (after Garratt, 1992).

The friction at the surface causes the wind speed to decrease towards the ground by momentum exchange resulting in a semi-logarithmic mean wind speed profile described by:

$$u(z) = \left(\frac{u_*}{k}\right) \cdot \ln\left(\frac{z-d}{z_o}\right)\phi_M \qquad (2\text{-}1)$$

where $u(z)$ is the wind speed (u) at height (z), k is the von Karman constant (0.41), ϕ_m is an empirical stability correction factor and equals 1 in neutral conditions, u_* is the friction velocity, which is related to the momentum flux, τ, by $u_* = -(\tau/\rho)^{1/2}$, d is the zero plane displacement, ρ is the density of moist air and z_o is the aerodynamic roughness length (Monteith and Unsworth, 1990). The parameters d and z_o describe the aerodynamics of the surface. Over short vegetation d approaches zero and z_o is the height above the surface at which the mean horizontal wind speed extrapolates to zero. Over tall vegetation, mean horizontal wind speed extrapolates to zero at height $z_o + d$.

2.2.2 Conservation of a scalar quantity

Surface fluxes of CO_2, water vapour and sensible heat are a function of the sink/source strength and transport efficiency. To examine these fluxes we use the law of conservation of a scalar quantity as a framework.

The conservation of mass equation for a scalar quantity for a control volume expressed in molar terms adapted from Stull (1988) is:

$$\mathbf{S} = \frac{\partial \overline{\chi}}{\partial t} + \sum_{i=1}^{3} \frac{\partial \overline{u_i \chi}}{\partial x_i} + D \sum_{i=1}^{3} \frac{\partial^2 \chi}{\partial x_i^2} \qquad (2\text{-}2)$$

where $\mathbf{S}$ is the volumetric sink/source strength, χ is the molar ratio of a chemical constituent, t is time, u_i is the wind velocity component in the orthogonal directions x_i (i = 1, 2 ,3) and D is a diffusion coefficient. The first term on the RHS is the rate of change of concentration (moles per volume) of the chemical constituent, the second is the airflow flux divergence/convergence and the third is the diffusive flux divergence/convergence. When the flux into the volume is greater than the flux out, the flux is said to converge, and conversely, when the flux in to the volume is less then the flux out, the flux is said to diverge.

If the hypothetical control volume is applied to a forest, the lower surface of the volume is the interface between vegetation/soil and free air. The volume then contains air only and there is no sink or source for the scalar quantity in the volume assuming no changes in atmospheric chemistry of the scalar. At the interface between vegetation/soil and free air, turbulence is inhibited and the exchange is by diffusion across large concentration gradients. Away from this interface, turbulent transport is several orders of magnitude greater than that by molecular diffusion (concentration gradients are small) (Businger, 1986) and transport by molecular diffusion is negligible. The control volume occupies the roughness layer but should extend vertically into the constant flux layer above any sink or source (except air) to capture all exchange between surface and atmosphere.

Because we have defined the sink/source to be outside the volume $\mathbf{S} = 0$, and assuming that there is no horizontal flux divergence (i.e. no horizontal advection) we can integrate equation (2-2) to give:

$$D_0 = \int_{z=0}^{z_m} \frac{\partial \overline{\chi}}{\partial t} dz + \overline{w\chi} \quad (2\text{-}3)$$

where D_0 is the diffusive flux at the vegetation/soil and free air interface, z is height, z_m is the measurement height and w is the vertical windspeed (Moncrieff *et al.*, 1996). The first term on the RHS is the storage term and can be estimated by measuring concentration profiles. The second term on the RHS is the vertical flux where the transport is airflow (turbulent and advective) in kinematic units (flux divided by the air density) and can be estimated by eddy covariance (turbulent flux) plus Webb, Pearman and Leuning (1980) (WPL) corrections. WPL corrections are an estimate of the advective flux (carried by a non-zero vertical windspeed) caused by the transport of heat and by evaporation (see section 2.2.3.1 *Derivation of eddy covariance*).

2.2.3 Eddy covariance theory

Eddy covariance is a technique used to estimate fluxes to and from the surface and the atmosphere of sensible heat, latent heat (water vapour) and CO_2. A flux is a rate of flow of mass or energy per unit cross-sectional area normal to the flow. When measuring exchange between the surface and the atmosphere none of the flux component along the surface should be included. Therefore, the desired flux (between the surface and atmosphere) is normal to the streamlines, which may not be horizontal.

Eddy fluxes (fluxes as measured by eddy covariance) are functions of turbulence. When turbulence is high, other methods of transport may be negligible and eddy covariance will then estimate the surface fluxes closely. However, if turbulence is low other transports, or storage, must be taken into account (see section 2.2.2: *Conservation of a scalar quantity*).

2.2.3.1 Derivation of eddy covariance

Following Swinbank (1951) the instantaneous flux at a point in space and time, F, of a scalar quantity in fluid, is given by the velocity of the fluid, U, and the partial density, ρ, of the quantity in that fluid at that point i.e.

$$F = U\rho \qquad (2\text{-}4).$$

The axes, x, y, and z are usually defined in the horizontal and vertical for the sake of simplicity. Here, they are defined with the x y plane as parallel to the streamlines, not necessarily horizontal, and z as perpendicular to this plane. For fluxes perpendicular to the streamlines, F_w, we use the perpendicular component of the wind velocity, w,

$$F_w = w\rho \qquad (2\text{-}5).$$

Instantaneous point fluxes are continuously variable in time and space. The time averaged perpendicular flux at a point, F_w, is given by,

$$\overline{F}_w = \frac{\int_{t=t_1}^{t_2} w\rho.dt}{t_2 - t_1} \qquad (2\text{-}6).$$

A time averaged flux may be approximated by the mean of a time series of discrete samples, where an overbar denotes such a mean,

$$\overline{F}_w = \overline{w\rho} \qquad (2\text{-}7).$$

If we separate the mean and fluctuating parts (Reynolds averaging, which is a technique often used in meteorology so that properties of the mean wind and turbulent events can be separated) denoting fluctuations from the mean with the symbol " ' ", we get,

$$\overline{F}_w = \overline{(w' + \overline{w})(\rho' + \overline{\rho})} \qquad (2\text{-}8)$$

because $\overline{w'} = 0$ and $\overline{\rho'} = 0$:

$$\overline{F}_w = \overline{w}\,\overline{\rho} + \overline{w'\rho'} \qquad (2\text{-}9).$$

Now it is tempting to assume that $\overline{w} = 0$ on the basis that there can be no net vertical movement of air near the surface over a reasonably long period, so

$$\overline{F}_w = \overline{w'\rho'} \qquad (2\text{-}10).$$

Hence the term eddy covariance as $\overline{w'\rho'} = \overline{(w-\overline{w})(\rho-\overline{\rho})}$ is the covariance of w and ρ.

In deriving equation (2-10), we introduced two sources of possible error:

i) approximating an integral of a continuous variable with the sum of discrete samples of that variable,

ii). on assuming that $\overline{w} = 0$.

The approximation of an integral with a sum of discrete samples is a numerical integration problem. The accuracy of the approximation depends on the resolution of the discrete samples. In this case we are dealing with a time series and the resolution depends on the sampling frequency. The higher the sampling frequency the better the approximation as more of the variation is included. This problem can be investigated using spectral analysis and theory based on dimensional analysis, e.g Kaimal *et al.* (1972) showed that good approximations can be made with quite low sample frequencies between (10 and 20 Hz) as very little variation occurs at high frequencies. Variation at high frequencies is low as fluctuations occur over small distances at which friction between molecules becomes increasingly important. However, with slow response instrumentation, covariance is underestimated and that this must be taken into account when estimating fluxes (Moore, 1986).

The inaccuracy caused by assuming that $\overline{w} = 0$ can be investigated by using sensitivity analysis. Let us assume that: $\overline{w} = 1$ mm s^{-1}; CO_2 concentration, c, = 360 μmol mol^{-1} which gives a partial density of 15 mmol m^{-3} at STP; vapour pressure, *e*, = 1 kPa which gives 411 mmol m^{-3} at STP and an air temperature of 293 K (20 °C) gives a heat density of 356 kJ m^{-3} at STP with dry air. The resulting advective fluxes $\overline{w}\overline{\rho}$ are then: CO_2 flux of 15 μmol m^{-2} s^{-1}; water vapour flux of 0.41 mmol m^{-2} s^{-1} and a sensible heat flux of 356 W m^{-2}. The values for CO_2 and sensible heat fluxes are typical large values but for water vapour, it is 10% of a typical daytime flux. This

analysis shows that a low vertical windspeed, well below the resolution of today's sonic anemometers (which have offsets or errors in measuring zero of about 1 cm s^{-1}), would cause large advective fluxes (less so with water vapour).

Two surface processes that cause a non-zero mean vertical windspeed are sensible heat flux and evaporation. Evaporation is a source of gas and as air molar density remains constant, vertical windspeed is enhanced. Sensible heat flux enhances vertical windspeed because a larger volume of warmer air is displaced by a smaller volume of colder air of equal mass. The warmer air is of greater volume and so must travel faster than the cold air causing a net vertical windspeed. Changes to the partial densities of scalars also occur, coupled with this inducement of vertical windspeed.

The effects of sensible heat flux and evaporation on eddy covariance measurements that assume $\overline{w} = 0$ was investigated by Webb, Pearman and Leuning (1980). They showed that sensible heat flux could cause CO_2 fluxes of about 50% of those estimated by pure eddy covariance ($F = \overline{w'\rho'}$) and evaporation could cause CO_2 fluxes of about 10% of those estimated by pure eddy covariance. The vertical wind caused by sensible heat flux and/or evaporation can be ignored, however, if the corresponding fluctuations in partial density of the scalar are removed, so:

$$F = \overline{w'\rho'_{cor}} \qquad (2\text{-}11)$$

where ρ_{cor} is the scalar partial density at constant temperature and humidity (Leuning and Judd , 1996).

2.2.3.2 Measuring surface fluxes by eddy covariance

Eddy covariance sensors measure over a small volume not at an infinitesimal point because sensors have a finite size. The errors in measuring over a small volume must be taken into account when estimating point fluxes and micrometeorological theory must be used to extrapolate from the point fluxes to a more useful area flux estimate.

The surface fluxes we are interested in are those between the surface and the atmosphere which are, by definition, across the stream lines. The orientation of the stream lines depend on the slope of the surface and often vary with wind direction whereas the anemometer is fixed in position. Rearranging the co-ordinate reference is a geometric transformation introduced to cope with this and is described in Chapter 3.

2.2.3.3 Area flux estimates from point fluxes estimates.

The estimates required are of mean fluxes over a given area, i.e. over a certain surface type. Areal averaging could be achieved by sampling at an appropriate number of points, however, the cost of equipment is prohibitive and areal averages can be estimated by assuming Taylor's (1938) hypothesis of "frozen turbulence" and measuring over a homogenous surface.

Taylor's hypothesis suggests that assuming turbulence is "frozen" as it advects passed the sensor, i.e. the properties of eddies do not change significantly, measuring at a point for a certain time interval is equivalent to instantly measuring at all the points upwind of the sensor, over the distance it takes air to travel during that time interval. If turbulent intensity is high because of high wind shear such as is often the case inside plant canopies Taylor's hypothesis fails. In addition, over a heterogeneous surface, spatial variations that are not represented by a time series measured at one point invalidate the hypothesis.

2.2.3.4 Areal averaging – flux footprint

The eddy flux measured is a function of the surface fluxes and the transport for some area upwind of the sensors where the surface is the interface between soil/vegetation and air. The flux footprint function maps the point eddy flux measurement to the surface fluxes and is essentially a probability distribution (Leclerc and Thurtel, 1989; Schuepp *et al.*,1990; Horst and Weil, 1992;). Following Schuepp *et al.* (1990) the eddy flux density, F_D, is a function of distance upwind, x,

$$F_D = -\frac{2x_{max}\phi_m}{x^2} \cdot e^{-2x_{max}\phi_m / x} \qquad (2\text{-}12)$$

where x_{max} is the distance to the maximum relative flux density given by:

$$x_{max} = \frac{\bar{u}(z-d)}{2u_*k}\phi_m \qquad (2\text{-}13)$$

$\bar{u}$ is the average wind speed in the layer between the measurement height and the surface, calculated as:

$$\bar{u} = \frac{u_*[\ln((z-d)/z_o) - 1 + z_o/(z-d)]}{k(1 - z_o/(z-d))} \qquad (2\text{-}14)$$

The published flux footprint models do not hold in very stable conditions (generally at night when sensible heat flux, H, ≤ 0), however, when the mixing process is very slow and the flux footprint becomes very long for most of the time. In these conditions mixing is sporadic and gusts of wind will cause a very short lived flux which will contribute almost all the time averaged measured eddy flux. This heterogeneity violates Taylor's hypothesis and the point measurement cannot be assumed to represent the flux over a large area, i.e. the foot print of the measurement is very small.

As described in section 2.2.3.4 the eddy flux is a result of surface fluxes and the transport. In unstable conditions (daytime) most of the flux measured resulting from surface fluxes relatively near the tower the eddy flux is then influenced by surfaces fluxes more distant than that less and less. The footprint was estimated for a range of windspeeds and sensible heat fluxes for the eddy covariance system at Southern Study Area (SSA) Old Black Spruce site (OBS) (measurement height of 26 m with the canopy displacement height of 4.5 m and roughness length of 1.03 m calculated from profiles of mean wind speed and momentum flux (Hale, 1996). Figure 2-2 shows the footprint estimate for a windspeed of 2 m s^{-1} and sensible heat flux of 100 Wm^{-2}. For these conditions, the maximum proportion of the flux is estimated to be 60 m upwind from the tower, 80% of the eddy flux to have come from with 445 m and 90% from with 1200 m.

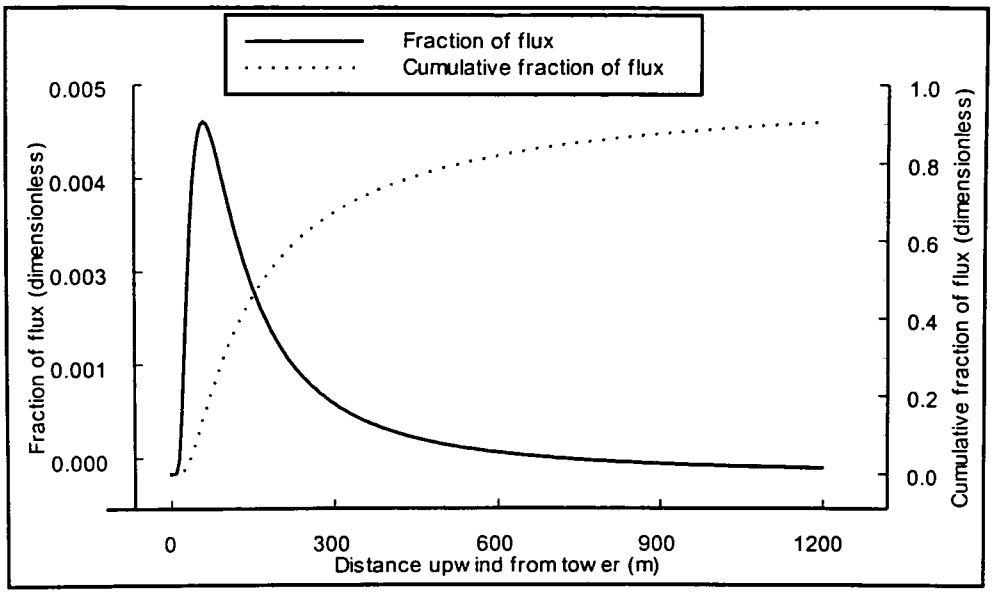

Figure 2-2 "Footprint" for the eddy covariance system at 26 m, with the canopy displacement height of 4.5 m and roughness length of 1.03 m with a windspeed of 2 m s^{-1} and a sensible heat flux of 100 W m^{-2}. For these conditions the maximum proportion of the flux is estimated to be 60 m upwind from the tower, 80% of the eddy flux to have come from with 445 m and 90% from with 1200 m.

Table 2-1 and 2-2 show the distance to the peak contribution to the eddy flux and distance within which 80 % of the flux comes from, respectively. For the range of windspeeds and sensible heat fluxes that the footprint was estimated for (windspeed: 0.5, 1, 2, 4, 6 and sensible heat flux: 0.1, 50, 100..400), the minimum distance to the peak was estimated to be 15 m at low wind speed, and large sensible heat flux and the maximum 140 m, with very small but positive sensible heat flux and high windspeed. Nocturnal footprints when sensible heat flux may be negative were not estimated. Similarly, the distance within which 80 % of the eddy flux comes 130 m at very low wind speed and high sensible heat flux, and 1250 m for approximately zero sensible heat flux and high windspeed. The maximum distance within which 80 % of the flux is produced approaches a symptotic value at a windspeed of 4 m s^{-1} of 1250 m and for 95 % of the flux this value is 5200 km. Therefore, under any conditions 80 % of the flux will come from an approximate homogenous surface.

u \ H	0.1	50	100	150	200	250	300	350	400
0.5	107.6	25.3	21.3	19.2	17.9	16.9	16.2	15.6	15.1
1	133.0	42.5	35.8	32.3	30.1	28.5	27.2	26.2	25.3
2	139.1	70.5	59.7	54.1	50.4	47.7	45.6	43.9	42.5
4	140.0	108.0	95.4	87.8	82.5	78.5	75.3	72.7	70.5
6	140.1	125.7	116.6	110.1	105	100.1	97.6	94.7	92.2

Table 2-1 Distances to the peak contribution to the eddy flux for the SSA OBS calculated using equation 2-6. The results are for a range of sensible heat flux, H (W m^{-2}), and windspeed, u (m s^{-1}), values and z =26 m, d = 4.5 and z_0=1.03.

u \ H	0.1	50	100	150	200	250	300	350	400
0.5	960	220	185	170	155	145	140	135	130
1	1185	375	315	285	265	250	240	230	220
2	1240	625	530	480	445	425	405	390	375
4	1250	965	850	780	735	700	670	645	625
6	1250	1120	1040	980	935	900	870	845	820

Table 2-2 Distance within which 80% of the eddy flux comes from for the SSA OBS calculated using equation 2-6. The results are for a range of sensible heat flux, H (W m^{-2}), and windspeed, u (m s^{-1}), values and z =26 m, d = 4.5 and z_0=1.03.

2.3 Site description

The site was chosen by BOREAS staff as representative of predominantly black spruce (*Picea mariana* (Mill.) BSP) stands of the southern boreal forest: with the proviso, that it was flat and with homogenous vegetation and so suitable for surface flux measurements by eddy covariance. A large proportion of the boreal forest is made up of black spruce making this an important vegetation type to investigate as part of a study of the forest – atmosphere exchanges of the boreal region.

The tower from which eddy covariance measurements were made was located at 53.99 ° N, 105.31 ° W at an altitude of 590 m resulting in a height corrected standard pressure of 94.0 kPa. The zero plane displacement, *d*, and roughness length, z_0, were found to be 4.5 m and 1.03 m respectively (Hale, 1996) and around the tower fetch

was at least 1.2 km, except to the north-east, where caterpillar tractors had been used to lay the power cable. To the north and east a road ran along the side of a low ridge, 1.2 km away, whilst ridges to the south and west were more than 2 km from the tower. The surface strata were peat overlying alluvial drift with the water table close to the surface all year (Jarvis *et al.*, 1997).

The tree cover was predominantly black spruce (*Picea mariana* (Mill.) BSP) with about 10% tamarack (*Larix laricina* (Du Roi) K. Koch) and scattered Jack pine (*Pinus banksiana* Lamb.) and some balsam poplar (*Populus balsamifera* Lamb.). The black spruce were close to an even age of 115 years, probably becoming established after a fire. The black spruce were up to 11 m tall and tamarack up to 16 m. The stem diameters (DBH) were 3 to 20 cm and with a basal area of 30 m^2 ha^{-1} (Halliwell and Apps, 1997). The crowns were very narrow with a median diameter of 1.6 m with a live crown length of up to 6 m. Projected leaf area index (LAI) was variable over the site and though narrow, the crowns were very dense, and mean LAI was 4.5 (Chen *et al*, 1997, Gower *et al*, 1997). Tree density was 5900 trees ha^{-1} but, again because the narrowness of the crowns, there was only 55 % canopy closure (Sellers *et al.*, 1994).

The understorey was patchy and generally under 50 cm though reaching a maximum of about 1.5 m. The understorey consisted of low shrubs (e.g. *Ledum groenlandicum, Vaccinium uliginosum, Potentilla fructicosa, Rubus idaeus, Rosa acicularis, Lonicera dioica, Betula glandulosa, B. glandulifera, Salix spp.*), herbs (e.g. *Mertensia paniculata, Geum aleppicum, Solidago canadensis, S. spathulata, Aster puniceus, Petasites palmatus, P. sagittatus, Potentilla palustris, Gallium boreale, Lillium philadelphicum, Platanthera hyperborea, Spiranthes romanzoffiana, Equisetum sylvaticum*), and dwarf shrubs (e.g. *Vaccinium vitis-idaea, Andromeda polifolia, Kalmia polifolia, Cornus canadensis*).

Over the wetter areas there was a sphagnum and feather moss (e.g. *Hylocomium splendens, Pleurozium schreberi*) hummock/hollow system whereas over the drier slightly elevated areas there were lichens (*Cladina* sp).

A hut with mains power and heating was provided as was a 24 m scaffold tower by BOREAS. Power sockets were provided on the tower.

2.4 Field measurements

The measurements were made in two campaigns: the first being in 1994 from May 23 (day 143) to September 21 (day 264) and the second in 1996 from March 25 (day 85) to November 28 (day 333). Soil temperature measurements, however, were made throughout the winter from 15 November 1995 until the end of the main measurements ending on 28 November 1996. The times shown are in GMT, which is the standard for BOREAS. The site is in Saskatchewan, in the North American Central Standard Time (CST) zone and does not any use daylight saving adjustment. However, as the site was at longitude 105.31 ° W and so solar noon is at approximately 19:00 GMT or 13:00 CST.

2.4.1 Eddy covariance system

The closed path EC (Eddy Covariance) sensors were placed on an upright pole at the south-west corner of the top of the tower. The south-west corner of the tower was used as one end of a tramway system was at the northern end of the tower and the main fetch at the site was from the west. The main canopy height, h, of black spruce was less than 11 m and so the EC sensors were above $2h$ which Cellier and Brunet (1992) suggest $2h$ as the lowest level for flux measurements.

The anemometer used in the eddy covariance measurements was a Solent A1012R2, (Gill Instruments, Lymington, UK) 3D research ultra sonic anemometer. The Solent outputs three orthogonal wind velocity components and the speed of sound from which air temperature may be derived at 20.8 Hz. To measure CO_2 and water vapour concentrations a LI-COR LI-6262 (LI-COR Inc., Lincoln, Nebraska) closed path infrared gas analyser (IRGA) was used. The inlet tube was placed 5 cm below the centre of the sonic anemometer's path and air was ducted down a 32 m heated tube (Dekabon 13, Samual Moore, OH, USA) (aluminium tube with PVC coating and polyethylene lining) of 6 mm internal diameter.

The airflow down the tube was controlled by a mass flow controller (TYLAN FC2900B, TYLAN General, Swindon, UK) at 6 dm^{-3} min^{-1} (calibrated at 0°C and 101.34 kPa) which resulted in pressure in the LI-6262's sample cell typically 7 kPa

less than atmospheric. The analogue to digital (A/D) converter in the sonic anemometer was used to sample the analogue output from the LI-6262 at 11 Hz. The linear outputs of the LI-6262 were used to take advantage of the LI-6262's processor to correct for sample cell pressure, CO_2 band broadening and dilution caused by water vapour. The fully processed CO_2 output of the LI-6262 is at 5 Hz and for H_2O at 3 Hz. The combined wind velocity and LI-6262 outputs were then transmitted from the Solent by RS-232 and received by a notebook PC where the fluxes were calculated by the EdiSol software which is described in Chapter 3. Computed fluxes, and from time to time primary data, were off-loaded onto removable hard disk cartridges (SyQuest, SyDos, Florida, USA).

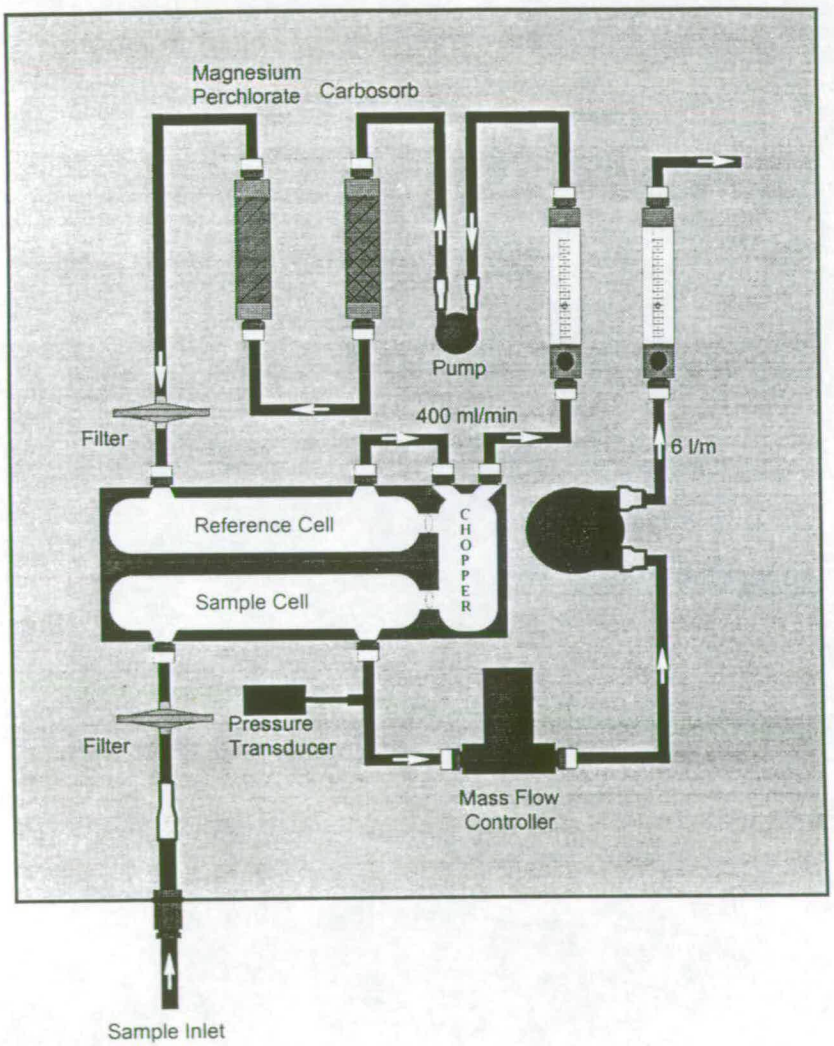

Figure 2-3 Sample and reference gas flow in the EC system.

The gas flow system was designed to have a low power requirement and battery back up which restricted the power available to the pump. This was advantageous despite having mains power at the site in that the mains supply was prone to overloading and outages at this remote location. The battery back up prevented many breaks in data collection that there would otherwise have been. Data capture was over 90%.

The gas analyser and gas flow system were housed in a box at the bottom of the tower. This position allowed easy access to the system to check its performance without disturbing other sensors on the tower (which we shared with many other BOREAS groups). Particularly, placing the box at the top of the tower may have interfered with the airflow over the anemometer. However, the sample tube used to duct the air from close to the anemometer path to the IRGA introduces an error to the measurement of fluctuations of the properties of the air as the air mixes in the tube. The primary factors influencing the attenuation of fluctuations down the tube is whether the air-flow is turbulent or laminar and the tube length (Lenschow and Raupach, 1991 and Massam, 1991). If the air-flow is laminar, the windspeed close to the tube wall is much slower than the air-flow at the centre of the tube mixing the air more than in turbulent flow where air that entered the tube at the same time tends to travel down the tube at the same speed. Air-flow is classed as turbulent if the Reynolds number, Re, > 2300 where:

$$Re = \frac{2rU_t}{\nu} \qquad (2\text{-}15)$$

r is the tube radius (m), ν is the kinematic viscosity of the sampled fluid and U_t is the windspeed down the tube (m s^{-1}). Hence, whether the air-flow is turbulent or laminar down a tube is determined by U_t and r (ν being out of experimental control in this situation). U_t is proportional to the flow rate the pump is capable of and inversely proportional to r, however, decreasing r increases friction (larger surface area to volume ratio) and the flow rate of which the pump is capable. In this low power system the pump was not capable of inducing turbulent flow.

Placing this box further up the tower would have enabled the use of a shorter sample tube and reduced the mixing of the air during transit to the IRGA. However, the next platform down was 6 m below the top platform requiring a sample tube length of about 9 m. Using the model of flux attenuation described in section 4.4 *Frequency Correction* [of fluxes] a typical flux attenuation using a 9 m tube was 15 % and that for a 32 m tube was 20 %. These attenuation coefficients are not the final errors in the flux estimates as the model is used to correct for the underestimation. The final error in the fluxes will depend on the error in the model and is unlikely to be significantly higher for the 32 m tube than a 9 m tube. Because of the benefits of frequent system checks and non-interference with other sensors the IRGA and box were placed at the bottom of the tower.

2.4.2 CO_2 and water vapour concentrations profile system

CO_2 and water vapour concentrations profiles were measured to enable the changes in storage (storage flux) of these gas species which is part of the mass balance equation (equation 2-3). In 1994 only CO_2 concentrations were monitored and at only four heights whereas in 1996 the profile system was extended to include water vapour concentrations and to include 8 heights. There were other changes too to the 1996 system and so the two systems are described separately below.

2.4.3 1994 CO2 concentration profile system

CO_2 concentrations were continuously monitored at five heights through the canopy, by a sampling line and an IRGA (LI-6252, LI-COR Inc., Lincoln, Nebraska) fitted with time switched solenoid valves. Air was drawn continuously through the sample pipes at each of the five heights 1.5, 3, 6, 12 and 26 m and each line was sampled for three minutes every fifteen minutes. Data from the first minute of every three minute period were discarded since this corresponded to the time taken to flush the IRGA sample lines clear of air from the previous sample line. In addition, air was drawn through a column containing Carbosorb one cycle every fifteen minutes in order to provide a constant check of the IRGA's zero.

All CO_2 concentration data were logged using a data logger (CR10, Campbell Scientific (UK) Ltd., Loughborough, UK), which also controlled the sample line switching three way solenoid valves through a purpose-built control circuit. Sample lines were of 5 mm i.d. nylon tubing, CO_2 adsorption/desorption was not considered a problem since all pipes were continuously purged whilst not being sampled by the IRGA. Sample inlets consisted of a gauze mosquito cover, an inverted funnel water trap and a fine particulate filter. Sampling to the IRGA was carried out via a pump downstream of which was a needle valve and flow meter, restricting flow to 0.5 dm^3 min^{-1}. The downstream end of the IRGA was left open to the atmosphere, ensuring operation at atmospheric pressure. The IRGA and valves were enclosed in a ventilated metal box, placed on wooden slats off the ground.

2.4.4 1996 CO2 and water vapour concentrations profile system

The number of heights in the profile was increased to eight with the extra sample heights close to the ground to improve the sampling of the logarithmic concentration profiles. The H_2O concentration profile was measured for comparison with the CO_2 profile. CO_2 and H_2O concentrations were continuously monitored at five heights through the canopy, by a sampling line and an IRGA (LI-6252, LI-COR Inc., Lincoln, Nebraska) fitted with time switched solenoid valves. Air was drawn continuously through the sample lines at each of the eight heights approx. 0.5, 1.5, 3.5, 6.5, 9.5, 12.5 18 and 26 metres and each line was sampled for one minute every ten minutes. Data from the first twenty seconds of each period was discarded to allow for flushing of the short tube between the solenoids and the analyser. The rest of the system was as for 1994.

2.4.5 Weather station analysis

The weather station was set up on the eastern side of the top platform of the tower at 24 m and was about 2.6 m horizontally from the EC system. The measurements detailed below were required at all BOREAS tower flux sites and are used in later chapters in the analysis of the surface fluxes.

2.4.6 Weather station 1994

At the top of the tower (24 m) a simple weather station was set up to measure the following environmental variables: net radiation, photosynthetic photon flux density (Q), short-wave solar radiation, air temperature, relative humidity, vapour pressure, wind speed and direction, and rainfall. Soil temperatures at 0.025, 0.05, 0.1, 0.2, 0.5 and 1 m were measured using a reference thermistor at 1 m and differential thermocouples at the shallower depths. Soil heat flux was measured using seven soil heat flux plates, buried about 7 cm below the surface of the moss just into the peat layer. Details of these sensors are shown in Table 2.3.

The rain gauge was located on top of the tower. Two net radiometers were mounted on the south side of the tower at a height of 16 m extending 3 m from the tower; one facing up and one facing down. A downward facing Q sensor was also placed at this location. This position offered some symmetry of tower influence on upward and downward fluxes whereas if the radiometers had been placed at the top of the tower only the upward fluxes would have been influenced. The soil temperature probe was located about 10 m from the SW corner of the tower and the soil heat flux plates were placed within 5 m of the probe.

Data loggers (21X, Campbell Scientific (UK) Ltd., Loughborough, UK) with multiplexers (AM416, Campbell Scientific (UK) Ltd.) were used to log output from the sensors listed in Table 2.1. Half-hourly summary statistics were calculated by the datalogger.

Variable	Sensor	Model and Manufacturer
Net radiation	2 x net radiometers	Q6, REBS, Seattle, Washington, USA
Solar radiation, incoming and reflected	Solarimeter	CM3, Kipp & Zonen, Delft, Netherlands
Solar radiation	Pyranometer	LI-200SZ, LI-COR Inc, Lincoln, Nebraska, USA
Photosynthetic Photon Flux Density (Q)	Quantum sensor	LI-190SZ , LI-COR
Relative Humidity	Humidity probe	SKH1031, Skye Instruments Ltd, Powys, UK
Wind direction	Wind vane	W200P, Vector Instruments, Rhyl, UK
Windspeed	Cup anemometer	A100R, Vector Instruments
Air temperature	Psychrometer developed at Edinburgh University	University of Edinburgh
Wet bulb temperature	Psychrometer developed at Edinburgh University	University of Edinburgh
Soil temperatures	Probe, differential thermocouples, copper-constantan and thermistor	University of Edinburgh
Soil heat flux	Heat flux plates	HFT3, REBS
Precipitation	Tipping bucket rain gauge, resolution 0.2 mm	Tipping bucket rain gauge,Cassella, London,UK

Table 2-3 List of the variables measured by the weather station in 1994 with the sensors used to measure them.

2.4.7 Weather station 1996

The weather station in 1996 was similar to that in 1994 but some sensors were changed and four soil temperature probes were used instead of one to improve sampling. The changes are detailed below in Table 2-4.

Variable	Sensor	Model and Manufacturer
Air temperature	Ventilated psychrometer	VP1, Delta-T Devices, Cambridge, UK
Wet bulb temperature	Ventilated psychrometer	VP1, Delta-T Devices
Soil temperatures	Four probes, differential thermocouples, copper-constantan and thermistor	University of Edinburgh
Precipitation	Tipping bucket rain gauge, resolution 0.2 mm	Tipping bucket rain gauge, Delta-T Devices

Table 2-4 Changes to sensors used in 1996. All other sensors and variables measured were as in 1994.

Soil temperatures were measured at four locations at 0.05, 0.1, 0.2, 0.5 and 1 m using differential thermocouples and reference thermistors at 1 m. Soil heat flux was measured using soil heat flux plates, buried about 7 cm below the surface just into the peat layer. The soil temperature probes were installed, two to the north east and two to the south east of the tower. Two soil heat flux plates were placed within 5 m of each probe.

2.4.8 Calibration

2.4.9 Gas analysers

The gas analysers used for the eddy covariance and concentration profile measurements were calibrated for water vapour using a dew point generator (LI-610, LI-COR, Nebraska, USA) and for CO_2 using cylinders of CO_2 in dry air cross-referenced to a BOREAS project standard which in turn was cross-referenced to global references. The analysers were calibrated every one to two weeks. Typical CO_2 and water vapour drift was 1 ppm drift in span and offset and 0.1 kPa. in span and offset, respectively, between calibrations.

2.4.10 Solent anemometers

These instruments have stable calibrations and factory values are used. The calibrations have been tested in Edinburgh University's wind tunnel and were found satisfactory.

2.4.11 Weather station

One of the radiometers was purchased new from the manufacturers and the calibration coefficient supplied with it was assumed accurate. This new radiometer was used as a standard against which the second one was calibrated. The radiometers were calibrated in the field as part of a comparison of net radiometers used in BOREAS (Hodges and Smith, 1997). A quantum sensor (LI-190SZ , LI-COR) with factory calibration is kept as a standard at the IERM and the quantum sensor used for this study was calibrated against this. The cup anemometer was calibrated in the wind tunnel at the department. The Skye temperature and humidity probe was calibrated by enclosing it in flasks containing salt solutions of known equilibrium water vapour pressures as supplied by Campbell. Lastly, the psychrometer, wind vane and pyranometer were purchased new and the manufacture's calibration coefficients were assumed accurate.

Chapter 3 Design of EdiSol

3.1 Introduction

By 1991, when EdiSol was designed, eddy covariance had been used successfully for short-term measurements of CO_2 surface fluxes (Anderson *et al.*, 1984; Baldocchi *et al.*, 1986; Valentini *et al.* 1991). Most measurements were made with instruments of unstable calibration that required constant attention. This limited measurement duration to a few days and often to dry weather. As reliable and weatherproof sonic anemometers and gas analysers were becoming available, long term measurements were becoming possible and long term monitoring became a realisable goal. Indeed, this has since become reality (e.g. Wofsy *et al.*, 1993) culminating in surface flux measuring networks EUROFLUX and AmeriFlux. There have also been large scale studies such as HAPEX Sahel (Goutorbe *et al.*, 1997) and BOREAS (Sellers, 1995) which have all involved campaign-made measurements using eddy covariance. Long term monitoring is important to ensure data covers the environmental range required for physiological analyses, to quantify inter-annual variation and to ensure the possibility of making measurements under the same conditions to increase statistical accuracy and precision of data (replication). This move would increase the amount of data to be processed many-fold and to help handle this increase, software that calculated covariances during data acquisition was developed. Processing data as it is acquired is often referred to as "real-time" processing. A low-power eddy covariance system was also required for measuring fluxes at sites where no mains power was available. This chapter describes the design of such a system. EdiSol software was used at many sites in the Southern Supersite in HAPEX Sahel (Moncrieff *et al*,. 1997) and is currently in use in EUROFLUX and is by some groups participating in AmeriFlux and Mediflux. It was also used in the ABRACOS study (Grace *et al.*, 1995a,b).

An eddy covariance system comprises sensors, data acquisition hardware and software to control the acquisition system and implement algorithms to calculate the fluxes. The work described here is the design and implementation of the software

system. The hardware is described to justify its use and to explain where it influenced the design of the software.

3.2 Overall Specification

The requirement was for a low power system to measure CO_2, H_2O, sensible heat and latent heat fluxes that could be run without mains power if necessary and be left unattended for a few days at a time. An eddy covariance system to measure these fluxes must comprise of: an anemometer to measure vertical windspeed, a gas analyser to measure CO_2 and H_2O concentrations, a temperature sensor and a device to log data from the sensors and calculate fluxes.

A 3-axis sonic anemometer is the preferred type of anemometer, to allow co-ordinate rotation and have a fast response with no inertia effects. The temperature sensor must have a fast response and not be significantly sensitive to radiation and the gas analyser must have a stable calibration so that the system can go without calibration for days at a time. Fast response (up to about 10 Hz) is important to capture fluctuations of windspeed and scalars at these frequencies that are associated with turbulent flux. Slower response sensors can be used without underestimating flux by measuring further above the surface where higher frequency fluctuations contribute less to the flux (Kaimal *et al.*, 1972). Compromises may be made, however, and response time may be traded for stability in calibration particularly when air is sampled down a tube to a closed path gas analyser instead of using an open path gas analyser. Fluctuations are damped as they travel down a tube but stable, closed path gas analysers are commercially available, whereas fast response open path gas analysers, with stable calibrations are expensive and custom made.

Software is required for the logging device to read data from the sensors and to calculate fluxes and supporting statistics as the data is acquired. Software discussed further in section 3.4.

3.3 Hardware

3.3.1 Solent 1012R2 anemometer

The anemometer chosen was the Solent A1012R2, (Gill Instruments, Lymington, UK) 3D research ultra sonic anemometer (Solent R2). The Solent R2 will output the wind velocity as orthogonal components (one nominally vertical and two nominally horizontal and mutually perpendicular) at 20.8 Hz. The anemometer includes an 11 bit A/D converter with up to five inputs for analogue voltages and a sample rate of 10.4 Hz. The three wind velocity components, the speed of sound and voltage readings of the analogue inputs are output by RS232 and can be read by a computer. The power consumption is 700 mW and the instrument is waterproof.

The windspeed and speed of sound are calculated from the transit times of sound pulses between two transducers. Two pulses of ultrasound travel in opposite directions between transducers a distance, l, apart. The transit times t_1 and t_2, are recorded. This allows the construction of two equations in which there are two unknowns, i.e. windspeed in the direction of the axis of the two transducers, u_t, and speed of sound estimated by the Solent R2, C_{Solent} (Shotanus *et al.*,1983).

$$u_t = \frac{l}{2}\left(\frac{1}{t_1} - \frac{1}{t_2}\right) \qquad (3\text{-}1)$$

$$c_{\text{Solent}} = \frac{l}{2}\left(\frac{1}{t_1} + \frac{1}{t_2}\right) \qquad (3\text{-}2)$$

The Solent R2 has three pairs of sensors arranged 120^0 apart horizontally and at 45^0 to the vertical. This arrangement minimises airflow disturbance and removes the effect of the lengthening of sonic path by wind velocity normal to the line between transducers (Gill Instruments, 1997). There are two forms of error caused by flow distortion: "cross talk" and wind blockage (Wyngaard, 1988). "Cross talk" errors are caused where windspeeds in a given direction are contaminated with windspeed fluctuations normal to that direction. Flow blockage results in increased or decreased windspeed fluctuations in a given direction. These errors are minimised for "cross-

talk" by using a symmetrical sensor geometry and for flow blockage by minimising flow obstruction (Wyngaard, 1986). The windspeed is measured between each transducer pair 56 times each second and internal software transforms the measured wind velocities to the above mentioned orthogonal velocities. The speed of sound is measured on only one transducer pair and the lengthening of sonic path by wind velocity normal to the line between transducers is significant in some cases (Schotanus *et al.*, 1983; Kaimal and Gaynor, 1991). This can be corrected for as shown in section 3.4.2.4.

The anemometer provides the temperature signal by approximating virtual temperature from the speed of sound. Sonic temperature, T_s, is given by:

$$T_s = \frac{c_s^2}{403} = T\left(1 + 0.32\frac{e}{P}\right) \qquad (3\text{-}3)$$

where T is absolute air temperature, e is vapour pressure, c_s is the speed of sound and P is atmospheric pressure. Sonic temperature very closely approximates virtual temperature (Kaimal and Gaynor, 1991).

3.3.2 LI-COR LI-6262 infra-red gas analyser

Open path infra-red gas analysers measure the partial densities of gas molecules at ambient pressure and temperature. Eddy covariance flux estimates with these analysers require large WPL corrections. The correction may be made by estimating the mean vertical windspeed from the sensible heat flux and evaporation or by removing the balancing density fluctuations (WPL corrections) (Webb *et al.*, 1980). Sensible heat flux can cause up to a 50% error and evaporation a 10% error in flux estimations. With closed-path infra-red gas analysers the air to be sampled is drawn down a tube and fluctuations of temperature and other scalars are damped (Philip, 1963; Lenshow and Raupach, 1991). Temperature fluctuations are damped most and as little as 2 m of copper tubing can reduce these to negligible levels (Leuning and Moncrieff, 1990) removing the need for WPL corrections for temperature fluctuations. The removal of temperature fluctuations is therefore an advantage when using closed path analysers. However, the damping of gas concentration fluctuations

results in an underestimation of the flux and the underestimation must be verified as negligible or corrected for (Leuning and Moncrieff, 1990). Current open path gas analysers are bulky and cause airflow distortion when upwind of the anemometer. For short-term work, open path analysers can easily be positioned so as not to distort airflow over the anemometer, however, for long term monitoring frequent repositioning is necessary as wind direction changes. The much smaller sample tube of a closed path analyser, in contrast, produces a minimum of distortion and so is preferable for long-term monitoring.

Given that there were no suitable open path gas analysers available commercially and that the LI-COR LI-62XX (LI-COR, Lincoln, NE, USA) family of closed path gas analysers were available, the LI-6262 was chosen. The LI-62XX has been adapted by widening the ports to the sample tube for relatively fast response and have stable calibrations. The LI-6262 measures both CO_2 and water vapour concentration. The fast response options of the LI-62XX respond to 95 % of a step change in 0.1 s or have a cut-off frequency of 5 Hz. (The cut-off frequency defined here is the frequency at which the measured amplitude is 0.707 of the amplitude of a sinusoidal oscillation of gas concentration.)

The calibration of the LI-6262 is sensitive to temperature and pressure. Whereas the optic bench temperature is measured, a constant is assumed for the pressure in the standard calibration calculations. A pressure sensor measuring the air pressure close to the sample cell is optional to allow the measured pressure to be used in the calculations instead of the assumed constant. In the field calibration checks are required only every week or fortnight if a pressure transducer is used to make pressure corrections. The changes in span and drift typically being less than 0.5 % of ambient values over one or perhaps two weeks.

The LI-6262 contains software to apply the calibration for CO_2 and water vapour concentration and water vapour measurements can be used to correct for cross sensitivity to water vapour when measuring CO_2. Cross sensitivity is caused by infra-red absorption band broadening alone because the overlap of the absorption bands used is negligible (LI-COR, 1991). The internal software will also calculate CO_2 concentration as if in dry air so taking care of the water vapour dependent WPL

corrections. The temperature dependent WPL corrections are eliminated by sampling the air down a tube as the temperature fluctuations are damped out. Calibrated CO_2 output frequency is 5 Hz and that of H_2O is 3 Hz. Output is by 12 bit digital to analogue voltage conversion or digitally using the RS-232 standard.

3.3.3 Data acquisition

Calibrated analogue output from the LI-6262 corresponding to a CO_2 or H_2O sample concentration is input to the Solent analogue to digital (A/D) converter where it is combined with the wind velocity and speed of sound data. The combined data is transmitted to the computer by RS232 approximately every second. No low pass filtering of the LI-6262's analogue output is required to prevent aliasing as the A/D sampling rate of the Solent is 10.8 Hz giving a Nyquist frequency of 5.4 Hz. The output frequency of the LI-6262 calibrated signals is less than this. Calibrated analogue output from the LI-6262 is used because the A/D resolution of the Solent R2 of 11 bits is inadequate when used with the unprocessed analogue output and then calibrated digital (RS232) output would be difficult to synchronise with the wind velocity data.

The A/D converter input range of the sonic anemometer is 0 to 5000 mV with a resolution of 11 bits and the output range of the LI-6262 is 0 to 5000 mV corresponding to a CO_2 concentration range of 0 to 3000 μmol mol^{-1}. Therefore, the CO_2 concentration resolution is $3000 / 2^{11} = 3000 / 2048 = 1.46$ μmol mol^{-1}. Using the calibrated analogue output allows the 0 to 5000 mV range to correspond to say, 300 to 400 μmol mol^{-1} giving a resolution of $100 / 2048 = 0.05$ μmol mol^{-1}. In this case, the A/D conversion is no longer limiting and the total system resolution depends upon the resolution of the LI6262. Table 3-1 shows the percentiles for half hourly standard deviation of CO_2 concentration measured at BOREAS SSA OBS. Using the A/D converter of the Solent R2 simplifies synchronising sampling of wind vectors and scalars and reduces costs.

Percentile	Standard deviation (μmol mol^{-1})
99.0	2.84
97.5	2.10
95.0	1.57
90.0	1.05
75.0	0.60
50.0	0.35
25.0	0.20
10.0	1.40
5.0	0.12
2.5	0.12
1.0	0.11

Table 3-1 Percentiles for half-hourly standard deviation of CO_2 concentration measured at BOREAS SSA OBS.

3.4 Software

3.4.1 Specification

3.4.1.1 General specifications

The software must acquire the wind velocity and scalar data from the Solent R2 and calculate CO_2, water vapour, sensible heat and latent heat fluxes. Also required are friction velocity and means and variances of input variables (orthogonal wind velocities, temperature, CO_2 concentration and water vapour concentration). The design is object-orientated and an object-orientated language (Borland Pascal 7) was used for the implementation to allow for changes in hardware and in software development tools.

The major tasks for the software are:

- Accept data from the Solent by RS232.
- Save raw data from the Solent to disk if required.
- Convert the Solent output to useful units (calibration).
- Rotate the wind velocity components.
- Compensate for the time taken for the air to travel down the tube if a closed path gas analyser is used.
- Calculate covariances and other statistics.
- Convert the covariances to flux units.

3.4.1.2 Rotation of the wind velocity components

Stream lines are not usually horizontal and so fluxes between the surface and the atmosphere are not usually vertical. Knowing the wind components as output by the Solent R2, it is possible to calculate the stream flow orientation with respect to the Solent R2 geometry and thence transform the vector covariances and variances to the stream line orientation.

Following McMillen (1988) the rotation angles are calculated from the means of the nominal wind components. The first rotation of angle ε around the vertical, z, axis aligns the x axis with the mean horizontal wind direction making $v = 0$. The second rotation is around the lateral, y, axis of angle θ and aligns the x axis with the mean wind vector forcing w to zero. Finally, the third rotation of angle β is around the x axis and minimises the absolute covariance of v with w.

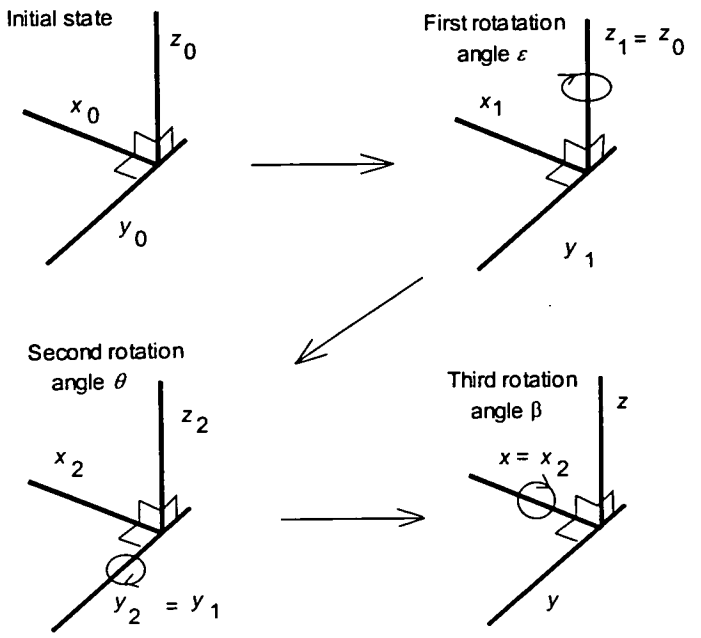

Figure 3-1 Diagram showing the three co-ordinate rotations used to align the wind components with the stream lines.

The co-ordinate rotation routines used in EdiSol were first described in a report by McMillen (1986) and were implemented by McCracken (1993) after correcting a number of typographic errors in that report. The rotations align the co-ordinate references with the local streamlines so that w is perpendicular to the streamlines and has no component in the direction of the mean flow. This is important when, as in most cases, that it is the flux between the surface and the atmosphere. McMillen (1986) showed that co-ordinate rotation improved momentum flux, τ, measurements on an airfield (assuming that τ should always be negative at the surface, i.e. momentum is absorbed not created at the surface). The averaging period used to calculate the rotation angles is important. If too short a period is used x and y alignment will be heavily influenced by gusts and the flux will be underestimated. The same problem is exacerbated inside a canopy or at night when most of the flux is carried by low frequency eddies the xy plane will be aligned with the gust and the flux will be underestimated. However, if the averaging period is too long, the xy plane will not be aligned with the local streamlines and flux measured will be contaminated with a component of the flux along the surface.

3.4.1.3 Compensation for the delay in air sampling

A consequence of the use of a closed path gas analyser is that air must be ducted from close to the anemometer to the gas analyser down a tube with the flow driven by a pump. This introduces a delay between the wind velocity and temperature measurements and the measurements of gas concentrations. To compensate for this the software must store the undelayed measurements until the delayed gas concentration measurements are received by the computer. Both sets of measurements must then be combined in the same record representing concurrent observations of the measured variables. This record can then be used to calculate fluxes and other statistics.

The values of the undelayed measurements are easily stored in a circular buffer. A circular buffer is an array in which new data is stored over-writing the oldest data. Pointers are maintained allowing the retrieval of observations stored at a given time up to a maximum delay determined by the buffer size. Because old data is over written, the array must, at least, be large enough to store the number of samples given by the maximum delay required and the sample period.

To retrieve the wind velocity and temperature data, concurrent with the gas concentration measurements, the delay between the two sets of data must be known. The delay in this and all systems sampling air through a tube is the time taken for the air to travel down the tube. Three methods available to estimate this time are: 1) calculate time given the tube dimensions and flow rate, 2) measure the time for a step change in concentration caused at the sample end of the tube to be registered by the gas analyser, and assume this time remains constant between measurements and 3) estimate the delay using lagged cross-correlation between the wind data and the gas concentration data.

Calculation of the delay given the flow rate and tube dimensions is easy to do but the accuracy of the result depends on the accuracy of the given parameters. The lag time is given by:

$$t_t = \frac{l_t \pi r^2}{R_v} \qquad (3\text{-}4)$$

where l_t is the tube length, r is the internal radius of the tube and R_v is the volume flow rate.

Changes in air pressure, voltage and temperature effect pump efficiency and will cause changes in flow rate where the pump is the sole controller of the flow. Filters must be used at the sample end of a tube to prevent particle deposition on the tube wall where they may change the adsorption properties of the tube for the gas constituents being measured. Particles must also be prevented from entering the gas analyser and changing its calibration. Changes in flow rate may be caused by the clogging of filters altering the resistance to airflow and hence air pressure in the tube causing a change in flow rate. To allow the flow rate to be known accurately a mass flow controller (MFC) may be used. However, even when the mass flow is kept constant the volume flow will change with temperature and pressure and these changes will be proportional to the length of the tube (see below). Another source of inaccuracy in calculating the transit time down the tube is the accuracy of the tube dimensions used. Tubes generally available are not made to precise dimensions and precise measurements of the dimensions are not possible. In addition, gas constituents may travel more slowly than the general airflow if there is adsorption/desorption on the tube wall. Electrically polarised molecules such as water vapour interact with the tube wall (Moncrieff *et al.*, 1997) as do reactive molecules, e.g. ozone (Massam, 1991).

The transit time down a tube for a given gas species may be determined accurately by causing a step change in concentration at the mouth of the tube, usually by solenoid valve, and measuring the time elapsed before the gas analyser registers the step change. This gives an accurate measurement for one set of conditions but air resistance by filters, atmospheric pressure and temperature will vary over time causing the transit times to vary. This measurement may be made periodically to reduce the error caused by variation (e.g. Goulden *et al.*, 1996).

Lastly, transit time down a tube for a gas species may be estimated using lagged cross-correlation between the wind velocity time series and the gas concentration time series (McMillen, 1988; Grelle and Lindroth, 1996). This has the advantage that it can be calculated as data is collected (in real time) and changing lag times caused

by clogging filters, and changing atmospheric pressure and temperature can be compensated for. This technique is used in EdiSol and the lags are calculated in real time. Even when using a mass flow controller, calculation of lags in real time is useful because the fixed mass flow results in a change in volume flow when temperature and pressure changes. Typical results of the lagged cross-correlation of CO_2 concentration with vertical wind velocity are shown in Figure 3-2.

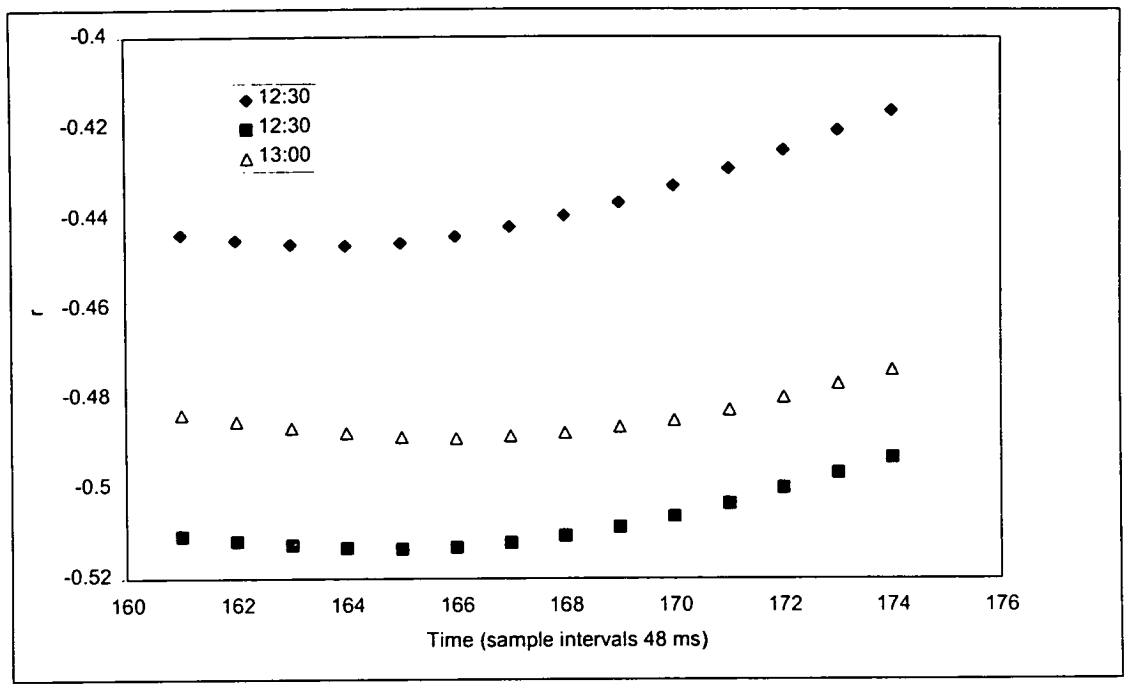

Figure 3-2 Correlation coefficients of CO_2 concentration with vertical wind velocity with different lag times between the variables for three half-hour periods on 1 September 1996 at SSA OBS.

3.4.1.4 Change in volume flow with temperature and pressure when using a MFC

The MFC controls the mass flow of a given mixture of gases determined by the specific heat capacity of the mixture and temperature changes induced by heating (Tylan General Corp., 1992). For air (a mixture of gases) the specific heat capacity does not change significantly in the meteorological range and changes in the proportion of gases including water vapour may be ignored (Tylan General Corp., 1992). However, the volume of a mass of gas varies with temperature and pressure (ideal gas law). Even with a fixed mass flow of air, the transit time down the tube,

which depends on the volume flow, will be directly proportional with absolute temperature and pressure. Then relationship between volume flow rate and mass flow rate is given by:

$$R_v = \frac{R_m \Re T_t}{M_a P_t} \qquad (3\text{-}5)$$

where R_m is the mass flow rate, T_t is the air temperature in the tube, M_a is the molecular mass of moist air and P_t is the air pressure in the tube.

Combining equations 3-4 and 3-5 gives the lag time as a function of mass flow rate:

$$t_t = \frac{l_t \pi r^2 M_a P_t}{R_m \Re T_t} \qquad (3\text{-}6)$$

where R_m is the mass flow rate, T_t is the air temperature in the tube, M_a is the molecular mass of moist air and P_t is the air pressure in the tube.

Large meteorological changes in absolute temperature and pressure may be in the range of only, say, 3 %. However, the transit time down the tube depends on the volume of the tube and is directly proportional to its length (given a constant cross section) and thus variation in transit time caused by absolute temperature and pressure changes will vary proportionally with length of the tube.

3.4.2 Calculations and procedures

Figure 3-3 shows the data and control flow of the software and is followed by paragraphs describing the procedures or functions in detail.

3.4.2.1 Initialisation

The RS232 port to which the Solent R2 is connected to is configured before data logging starts. The Solent R2 is put in the "unprompted" mode in which it saves 20 records of data in an internal buffer and then transmits them to the computer in one

packet. (N.B. in the Solent R2 user manual, Gill Instruments use "record" and "packet" in non-standard ways. Here the author uses a more conventional meaning of "record" as the values of a given set of variables at one observation.) The user may choose whether the anemometer makes corrections for strut interference.

3.4.2.2 Check RS232 port for data

The procedure *Check RS232 port for data* reads data from the RS232 port, swaps the bytes which make up the integer values into the correct format for IBM PC compatibles and converts these into IEEE single precision floating point representations in an array for processing.

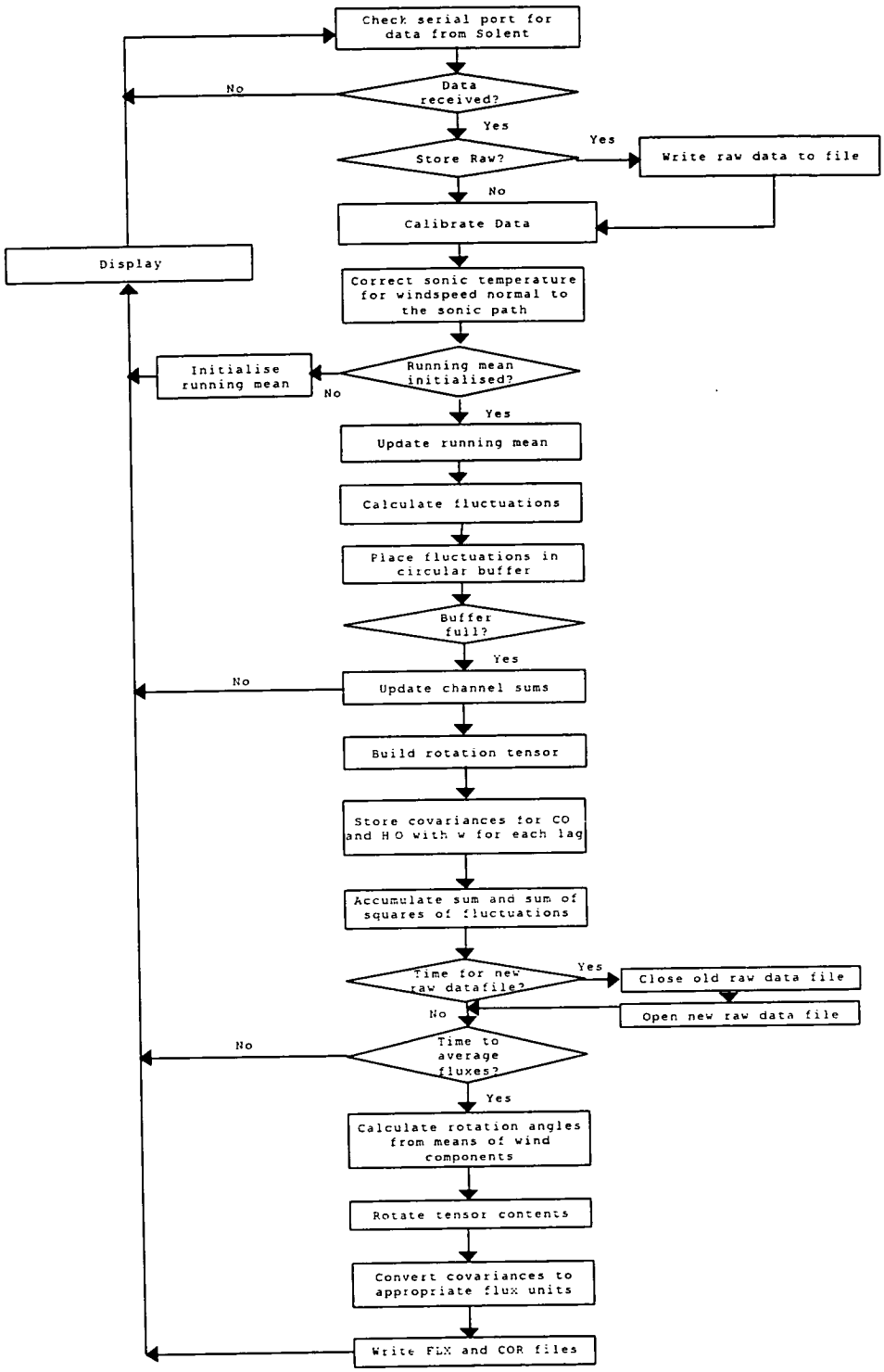

Figure 3-3 Flow diagram for EdiSol data logging and "real time" data processing. See text for details.

3.4.2.3 Calibrate data

The calibrations are implemented using a quadratic equation:

$$y = ax^2 + bx + c \qquad (3\text{-}7)$$

This allows linear calibrations to be implemented be making $a = 0$ and also for the derivation of sonic temperature from the speed of sound which requires a squared term (see below).

Table 3-2 shows the units for Solent R2 wind velocity and speed of sound as output by the Solent R2 (raw units). The values of the coefficients a, b, and c for each variable to convert them to calibrated units are also shown.

Variable	Raw Unit	a	b	c	Calibrated Unit
u	cm s^{-1}	0.0	0.01	0.0	m s^{-1}
v	cm s^{-1}	0.0	0.01	0.0	m s^{-1}
w	cm s^{-1}	0.0	0.01	0.0	m s^{-1}
Speed of sound	1/50 m s^{-1}	9.9256×10^7	0.0	273.15	Sonic temperature °C

Table 3-2 Calibration of Solent R2 wind velocity and speed of sound conversion to sonic temperature

The calibration for the wind speed component of the sonic anemometer is simply a conversion from cm s^{-1} to m s^{-1}. For sonic temperature, the calibration incorporates the calculation of T_s from C_s. The sonic anemometer output the speed of sound from the serial port in m s^{-1} 50^{-1} ($C_{s,serial}$) so:

$$C_s = C_{s,serial}/50 \qquad (3\text{-}8)$$

substituting into equation 3-3 (the two left hand terms)

$$T_s = C_{s,serial}^2/403 \,.\, 50^2 \text{ (Kelvin)} \qquad (3\text{-}9)$$

Convert to °C

$$T_s = 1/1007500\, C_{s,serial}^2 - 273.15 \qquad (3\text{-}10)$$

Compare 3-10 with 3-7 and equate coefficients and

a = 1/1007500 = 9.9255583, b = 0 and c = -273.15

Values of analogue voltage inputs to the Solent R2 are output from serial port encoded as mV. The calibration coefficients then depend upon the calibration of the sensor connected to the Solent R2 analogue input. For connections to the LI-6262 CO_2 and H_2O computed outputs, *a* should be set to zero, *b* to the gain set for the DAC (Digital to Analogue Convertor) on the LI-6262 and *c* to the offset set for the DAC. (The LI-6262 CO_2 and H_2O computed outputs are linear.)

3.4.2.4 Correct sonic temperature for windspeed normal to the sonic path

The true path of sonic pulses between transducer pairs is longer than the distance between them as the pulse moves through a travelling medium, the air. Any wind velocity component normal to the straight line between the transducers will lengthen the path travelled by the pulse. The true sonic temperature is given by Kaimal and Gaynor (1991) as:

$$T_{Solent} = T_s - {}^{V_n^2}\!/_{403} \qquad (3\text{-}11)$$

where T_{Solent} is sonic temperature estimated by assuming the sonic path length is the distance between the transducers and V_n^2 is the wind speed normal to the straight line path between the transducer.

If the speed of sound is derived from transducers arranged vertically, the wind velocity component normal to the measurement axis is the resultant of the *u* and *v* components. However, the Solent anemometer transducers are arranged non-orthogonally so the speed of sound cannot be measured on a vertical axis. The speed of sound is measured using transducer pair 1 and the speed of sound is given by:

$$T_s = T_{Solent} + \sqrt{v_0^2 + 0.5|u_0 - w_0|^2} \qquad (3\text{-}12)$$

3.4.2.5 Update moving average

The ARMA is used to estimate fluctuations for the calculation of variances and covariances but can be used to remove trends caused by sensor drift. The ARMA used can be used in "real time" and is:

$$\bar{a}_t = \eta \bar{a}_{t-1} + (1-\eta) a_t \qquad (3\text{-}13)$$

where $\bar{a}_t$ and $\bar{a}_{t-1}$ are the values of the ARMA at time t, and t-1 respectively; a_t is the instantaneous value at time t, and η is a weighting coefficient, given by $\eta = e^{-\Delta t/\Gamma}$, where Γ is the time constant of the ARMA (Lloyd *et al.*, 1984; McMillen, 1988).

3.4.2.6 Calculate fluctuations

The fluctuations are required for the calculation of covariances and variances. True fluctuations are estimated by subtracting the moving average as calculated in section 3.4.2.5 from the instantaneous value.

$$a'_t = a_t - \bar{a}_t \qquad (3\text{-}14)$$

3.4.2.7 Place fluctuations in a circular buffer

When the sampling of some variables is delayed, the values of the undelayed samples must be stored if contemporary values are needed with the delayed samples. The most common cause of a delay in sampling is the use of closed path gas analysers where the air must travel down a tube before being analysed. In EdiSol each record of data from the collector is stored in a buffer which can contain a given number of records. When the buffer is full, the earliest record is over written with the newest. Access procedures to the data in the buffer allow retrieval of the values of a given record placed in the buffer a given number of sample intervals ago.

3.4.2.8 Update channel sums

The sums of the sampled variables over the given averaging period are required for calculation of the means. Therefore, at each observation interval the cumulative sum is computed.

3.4.2.9 Build rotation tensor

A tensor, M_0, of cumulative sums of products of wind components and scalar fluctuations is updated with each record received assuming no lag between samples.

$$M_0 = \begin{pmatrix} \sum u'u' & \sum u'v' & \sum u'w' & \sum u'T'_s & \sum u'c' & \sum u'q' \\ \sum v'u' & \sum v'v' & \sum v'w' & \sum v'T'_s & \sum v'c' & \sum v'q' \\ \sum w'u' & \sum w'v' & \sum w'w' & \sum w'T'_s & \sum w'c' & \sum w'q' \end{pmatrix} \quad (3\text{-}15)$$

This tensor is divided through by the number of samples at the end of the averaging period to provide variances and covariances see section 3.4.2.14.

3.4.2.10 Store cumulative sums of products of fluctuations for each lag

The sums of products of fluctuations of delayed scalar values (CO_2 and H_2O concentrations) and vertical windspeed are stored in a buffer to enable the covariances to be calculated for a range of delay times. The correctly lagged covariances can then be copied into the rotation tensor when the lag times to use have been selected.

3.4.2.11 Accumulate sums and sums of squares of fluctuations

The sums and sums of squares of the fluctuations of CO_2 and H_2O concentrations are also stored in buffers to allow lagged cross-correlations to be calculated. These are used to determine the lag times. The lag time of the most extreme value is used as the lag time.

3.4.2.12 Calculate channel means

Means are required for final output and the mean nominal wind components are needed to calculate the angles for co-ordinate rotation. These are calculated from the cumulative sums.

3.4.2.13 Calculate rotation angles from means of wind components

The rotation angles are calculated from the means of the nominal wind components. The first rotation angle, ε, with cosine, $C\varepsilon$, and sine, $S\varepsilon$,

$$\varepsilon = \tan^{-1}\left(\frac{\overline{v}_o}{\overline{u}_o}\right), C\varepsilon = \frac{\overline{u}_o}{\sqrt{\overline{u}_o^2 + \overline{v}_o^2}}, S\varepsilon = \frac{\overline{v}_o}{\sqrt{\overline{u}_o^2 + \overline{v}_o^2}} \tag{3-16}$$

The second rotation angle, ϕ, with cosine, $C\phi$, and sine, $S\phi$,

$$\phi = \tan^{-1}\left(\frac{\overline{w}_o}{\sqrt{\overline{u}_o^2 + \overline{v}_o^2}}\right), C\phi = \frac{\sqrt{\overline{u}_o^2 + \overline{v}_o^2}}{\sqrt{\overline{u}_o^2 + \overline{v}_o^2 + \overline{w}_o^2}}, S\phi = \frac{\overline{w}_o}{\sqrt{\overline{u}_o^2 + \overline{v}_o^2 + \overline{w}_o^2}} \tag{3-17}$$

The third rotation angle, β, with cosine, $C\beta$, and sine, $S\beta$,

$$\beta = \frac{1}{2}\tan^{-1}(2Y) \text{with} : Y = \frac{\overline{v_2 w_2}}{\overline{v_2^2} - \overline{w_2^2}} \tag{3-18}$$

$$C\beta = \left(\frac{1 + \left(1/(1+4Y^2)\right)^{1/2}}{2}\right)^{1/2}, S\beta = \left(\frac{1 - \left(1/(1+4Y^2)\right)^{1/2}}{2}\right)^{1/2}$$

(Kaimal and Finnigan, 1994).

3.4.2.14 Rotate tensor contents

Using the calculated rotation angles, the rotation tensor may be transformed with the axes aligned with the stream lines. The transformations are equally valid for instantaneous and mean values of wind velocity components and covariances of a wind velocity component and scalar. In the equations below only the rotation of wind

velocity components are shown but these may be substituted for by a covariances of a wind velocity component and scalar.

First rotation:

$$u_{1,i} = \sum_j A_{01,i,j} \cdot u_{0,j} \qquad (3\text{-}19)$$

with :

$$A_{01} = \begin{pmatrix} C\varepsilon & S\varepsilon & 0 \\ -S\varepsilon & C\varepsilon & 0 \\ 0 & 0 & 1 \end{pmatrix} \qquad (3\text{-}20)$$

Second rotation:

$$u_{2,i} = \sum_j A_{12,i,j} \cdot u_{1,j} \qquad (3\text{-}21)$$

with :

$$A_{12} = \begin{pmatrix} C\theta & 0 & S\theta \\ 0 & 1 & 0 \\ -S\theta & 0 & C\theta \end{pmatrix} \qquad (3\text{-}22)$$

Third rotation:

$$u_{3,i} = \sum_j A_{23,i,j} \cdot u_{2,j} \qquad (3\text{-}23)$$

where:

$$A_{23} = \begin{pmatrix} 1 & 0 & 0 \\ 0 & C\beta & S\beta \\ 0 & -S\beta & C\beta \end{pmatrix} \qquad (3\text{-}24)$$

3.4.2.15 Convert covariances to appropriate flux units

A flux is the transfer of a quantity per unit area per unit time (Stull, 1988). The covariances calculated so far are in kinematic flux form and require multiplying by air density to transform them to quantity units.

The covariances are converted to flux units by the following equations:

$$\text{CO}_2 \text{ flux}, F_c = \frac{P}{\Re T}\overline{w'c_c'} \quad (\mu\text{mol m}^{-2}\text{ s}^{-1}) \tag{3-25}$$

$$\text{Evaporation}, E = \frac{P}{\Re T}\overline{w'h_c'} \quad (\text{mmol m}^{-2}\text{ s}^{-1}) \tag{3-26}$$

$$\text{Momentum flux}, F_m = \frac{PM_a}{\Re T}\overline{u'w'} \quad ([\text{kg m s}^{-1}] / [\text{m}^2\text{ s}] = \text{N m}^{-2}) \tag{3-27}$$

$$\text{Friction velocity}, u_* = \sqrt{\overline{u'w'}} \quad (\text{m s}^{-1}) \tag{3-28}$$

Latent heat flux is given by, λE (J m^{-2} s^{-1} = W m^{-2}), (3-29)

where λ is the latent heat of vaporisation of water (J mmol^{-1}) = $M_w\lambda_{mass}/1000$

$\lambda_{mass} \approx 2501 - 2.37t$ (J g^{-1}) where t is air temperature (°C)

M_w is the molecular mass of water = 18 g mol^{-1}.

$$\text{Sonic sensible heat flux}, H_s = \frac{PM_a}{\Re T}C_P\overline{w'T_s'} \quad (\text{J m}^{-2}\text{ s}^{-1} = \text{W m}^{-2}) \tag{3-30}$$

where P is the atmospheric pressure (Pa),

$\Re$ is the gas constant (8.314 J K^{-1} mol^{-1}),

M_a are the molar mass of air (kg mol^{-1})

T is ambient absolute temperature (K)

T_s is sonic absolute temperature (K)

c_c is molar ratio of CO_2 in dry air at constant temperature (μmol mol^{-1})

h_c is molar ratio of water vapour in air at constant temperature (mmol mol^{-1})

and C_P is the specific heat capacity of air at constant pressure (J kg^{-1} K^{-1}).

Monin-Obukov length, L is also calculated, as given by Monteith and Unsworth (1990):

$$L = \frac{-\rho c_p T u_*^3}{kgH_s} \tag{3-31}$$

where:

g is the acceleration due to gravity (9.81 m s^{-2})

ρ is the density of air $\left(\frac{PM_a}{\Re T}\right)$(kg m^{-3})

and k is the von Karman constant (0.41)

3.4.2.16 Write the flux and lagged correlation files

Sonic sensible heat, latent heat, CO_2, evaporation and momentum fluxes, channel means and variances are written out to the flux output file see Table 3-4 for a list of the output variables and their units.

The lagged cross-correlations are written out to the lagged correlation file for later inspection and analysis of the algorithm used to estimate the lags (see Table 3-5 for the format of the table).

3.4.3 Processing of EdiSol output flux file

If the CO_2 concentration is measured using a closed path analyser with a suitable sampling tube no temperature WPL correction will have to be made to F_c. Likewise, if the water vapour concentrations fluctuations have been removed from the air of which the CO_2 content has been analysed or the CO_2 concentration has been calculated as if in dry air (LI-6262 option), then no water vapour WPL correction should be made to F_c. However, if an open path gas analyser were used to measure the CO_2 concentrations then WPL corrections for temperature and water vapour concentration should be made to F_c.

Column	Heading	Description	Units	Notes
1	Yr	1992 etc.		
2	Mon	1,2,,,12		
3	Day	1,2,,,28,[29,30,31] + day of week		
4	h	0,1,2,,,23		
5	m	0,1,2,,,59		
6	Sonic H	Sonic Sensible heat flux	W m^{-2}	
7	LE	Latent Heat	W m^{-2}	
8	E	Water vapour flux	mmol $m^{-2}s^{-1}$	
9	C	CO_2 flux	µmol $m^{-2}s^{-1}$	
10	MomtmFlux	Momentum flux	m^2 s^{-2}	
11	U*	Friction velocity	m s^{-1}	
12	M-O length	Monin - Obukov length	m	
13	var u	variance of u	m^2 s^{-2}	
14	var v	variance of v	m^2 s^{-2}	
15	var w	variance of w	m^2 s^{-2}	
16	var T_s	variance of sonic temperature	$°C^2$	
17	var c	variance of CO_2 concentration	$µmol^2$ mol^{-2}	
18	var h	variance of H_2O concentration	$mmol^2$ mol^{-2}	
19	av u	mean windspeed x_n component	m s^{-1}	x_n is aligned with 330 °
20	av v	mean windspeed v_n component	m s^{-1}	y_n is aligned with 240 °
21	av w	mean windspeed w_n component	m s^{-1}	z_n is aligned with the nominal vertical axis
22	av t	mean sonic temperature	°C	
23	av c	mean CO_2 concentration	µmol mol^{-1}	
24	av h	mean H_2O concentration	mmol mol^{-1}	
25	windspeed	mean windspeed	m s^{-1}	
26	wind dir	wind direction	degrees	
27	Eta	first rotation angle	degrees	
28	Theta	second rotation angle	degrees	
29	Beta	third rotation angle	degrees	
30	C lag	CO_2 time lag	sample periods	
31	H lag	H_2O time lag	sample periods	

Table 3-4 Column headings and units

	delay time in 1/20.8 ths of a second.	correlation coefficient.

Table 3-5 Lagged correlation file format.

If the water vapour concentration is measured using a closed path analyser with a suitable sampling tube no temperature WPL correction will have to be made to E. However, if an open path gas analyser were used to measure the water vapour concentrations then WPL corrections for temperature should be made to E.

True sensible heat can be calculated from H_s using:

$$H = H_s - \frac{P_a M_d}{\Re T} C_d \left(3.210^{-4} \overline{T}\,\overline{w'h'}\right) \text{ (W m}^{-2}\text{)} \qquad (3\text{-}32)$$

All the flux estimates and variances calculated by EdiSol must also be corrected for non-ideal frequency response of the sensors and measuring system (see Chapter 4).

3.4.4 Object Orientated Programming and Design

Object Orientated Programming (OOP) makes the design and implementation of modular software much easier than traditional procedural programming. OOP does not replace procedural programming completely because in most OOP languages the final algorithms for procedures and functions are coded procedurally. EdiSol is designed to be implemented in Borland Pascal with objects but could easily have been implemented in most other OOP languages.

There are three main concepts in OOP all of which Borland Pascal implement:

1. Encapsulation – The variables, procedures and functions required for a specific purpose, are bound together in an "object". The object is viewed as a black box, with internal details hidden away, unless the user specifically wants to look at the code. Classes of objects are defined which have the same variables, procedures and functions. Different objects of the same class may be instantiated and given different values for their variables to represent different cases.

2. Inheritance – a class of objects may be defined in terms of an existing class. The new class is a specialisation of the existing one. The variables and functions of the existing class are "inherited" and new ones may be added.

3. Polymorphism – inheritance as described above is very useful but is also possible to override inherited procedures and functions and replace them with corresponding sub-programs that have different results. Sub-classes (specialisations) are still members of the super-class and a routine that uses members of a class does not have to know which specialised class they belong to.

By designing abstract classes to define the basic functionality required, changes (e.g. in hardware) can be allowed for. Specialisations of these abstract classes are then defined to implement the hardware specific features but present a common interface via the general abstract class (e.g. all raw data files formats used by The University of Edinburgh, Institute of Ecology and Resource Management, micrometeorology section are all members of the class *EdiFile*. Class *EdiFile* defines an interface for reading from and writing data to any such raw data file. To access the data in any *EdiFile*, for processing, only this common interface need (or should) be used. Details for handling different raw file formats are hidden in specialised sub-classes and the same processing routine can be used with any *EdiFile*.

Changes in user interface were planned for by separating the data acquisition and processing code from user interface code and in general, by using the modularization inherent in OOP.

EdiSol is designed based on the following view (or model) of an eddy covariance measuring system. All sensors for the environmental variables pass data to a device that samples the variables, collects them together and passes them to the computer where the data may be saved to file. This is the *Collector* class in EdiSol. The data from the collector must be calibrated from whatever units they are collected in to physically meaningful units. This is done by an object of the *Calibrator* class. The variables are then in an appropriate form for use by the procedures that calculate the fluxes. These procedures are collected together into a *Flux Calculator* class which also co-ordinates other classes. Once the *Flux calculator* has calculated the fluxes, they are saved to a file. With closed path systems the autocovariances between vertical windspeed fluctuations and a scalar concentrations fluctuations which is used to determine the time for the air to flow down the tube is also output to file.

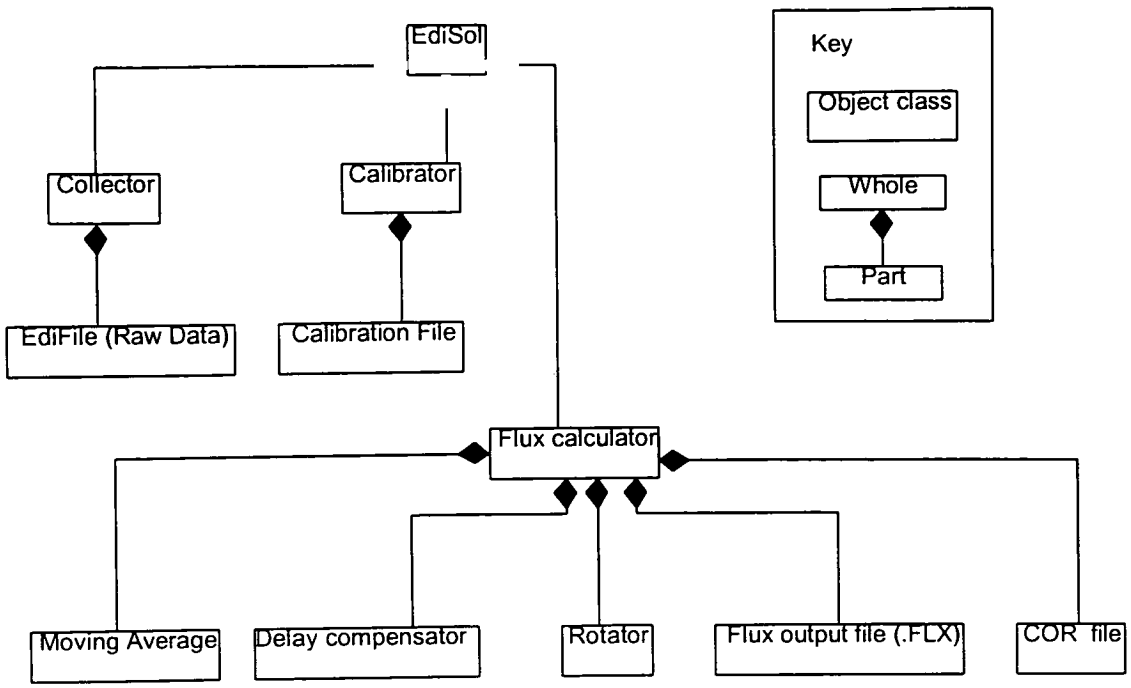

Figure 3-4 Class diagram for EdiSol showing the classes of objects that EdiSol consists of. See text for further description.

The Calibrator gathers data from sensors and delivers it to the computer. Two types of collector have been implemented, the Solent R2 and the dataset which takes the data from disk files. The Calibrator takes the data as output by the collector and converts it to appropriate units for further processing or reporting. The flux calculator contains objects to do some of the processing the rest of which is done by internal routines. The objects contained by the flux calculator are: moving average, delay compensator (e.g. for the gas sample to travel down the tube), rotator to do co-ordinate rotation and files for final output.

3.5 Summary

There was a need for an eddy covariance system to measure sensible heat, CO_2 and water vapour (latent heat) fluxes suitable for long-term monitoring. This required sensors with stable calibrations and software capable of calculating fluxes as the data was acquired (real-time processing) to reduce the time required to process the data after acquisition. The gas analyser available that fit the specifications was a closed path device. This made inevitable a lag between wind velocity measurements and gas

concentration measurements as the sampled air travelled down the tube from close to the anemometer sonic path to the gas analyser. The lag could not be assumed constant and was estimated by calculating lagged cross-correlations in real-time. Co-ordinate rotations were also made in real-time.

WPL corrections, corrections for the influence of vapour pressure on the relationship between sonic and true temperature and corrections for the under estimation of high and low frequency fluctuations were not included in the flux software (EdiSol).

Object-orientated design and Object Pascal were used in the design and implementation of the flux software, EdiSol, to make the software easier to maintain and extend.

Chapter 4 Post collection processing of eddy covariance data

4.1 Introduction

Routine corrections have to be made to the output of the logging software, EdiSol: a) frequency corrections (Moore, 1986) must be applied to the fluxes and variances and b) sensible heat flux must be derived from sonic sensible heat flux and evaporation. In this study, corrections also had to be made to the speed of sound as measured by the Solent 1012R2 anemometer when the temperature was below 5 °C, thus influencing sonic temperature and sonic sensible heat flux. In addition to the above corrections, a number of quality checks were also made on the data. The co-ordinate rotation angles were checked for large angles and large variation in angles that would indicate local flow disturbance and, therefore, inaccurate fluxes. Monin-Obukov variance-stability relationships were also examined. The eddy covariance technique used to calculate the fluxes depends upon stationarity (statistics not varying with time) and the algorithm for calculating the average (in this case, an ARMA) from which the fluctuations are calculated to estimate covariance. Data for two days covering varied conditions were used to investigate stationarity and the effect of using different time constants for the ARMA.

The sample tube was 28 m long and had an inner diameter (id) of 6 mm giving a length/id ratio of 4667. This is considerably larger than the threshold length/id ratio of 1000 over which temperature fluctuations may be assumed to be damped to negligible levels (Rannik *et al.*, 1997). Therefore, the temperature fluctuations were assumed negligible and the CO_2 concentration was calculated as if it were measured in dry air dispensing with WPL corrections. However, WPL correction would be necessary if a open-path IRGA were used or the CO_2 concentration were input to the software as measured in air of varying vapour pressure.

4.2 True sensible heat flux from sonic sensible heat flux

The air temperature T_a (K) is calculated from T_s (K) using (Schotanus *et al.*, 1983; Kaimal and Gaynor, 1991):

$$T_a = \frac{T_s}{1 + 3.210^{-4} h} \qquad (4\text{-}1)$$

The sensible heat flux, H, is given by :

$$H = \frac{PM_d}{\Re T_a} C_p \left(\overline{w' T_s'} - 3.2 \cdot 10^{-4} \overline{T}_a \overline{w' h'} \right) \qquad (4\text{-}2)$$

(Schotanus *et al.*, 1983; Kaimal and Gaynor, 1991). The second term in parentheses compensates for the difference between sonic and real temperature. Equation 8 in Schotanus *et al.* (1983) includes a third term to correct for the wind speed normal to the sonic path. However, Schotanus *et al.* (1983) assume a vertical sonic path which is inappropriate for anemometers where the speed of sound is not measured on a vertical axis such as the Solent 1012R2. In EdiSol, the speed of sound is corrected for wind speed normal to the sonic path by equation 3-10 before sonic temperature is calculated. By substituting equations 3-21 and 3-24, equation 4-2 can be expressed in terms of H_s and E.

$$H = H_s - 3.2 \cdot 10^{-4} M_a C_p \overline{T}_a E \qquad (4\text{-}3)$$

where M_d is the molar mass of dry air (0.028965 kg mol^{-1}). Schotanus *et al.* (1983) report corrections in the order of 10 %. For the 1996 data collected at SSA OBS the average half-hour correction was 2 % with values from zero to 10 % or higher when $|H_s| < 0$. The average half-hourly correction as a function of E was $2.7E$ (W m^{-2}) see Figure 4-1.

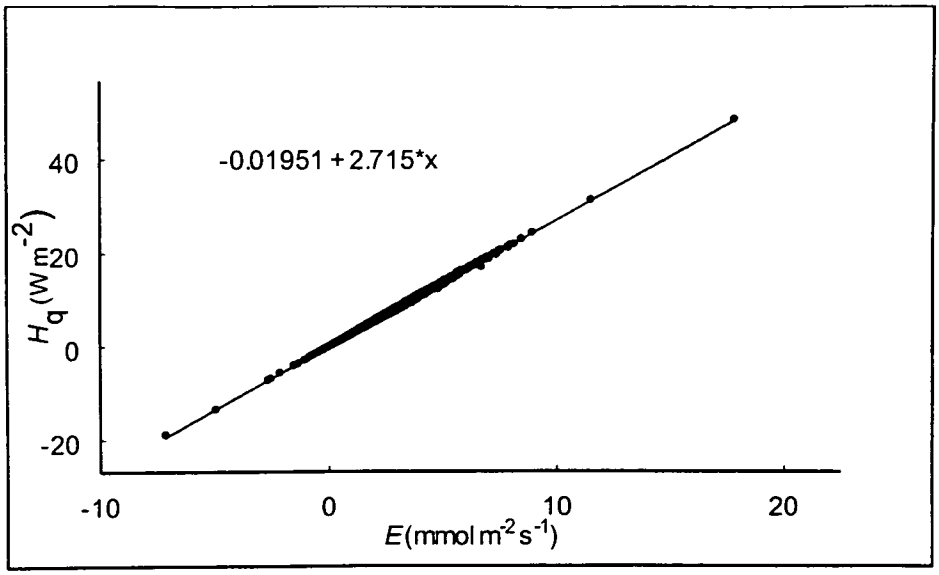

Figure 4-1 Regression plot of H_q (the correction subtracted from H_s to obtain H, equation 4-3) against evaporation, E. N = 10800 and $r^2 = 0.9995$.

4.3 Solent 1012R2 sonic temperature at low true temperatures

Gill specify an operating temperature range of 5 °C to 40 °C for Solent 1012R2 ultrasonic anemometers (Gill Instruments, Lymington, UK), however, the anemometers have been used successfully down to -40 °C (Peters *et al.*, 1993; Grelle *et al.* 1994) and in 1994 a Solent 1012R2 serial number 20 showed no change in calibration below 5 °C down to 1°C (Figure 4-2). On checking the output after installing the Solent anemometer serial number 83 (at -20 °C), it was noticed that temperature derived from the speed of sound was too high (Figure 4-3). R2 serial number 58 (Solent 58) not installed in the measuring system was then used to investigate the calibration of the R2 at low temperatures.

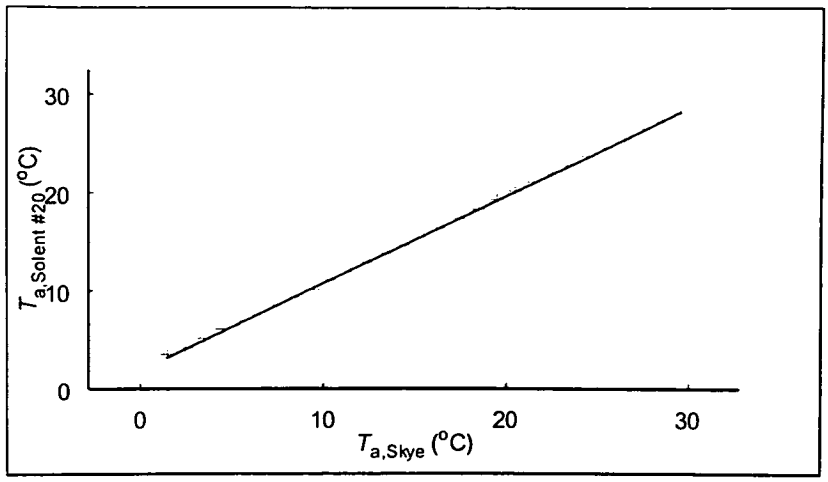

Figure 4-2 Regression plot of mean air temperature derived from Solent R2 serial number 20, $T_{a,Solent\#20}$, against air temperature measured by the Skye instruments temperature and humidity probe, $T_{a,Skye}$, in 1994. Each point is the mean value of $T_{a,Solent}$#20 for a 1 °C interval of $T_{a,Skye}$. The point is plotted at the middle of the $T_{a,Skye}$ interval. $T_{a,Solent}$ was derived using equation 4-1.

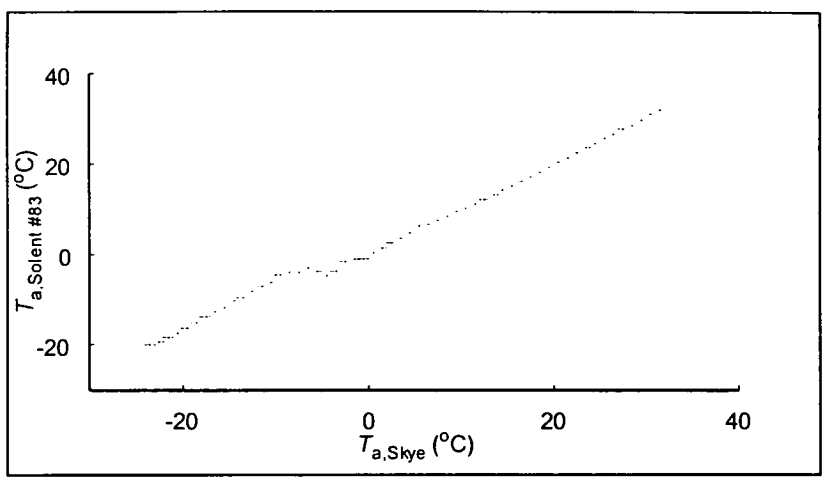

Figure 4-3 Scatter plot of mean air temperature derived from Solent R2 serial number 83, $T_{a,Solent\#83}$, against air temperature measured by the Skye instruments temperature and humidity probe, $T_{a,Skye}$, in 1996. Each point is the mean value of T_a,Solent#83 for a 1 °C interval of $T_{a,Skye}$. The point is plotted at the middle of the $T_{a,Skye}$ interval. $T_{a,Solent}$ was derived using equation 4-1.

Solent 58 was put in a box lined with expanded polystyrene supported so the transducers were away from the sides of the box. A thermocouple was positioned in the box near the transducers and connected to a datalogger (21x, Campbell Scintific, Logan, UT, USA) using the datalogger panel temperature thermistor as the reference for the thermocouple. The box was left open to the outside to cool at an ambient

temperature of –20 °C. When the anemometer temperature had fallen to a steady value the lid of the box was closed and the box was brought into the hut, where the temperature was 20 °C, and allowed to warm up while the thermocouple output was recorded and the sonic temperature was calculated and recorded by EdiSol from the speed of sound output from the R2. At –20 °C, saturated vapour pressure is 0.125 kPa, equivalent to h = 1.25 mmol mol^{-1}, and T_s/T_a = 1.0004 (equation 4-1) and therefore, T_s was assumed to equal T_a in this experiment. The results of this experiment are shown in Figure (4-4) and a correction equation was derived:

$$T_s = 2\times10^{-6}T^5_{s,58} + 5\times10^{-6}T^4_{s,58} - 0.0022T^3_{s,58} + 0.0111T^2_{s,58} + 1.4429T_{s,58} - 3.7263 \quad (4\text{-}4)$$

where $T_{s,58}$ is uncorrected sonic temperature reported by Solent R2 serial number 58.

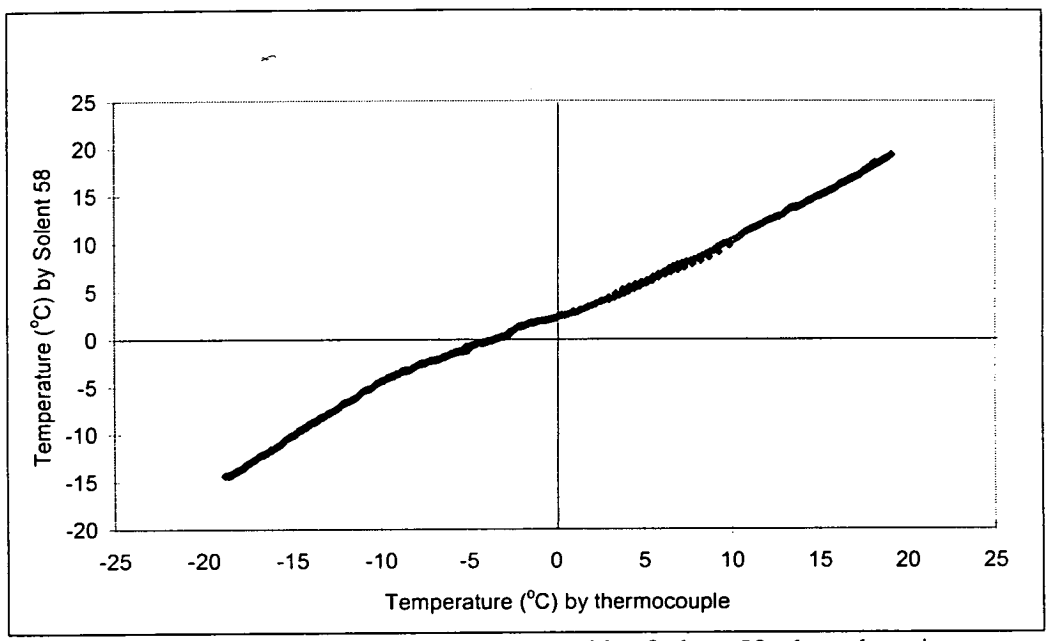

Figure 4-4 Uncorrected temperature reported by Solent 58 plotted against temperature measured by a thermocouple. Data points represent two minute means while the anemometer warmed from –20 °C in an insulated box.

Air temperature at 2 m height measured using Solent 58 after correction for low true temperature (equation 4-4) and conversion from sonic temperature to air temperature (equation 4-1), $T_{a,Solent\#58,}$ was compared with air temperature also measured at 2 m height but 4 m lateral separation under the trees using a psychrometer dry bulb (model VP1, Delta-T Devices, Cambridge, UK), $T_{a,VP1,2m}$ (Figure 4-5). The regression equation was, $T_{a,Solent\#58}$ = -0.27(±0.016) + 0.95(±0.0012) $T_{a,VP1,2m}$ where

the error terms are 95 % confidence intervals, N was 8442 and r^2 was 0.9967 and RMSE was 0.65 °C. The polynomial (equation 4-4) fails when T_a < -25 °C but the relationship is quite good bearing in mind that the sensors are 4 m apart below the canopy.

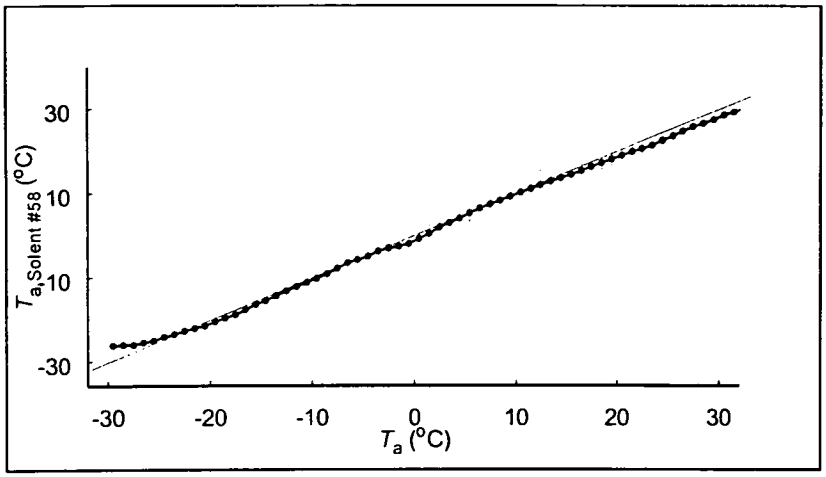

Figure 4-5 Scatter plot of mean air temperature derived from Solent R2 serial number 58, $T_{a,Solent\#58}$ after correction for low true temperature against air temperature measured by the VP1 psychrometer dry bulb, T_a, in 1996. Each point is the mean value of $T_{a,Solent\#58}$ for a 1 °C interval of T_a. The point is plotted at the middle of the T_a interval. $T_{a,Solent\#58}$ was derived using equation 4-1 after correction using equation 4-4. The bars represent minimum and maximum value and the 1:1 line is shown.

The correction equation for Solent 58 was tried with Solent 83 which was the anemometer used in the EC system at the top of the tower but the calibration of the two anemometers were too different. The sonic temperature given by Solent 83 at 26 m was then calibrated by cross-reference to the Skye instruments temperature and humidity probe at 24 m over short enough periods for the calibration to be approximately linear. The fully corrected air temperature derived from Solent 83 is compared with air temperature measured by Skye instruments temperature and humidity probe in Figure 4-6.

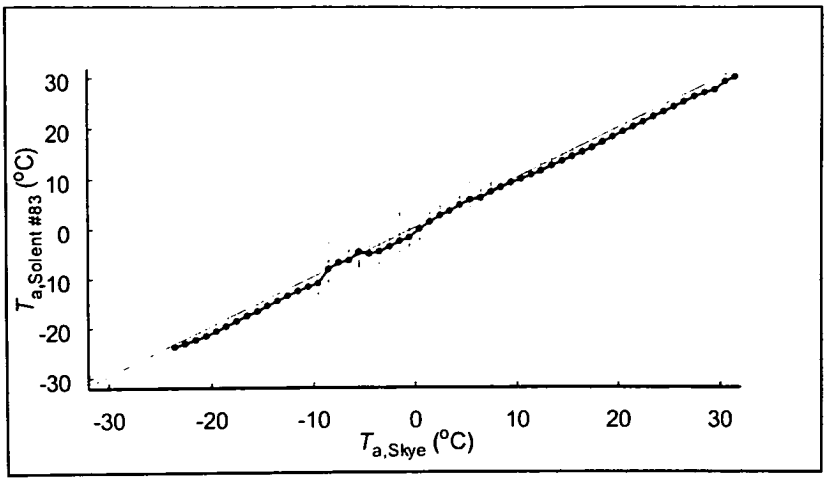

Figure 4-6 Scatter plot of mean air temperature derived from Solent R2 serial number 83, $T_{a,Solent\#58}$, after correction for low true temperature against air temperature measured by the Skye instruments temperature and humidity probe, $T_{a,Skye}$, in 1996. Each point is the mean value of $T_{a,Solent\#83}$ for a 1 °C interval of $T_{a,Skye}$. The point is plotted at the middle of the $T_{a,Skye}$ interval. $T_{a,Solent\#83}$ was derived using equation 4-1. The bars represent minimum and maximum value and maximum value and the 1:1 line is shown.

4.4 Frequency correction

As mentioned in Chapter 3 the flux estimates given by EdiSol must be corrected for non-ideal frequency response of the sensors and measuring system. Following Moore (1986) by using functions to model the frequency response of the components of the system and a function to model the cospectral distribution by convolution, the proportion of the flux that is measured, P_F, may be estimated by:

$$P_F = \frac{F_{meas}}{F} = \frac{\int_0^\infty T_{wx}(n) C_{wx}(n) dn}{\int_0^\infty C_{wx}(n) dn} \qquad (4\text{-}5)$$

where F_{meas} is the "measured" flux given by EdiSol, F is the true flux, $T_{wx}(n)$ is the total system transfer function, and $C_{wx}(n)$ is the cospectral distribution associated with F. The frequency response functions are given as simple gain functions where the variable of interest and its fluctuations are a function of frequency and as transfer functions which are the ratio of attenuated, P_{out}, to unattenuated, P_{in}, power spectra

(P_{out} /P_{in}) where power spectra give the fraction of variance of a time series as a function of frequency.

For EdiSol, frequency response functions are required for the moving average, gas analyser CO_2 and water vapour concentration measurements, sensor separation, path averaging by the anemometer, sensor frequency response mismatch and sampling the gas down a tube to the closed path gas analyser. For each flux the appropriate frequency response functions are multiplied to give a total frequency response function associated with the flux. The equation for each transfer function is shown below and plotted in Figure 4-7. Natural frequency is represented by n and f is normalised frequency given by $f = n\ (z\text{-}d)/u$.

The frequency response of the moving average which is a digital representation of an analogue RC filter (equation 3-8) can be described by the gain function of a first-order high-pass filter to a very good approximation for frequencies smaller than the Nyquist frequency (Moore, 1986) (Figure 4-7a)

$$G_r(n) = \frac{2\pi n \tau_r}{\sqrt{1 + (2\pi n \tau_r)^2 / \eta}} \qquad (4\text{-}6)$$

where $\eta = e^{\left(\frac{-\Delta t}{\tau}\right)}$, τ is the time constant of the running mean, $\Delta t = 1/n_S$, (n_S = sample rate) and t_r, the effective time constant is $t_r = \eta[n_S(1 - \eta)]^{-1}$

The dynamic response of the sonic anemometer and gas analyser may be described by a simple first-order gain function (Moore, 1986) giving:

The sonic anemometer dynamic response time gain function is

$$G_{da}(n) = \frac{1}{\sqrt{1 + (2\pi n t_a)^2}} \qquad (4\text{-}7)$$

where τ_{ra} is the response time of the sonic anemometer (Figure 4-7f).

IRGA dynamic response time for CO_2,

$$G_{dc}(n) = \frac{1}{\sqrt{1 + (2\pi n \tau_{rc})^2}} \tag{4-8}$$

where τ_{rc} is the response time of the IRGA (Figure 4-1f).

IRGA dynamic response time for water vapour is

$$G_{dh}(n) = \frac{1}{\sqrt{1 + (2\pi n \tau_{rh})^2}} \tag{4-9}$$

where τ_{rh} is the response time of the IRGA (Figure 4-1f).

If the covariance of two signals is to be calculated from sensors of different response times, the covariance will be underestimated because of a phase shift introduced between the signals from the different sensors. The underestimation increases with increasing response time mismatch. The transfer function for *sensor response mismatch* can be expressed as (Zeller *et al.*,1989),

$$T_{mc}(n) = \frac{1 + (2\pi n)^2 \tau_{ra} \tau_{rc}}{\sqrt{\left[1 + (2\pi n \tau_{ra})^2\right]\left[1 + (2\pi n \tau_{rc})^2\right]}} \tag{4-10}$$

$$T_{mh}(n) = \frac{1 + (2\pi n)^2 \tau_{ra} \tau_{hc}}{\sqrt{\left[1 + (2\pi n \tau_{ra})^2\right]\left[1 + (2\pi n \tau_{rh})^2\right]}} \tag{4-11}$$

where T_{mc} and T_{mh} are the transfer functions for the mismatch between anemometer and CO_2 and water vapour signals from the IRGA respectively. These functions are graphed in Figure 4-7e.

The sonic anemometer measures windspeed over a certain path length (14.5 cm for the Solent 1012R2), averaging the windspeed along this path and is, therefore, unable to resolve small eddies. The transfer function *path (or line) averaging* for the vertical wind component is approximated closely by:

$$T_{wa}(f_a) = \frac{2}{\pi f_a}\left[1 + \frac{e^{-2\pi f_a}}{2} - \frac{3\left(1 - e^{-2\pi f_a}\right)}{4\pi f_a}\right] \tag{4-12}$$

where $f_a = np_a / \overline{U}$, and p_a is the path length of the anemometer (Moore, 1986) (Figure 4-1d).

Turbulent eddies are of finite size and to measure exactly the same eddy, sensors would have to be in exactly the same place. The transfer function for the effect of sensors being separated can be described by:

$$T_s(f_s) = e^{(-9.9 f_s^{1.5})} \qquad (4\text{-}13)$$

where $f_s = ns / \overline{U}$, and s is the separation of the instruments if the sensors are close enough for the attenuated frequency to lie in the inertial subrange (Moore, 1986) (Figure 4-1c).

When using a closed path gas analyser the air is ducted down a tube from close to the anemometer to the gas analyser and the fluctuations in gas concentrations decrease as the air travels down the tube. The tube acts as a low-pass filter. When flow is laminar, there is a gradient in windspeed from the tube wall, where air is slowed by friction with the tube, to the centre of the tube where the airflow is fastest. This gradient in windspeed damps the fluctuations by mixing or "smearing" air together that entered the tube at slightly different times. As the air travels down the tube, mixing by diffusion also takes place but this effect is small. If the airflow is turbulent, despite the greater mixing of the air, the damping of fluctuations is less with turbulent flow. When the flow is turbulent the windspeed gradient from tube wall to the centre of the tube is small and fluctuations are "smeared" much less than in laminar flow. Much work on estimating flux loss caused by the use of sample tubes has been done for both laminar and turbulent flow (Taylor, 1953, 1954; Philip, 1963; Leuning and Moncrieff, 1990; Lenschow and Raupach, 1991 and Massam, 1991; Leuning and King, 1992; and Leuning and Judd, 1996)

The transfer functions describing the attenuation of the concentration fluctuations take the form:

$$T_t(n) = \exp\left(\frac{-\Lambda r X n^2}{U_t}\right) \qquad (4\text{-}14)$$

where $\Lambda$is an attenuation coefficient, r is the tube radius (m), X is the tube length (m) and U_t is the windspeed down the tube (m s^{-1}).

Taylor (1953) showed that when the flow is laminar, the attenuation coefficient is given by:

$$\Lambda = \frac{-0.82\,\mathrm{Re}\,\nu}{D} \tag{4-15}$$

where $\mathrm{Re} = 2rU_t/\nu$ and is the Reynolds number, ν is the kinematic viscosity (m^2 s^{-1}), D is the diffusion coefficient (m^2 s^{-1}) for the gas species in question.

For turbulent flow Lenschow and Raupach (1991) used turbulent flow theory of Taylor (1954) to derive the attenuation coefficient given by:

$$\Lambda = -160\,\mathrm{Re}^{-1/8} \tag{4-16}$$

The total transfer function for sensible heat and momentum fluxes are

$$T_{wT}(n) = T_{uw}(n) = G_r(n)^2.G_{da}(n)^2.T_{wa}(n) \tag{4-17}$$

and for water vapour and CO_2 fluxes are

$$T_{wh}(n) = T_t(n)^{1/2}.G_r(n)^2.G_{da}(n).G_{dh}(n).T_{mh}(n).T_{wa}(f_a)^{1/2}.T_{wi}(f_i)^{1/2}.T_s(f_s) \tag{4-18}$$

$$T_{wc}(n) = T_t(n)^{1/2}.G_r(n)^2.G_{da}(n).G_{dc}(n).T_{mc}(n).T_{wa}(f_a)^{1/2}.T_{wi}(f_i)^{1/2}.T_s(f_s) \tag{4-19}$$

These are shown in Figure 4-7g, for a wind speed of 3.0 m s^{-1}.

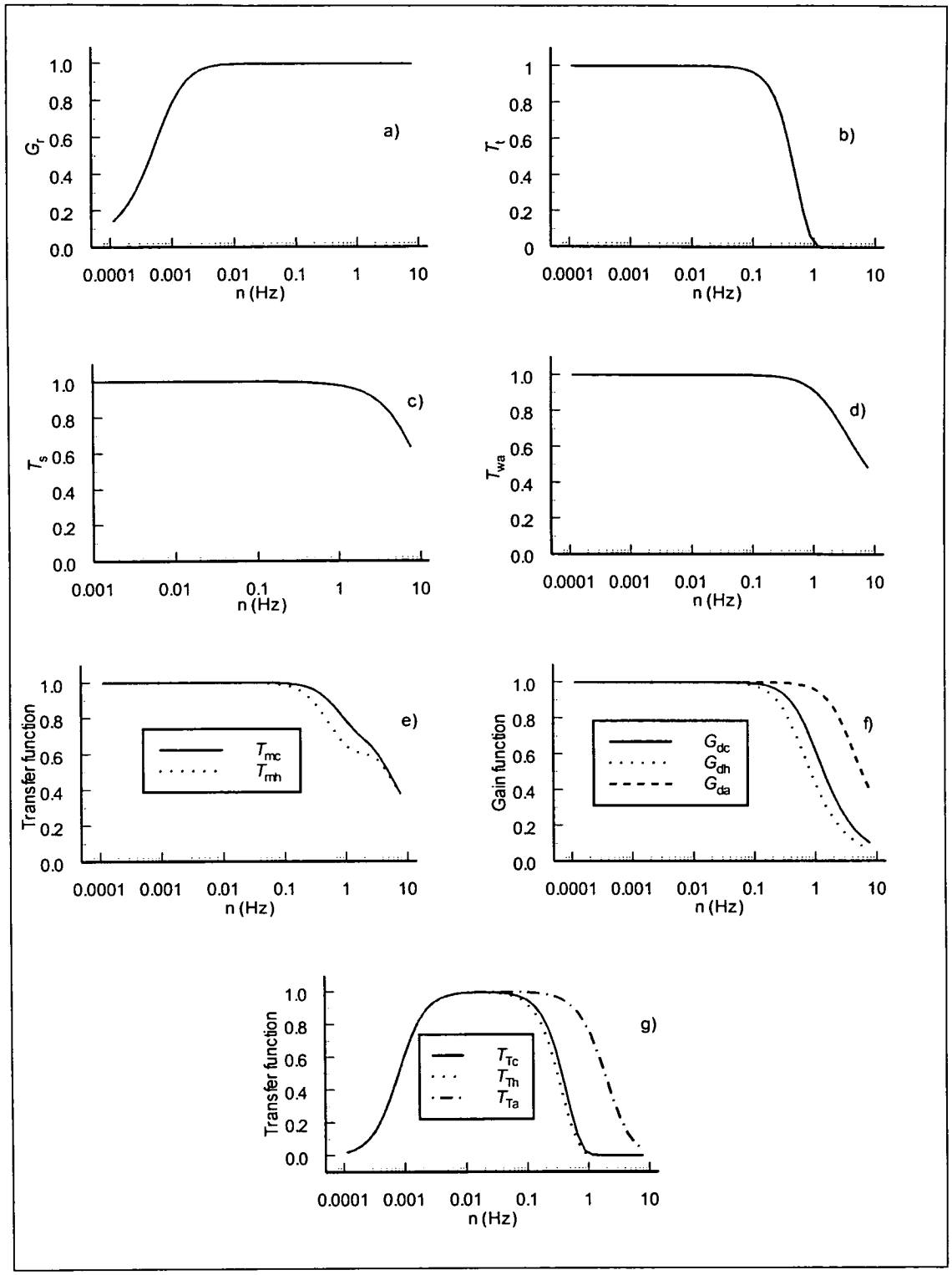

Figure 4-7 Individual and total transfer functions for EdiSol as configured for BOREAS in 1996.

The cospectral and spectral models used in this analysis are from Kaimal *et al.* (1972) normalised by Moore (1986) so that the integral equals unity over an unspecified frequency range.

The cospectrum of $w\alpha$ (α is a subscript denoting the variable of interest: temperature, CO_2 concentration or water vapour concentration) for stable conditions is given as follows:

$$nC_{w\alpha}(n) = \frac{f}{A_{w\alpha} + B_{w\alpha} f^{2.1}} \qquad (4\text{-}20a)$$

where

$$A_{w\alpha} = 0.28\left[1 + 6.4\left(\frac{z\text{-}d}{L}\right)\right]^{0.75} \qquad (4\text{-}20b)$$

and

$$B_{w\alpha} = 2.34 A_{w\alpha}^{-1.1} \qquad (4\text{-}20c)$$

The same form of equation can be used for momentum

$$nC_{wu}(n) = \frac{f}{A_{wu} + B_{wu} f^{2.1}} \qquad (4\text{-}21a)$$

where

$$A_{wu} = 0.124\left[1 + 7.9\left(\frac{z\text{-}d}{L}\right)\right]^{0.75} \qquad (4\text{-}21b)$$

and

$$B_{wu} = B_{w\alpha} \qquad (4\text{-}21c)$$

For unstable conditions the cospectral model for sensible heat is:

$$nC_{wT}(n) = \frac{12.92f}{(1 + 26.7f)^{1.375}} \quad \text{for } f < 0.54 \qquad (4\text{-}22a)$$

$$nC_{wT}(n) = \frac{4.378f}{(1 + 3.8f)^{2.4}} \quad \text{for } f \geq 0.54 \qquad (4\text{-}22b)$$

There are no such cospectral models for CO_2 and water vapour fluxes and the above model is used.

The cospectral model for momentum ($\overline{u'w'}$) in unstable conditions is given as follows:

$$nC_{uw}(n) = \frac{20.78f}{(1+31f)^{1.575}} \qquad \text{for } f < 0.24 \qquad \text{(4-23a)}$$

$$nC_{uw}(n) = \frac{12.66f}{(1+9.6f)^{2.4}} \qquad \text{for } f \geq 0.24 \qquad \text{(4-23b)}$$

The spectral models are similar to the cospectral models. For stable conditions the spectral model for temperature variance is used for all scalars and is given by:

$$nS_{TT}(n) = \frac{f}{A_T + B_T f^{2.1}} \qquad \text{(4-24a)}$$

where

$$A_T = 0.096 + 0.644\left(\frac{z-d}{L}\right)^{0.6} \qquad \text{(4-24b)}$$

and

$$B_T = 3.124A_T^{-2/3} \qquad \text{(4-24c)}$$

For unstable conditions the model scalar spectra becomes:

$$nS_{TT}(n) = \frac{14.94f}{(1+24f)^{5/3}} \qquad \text{for } f < 0.15$$

$$nS_{TT}(n) = \frac{6.827f}{(1+12.5f)^{2.4}} \qquad \text{for } f \geq 0.15 \qquad \text{(4-25)}$$

For the instruments used in this study, the flux losses are less than 2 % for sensible heat flux, and range from 10 to about 20 % for latent heat and CO_2 fluxes, being largest at low wind speeds.

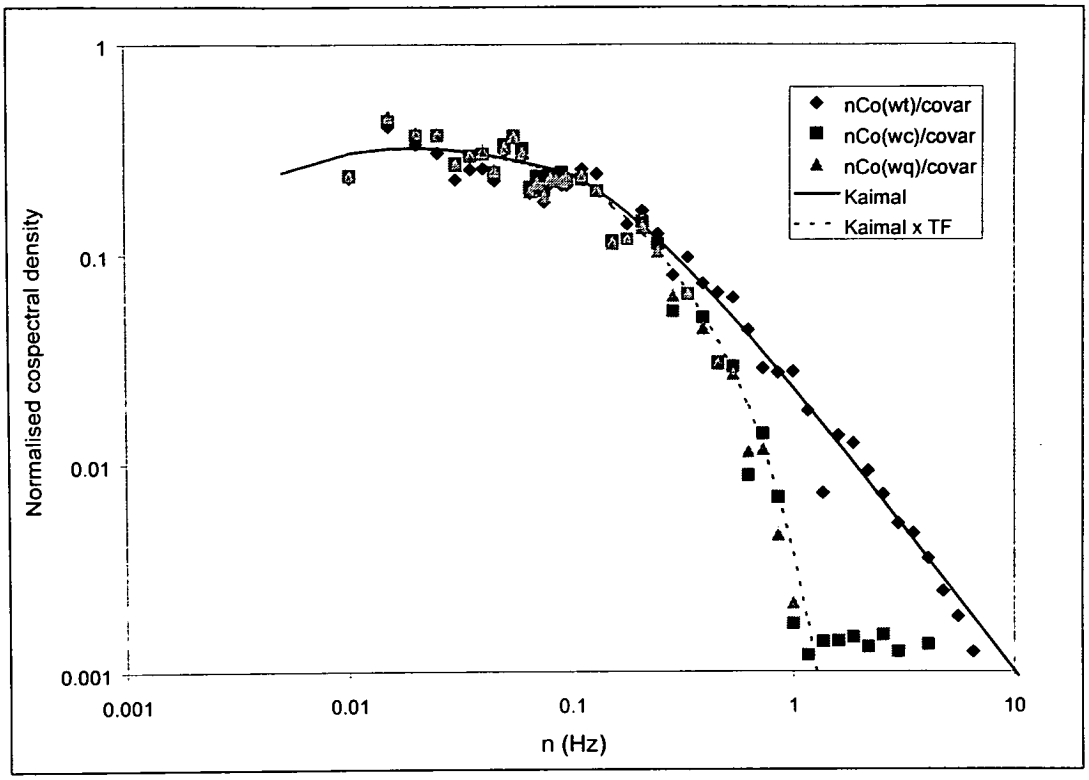

Figure 4-8 Averaged cospectra of temperature, CO_2 and water vapour with w. Also shown is the Kaimal model C_{wT} and the Kaimal model multiplied by the transfer function for CO_2. Data from 12:00 to 15:00 20th August 1996 (day 223). The model spectra were re-normalised for the frequency range used.

If the frequency corrections are correct, the unmodified Kaimal $\overline{w'T'}$ cospectral model will fit a measured cospectrum and the same model convolved with the total transfer function for the appropriate flux will fit measured CO_2 and water vapour flux cospectra (Figure 4-8). Figure 4-8 measure and modelled cospectra showing that the frequency correction scheme worked in unstable conditions. At night, however, when mixing was low, the measured spectra and cospectra were extremely noisy and did not fit models, therefore, the frequency corrections do not work. Under those conditions the turbulent fluxes are very low being limited by the lack of turbulent mixing and so over 24 hours the error is small.

4.5 Co-ordinate rotation angles

Co-ordinate rotation was introduced to the set of algorithms used in eddy covariance to reduce errors when measuring over non-simple terrain and to relax sensor levelling requirements (McMillen, 1986, 1988).

The sonic anemometer was not aligned precisely vertical but it was fixed parallel to the pole on which it was mounted and the pole was within a couple of degrees to the vertical (checked by spirit level). The anemometer and pole were mounted consistently to ensure a consistent orientation of the sonic anemometer. To ensure the fluxes measured were perpendicular to the streamlines, co-ordinate rotation was used. Figure 4-9 shows the second and third rotation angles (see Section 3.1.1.2 for an explanation of rotation angles). The mean second rotation angle for 4 ° bins was between -1 ° and 4 ° and did not increase in variability with any wind direction range bigger than the 4 ° averaging range. This indicates there was no increase in flow distortion at any wind direction. The results for the second rotation angle are similar to those reported for the Harvard Forest flux measurements (Goulden *et al.*, 1996) where the mean second rotation angle for 4 ° wind direction bins was between -2 ° and 3 °. The mean third rotation angle for 4 ° wind direction bins was between -5 ° and 5 ° and the standard deviation for the same wind direction bins was 7 °. The third rotation angle is generally more variable than the second and is not well defined at low windspeed and should be limited to 10 ° (McMillen, 1988). The third rotation angle was larger than 10 ° for less than 1 % of the half-hour averages. The sine wave described by the second rotation angle with wind direction is indicates that the average stream lines form a plane 2.5 ° off the horizontal with the slope running approximately NE to SW and that the anemometer is 1.5 ° off the vertical on the same NE to SW axis.

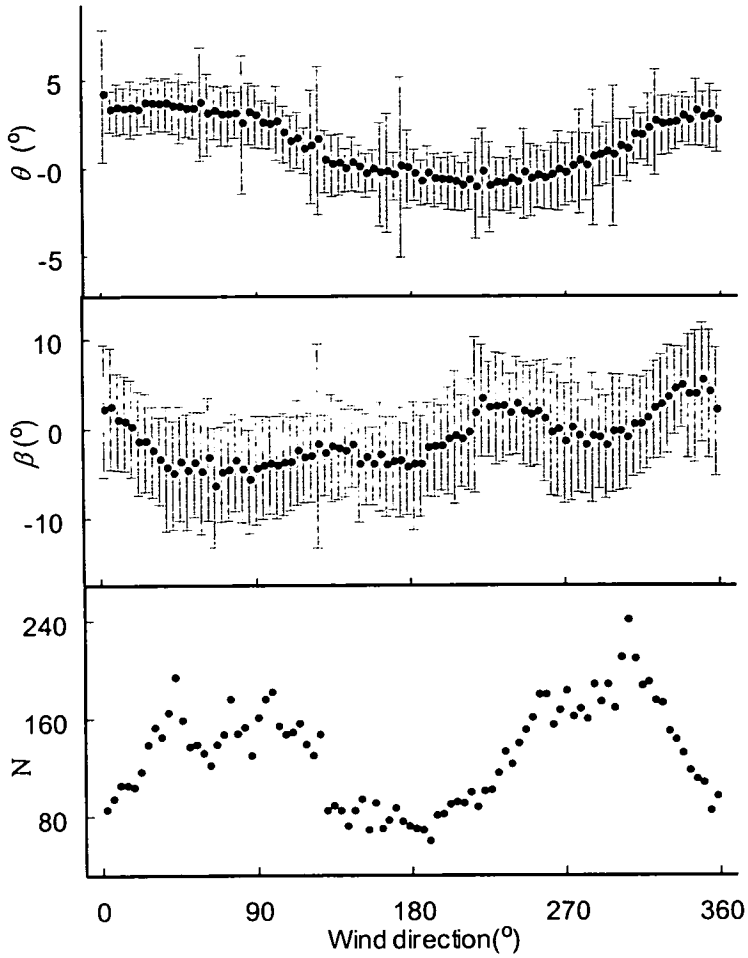

Figure 4-9 Mean rotation angles θ and β plotted against wind direction in 4° intervals. The error bars are standard deviations. The number of observations, N, (half-hour averages) are also shown.

4.6 Similarity relationships

Monin-Obukov similarity theory predicts that statistical properties of the surface-layer depend upon the following four variables: height above the displacement height (z - d), friction velocity (u_*), surface heat flux ($H/\rho C_p$) and buoyancy ($g / \overline{T}$) (where g is gravitational acceleration, m s^{-2}) (Stull, 1988). From these variables a stability parameter, $\zeta = (z-d)/L$, is derived and is positive in stable conditions, zero in neutral conditions and negative in unstable conditions. L is defined in equation 3-30. Monin-Obukov similarity only works when the wind is not calm and $u_* > 0$ (Stull, 1988).

Assuming Monin-Obukov scaling, the normalised variance (dimensionless) of wind velocity or a scalar will be a function of ζ.

Velocity variances are scaled by u_*, and scalar variances, x, are scaled by a derived parameter x_*, where

$$x_* = \overline{w'x'}/u_* \qquad (4\text{-}26)$$

giving the relationships:

$$\sigma_W/u_* = f_W(\zeta) \qquad (4\text{-}27)$$

$$\sigma_X/x_* = f_X(\zeta) \qquad (4\text{-}28)$$

These relationships cannot be derived from first principles and must be determined empirically in ideal conditions, hence the use of a similarity theory (dimension-analysis). The model relationship for σ_w/u_* is (Panofsky and Dutton, 1984; Kaimal and Finnigan, 1994):

$$\sigma_w/u_* = 1.25\,[1 - 3(\zeta)]^{1/3} \qquad (4\text{-}29)$$

and for temperature fluctuations is (Kaimal and Finnigan, 1994):

$$\sigma_T/T_* = 2\,[1 - 9.5(\zeta)]^{-1/3} \qquad (4\text{-}30)$$

Foken and Wichura (1996) present:

$$\sigma_w/u_* = 2.0\,(-\zeta)^{1/6} \quad \text{when } \zeta < -1$$

$$\sigma_w/u_* = 2.0\,(-\zeta)^{1/8} \quad \text{when } -1 < \zeta < -0.0625 \qquad (4\text{-}31)$$

$$\sigma_w/u_* = 1.41 \quad \text{when } -0.0625 < \zeta < 0$$

and:

$$\sigma_T/T_* = 1.00(-\zeta)^{-1/3} \quad \text{when } \zeta < -1$$

$$\sigma_T/T_* = 1.00\,(-\zeta)^{-1/4} \quad \text{when } -1 < \zeta < -0.0625 \qquad (4\text{-}32)$$

$$\sigma_T/T_* = 0.50(-\zeta)^{-1/2} \quad \text{when } -0.0625 < \zeta < 0$$

The results of Equation 4-31 are very close to those of Equation 4-29 except when $\zeta < -1$ when the exponent is 1/6 instead of 1/3. Equation 4-32 is a close approximation to Equation 4-30 except when $-0.0625 < \zeta < 0$ and Equation 4-32 is not constant.

Foken and Wichura (1996) suggest those observations which meet the criterion that the normalised variance is within 30 % of the model, may be considered of good quality and those that fall outside this limit are of intermediate to bad quality. When assessing data quality the surface over which the measurements were made and the purpose for which the data are to be used must be taken into consideration. The rougher surface of forest and larger eddy size over this surface causes turbulence to be more variable than over flat grass land or crops and the criteria may be more relaxed over forest. In addition, data for land-surface studies where fluxes are of primary interest do not require such well developed turbulence as when universal turbulence functions are being investigated (Foken and Wichura, 1996).

The ratio of σ_w/u_* measured over SSA OBS in 1996 is plotted against ζ in Figure 4-10a for data when $u_* > 0.2$ m s^{-1}, seventeen data points fall outside the "good" criteria of Foken and Wichura (1996). When $u_* < 0.2$ m s^{-1} measured σ_w/u_* was less than 30 % of the model σ_w/u_* and 12 % of the observations in unstable conditions fell into this category. In 88 % of the observations σ_w/u_* was within 30 % of the model in unstable conditions. Despite the different exponent used in Equations 4-29 and 4-31 when $\zeta < -1$ the data present here fit within 30 % of both models though the data shows a slope of 1/3 (Figure 4-10a).

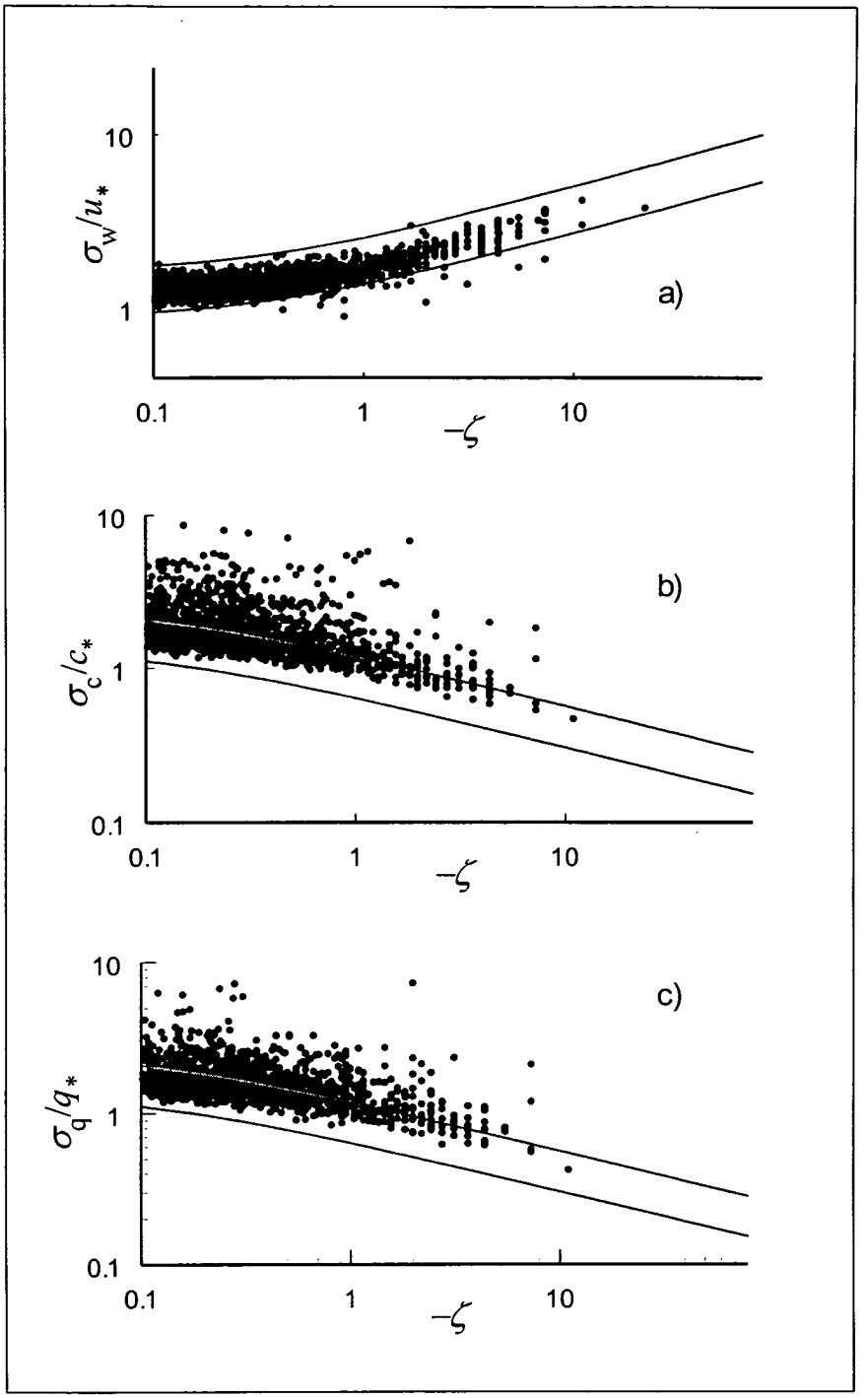

Figure 4-10 Scatter plots of a) σ_w/u_* b) σ_c/c_* and c) σ_q/q_* against ζ. The lines are ±30 % of the ideal ratio: a) $\sigma_w/u_* = 1.25\,[1 - 3(z/L)]^{1/3}$ (Panofsky and Dutton, 1984; Kaimal and Finnigan, 1994) or b) and c) $\sigma_T/T_* = 2\,[1 - 9.5(z/L)]^{-1/3}$ (Kaimal and Finnigan, 1994). Values of σ_w/u_* were excluded when $u_* < 0.2$ m s^{-1} and values of σ_c/c_* and σ_q/q_* were excluded when $u_* < 0.2$ and $c_* < 0.1$ μmol m^{-2} s^{-1} or $q_* < 0.02$ mmol m^{-2} s^{-1}, respectively

σ_c/c_* (Figure 4-10b) and σ_q/q_* (Figure 4-10c) were much noisier than σ_w/u_*.

Assuming that scalars were transported in a similar way, the model of σ_T/T_* as a

function of ζ (equation 4-30) was used as the model for σ_c/c_* and σ_q/q_* as functions of ζ. When observed values of σ_c/c_* and σ_q/q_* were compared with the model, 55 % of σ_c/c_* and 48 % of σ_q/q_* were more than 30 % larger than model (none were smaller). Large values (between 10 and 1000) of σ_c/c_* and σ_q/q_* occurred when $\sigma_c >$ 1 μmol m^{-2} s^{-1} or $\sigma_q > 1$ mmol m^{-2} s^{-1}, respectively, were excluded from Figure 4-10. Most of these occurred in the morning during the onset of turbulent mixing when instationarity is common (see section 4.7) and accounted for ten per cent of the values of σ_c/c_* and and 0.4 % of σ_q/q_*. Instationarity is more common with CO_2 than with water vapour in the morning. CO_2 fluxes change direction and CO_2 stored in the air below the eddy covariance sensors during the night is flushed out. In contrast, water fluxes are almost unidirectional (evaporation) and water vapour concentration profiles change little.

The remainder of the observations (30 %) when values of σ_c/c_* were larger than 10 (up to 3300) were when $c_* < 0.1$ μmol m^{-2} s^{-1}. For water vapour, the remainder of the observations (20 %) when values of σ_q/q_* were larger than 10 (up to 2150) were when $q_* < 0.02$ mmol m^{-2} s^{-1}. The threshold values of c_* and q_* scale approximately with typical values of their respective fluxes.

These large values of σ_c/c_* and σ_q/q_* may be caused by larger than expected σ_c and σ_q or smaller than expected $\overline{w'c_c'}$ and $\overline{w'h_c'}$. Noise in the measurements of the scalars that did not correlate with w would cause an overestimation of the variance but inspection of power spectra do not show this but that variance is attenuated by the tube. Frequency corrections for the variances are carried out in the same way as for covariances and are unlikely to cause an overestimation by such an amount. Additional turbulence caused by obstructions would also cause the similarity statistics to be larger than the model but σ_w/u_* would also be larger than expected. De Breuin *et al.* (1991) and Wichura and Foken (1995) found that inhomogeneity in surface temperature and moisture (but not surface roughness) caused the similarity statistics to be significantly higher than the model. SSA OBS comprised of hummocks and hollows and larger wet and dry areas and, therefore, the larger than expected σ_c/c_* and σ_q/q_* may be caused by surface inhomogeneity.

Though not "good" by Foken and Wichura's criterion, the CO_2 and evaporation fluxes corresponding to σ_c/c_* and σ_q/q_* were not discarded. The justification for this, is that there is some doubt that the σ_T/T_* model was applicable and flux data do not require ideal similarity relationships (Foken and Wichura, 1996).

4.7 Stationarity

For the half-hour flux averages to be areal averages, the turbulence and surface must be homogenous as required by Taylor's hypothesis. If these conditions were met the turbulence statistics would be stationary (i.e. not would not change) during the averaging period. Stationarity of the flux measurements may be investigated by checking how the flux changes with time. A 30 min. averaging period was selected for fluxes measured from towers in BOREAS so as to capture the change in statistics (including fluxes) between averaging periods but for statistics to be almost stationary within the averaging period. Following Foken and Wichura (1996) and Vickers and Mahrt (1996), 10 and 30 minute CO_2 fluxes were calculated using a linear detrend instead of the ARMA and with no co-ordinate rotation so that different rotation periods could not effect the results. The fluxes were calculated for 18:00 CST 31 August to 18:00 CST 1 September 1996. Three of the 10 min CO_2 fluxes were averaged to give averages covering the same time interval as the 30 min averages. An instationarity statistic was calculated:

$$I_c = \frac{F_{c,30} - F_{c,\Sigma}}{F_{c,\Sigma}} \qquad (4\text{-}32)$$

where,

$$F_{c,\Sigma} = \frac{\sum_{i=1}^{3} F_{c,10,i}}{3} \qquad (4\text{-}33)$$

$F_{c,30}$ is the 30 minute CO_2 flux average, $F_{c,10,i}$ is a 10 minute CO_2 flux average and the subscript i = 1, 2 ,3 represents the three 10 minute periods that make up the 30 minute period over which $F_{c,30}$ is calculated.

The time series of $F_{c,30}$ and $F_{c,\Sigma}$ are shown in Figure 4-11a. The night of 30 August was calm and F_c was small because of the lack of turbulent mixing (see Chapter 5). The night of 31 August was turbulent at the beginning and end of the night but calm in between and correspondingly F_c was large and positive (respiration) at the beginning and end of the night during turbulent mixing and small when the wind was calm. The time series are similar but with some values differing when the fluxes are changing, e.g. 08:00 31 August, 10:00 to 12:00 31 August and 05:30 1 September. Figure 4-11b shows the time series of I_c with a reference line of 0.3, a threshold value below which Foken and Wichura (1996) suggested that the flux might be considered stationary. The values of I_c identify the observations noted from Figure 4-11a as being instationary and some observations at night when F_c is small. The longer series of stationary observations are during the day 09:00 to 16:00 on 31 August and 05:00 to 15:00 on 1 September. The end of the stationary period on 1 September at 15:00 coincided with a rain storm.

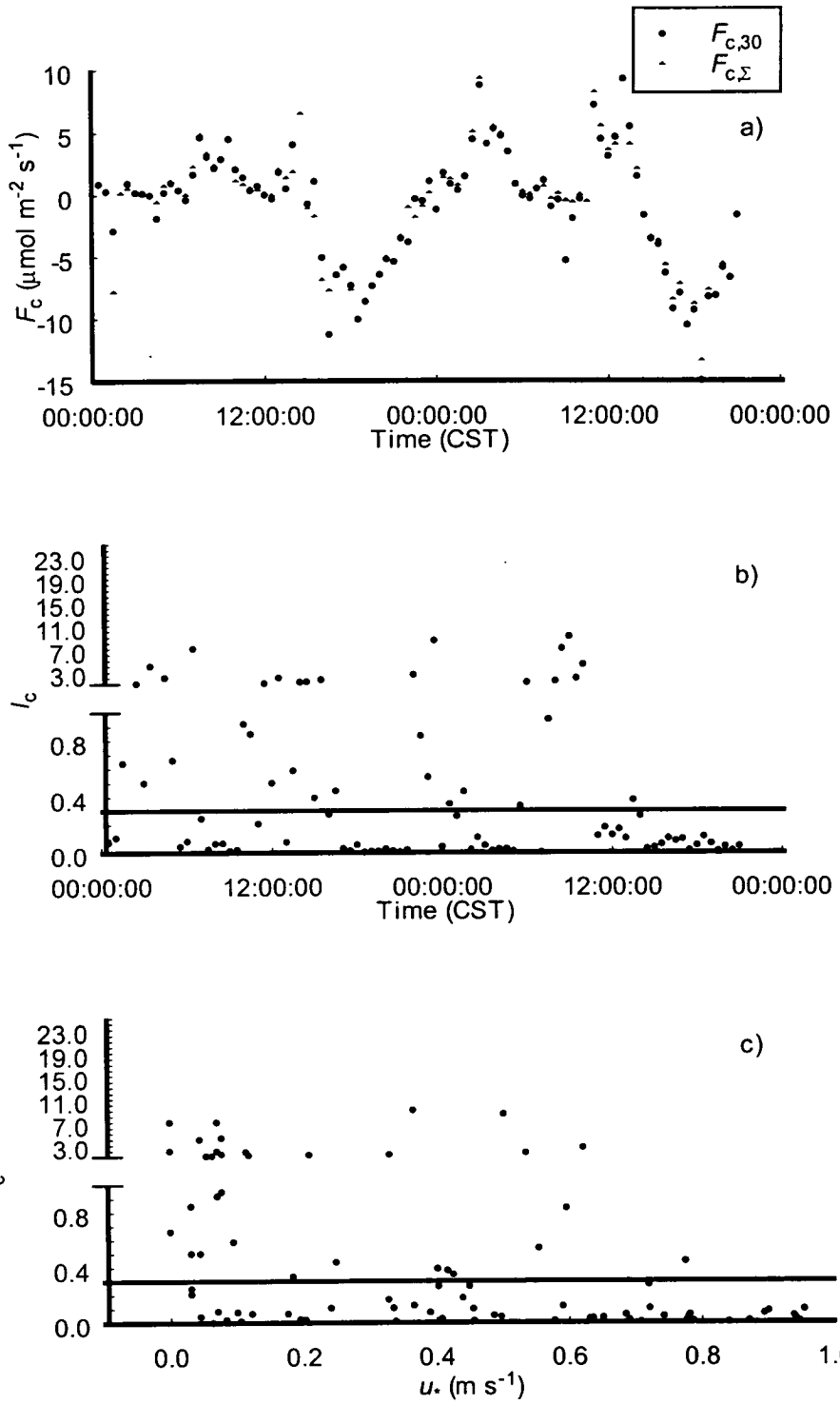

Figure 4-11 a) Time series of 30 minute CO_2 flux averages, $F_{c,30}$, and sums of three 10 minute CO_2 flux averages, $F_{c,\Sigma}$. Each data point represents the value for the 30 minutes before the time shown. b) Time series of I_c with a reference line showing $I_c = 0.3$ the threshold below which Foken and Wichura (1996) suggest the measurement maybe considered stationary. c) Scatter plots of I_c against u_*. The data are from 31 August and 1 September 1996.

Figure 4-11c shows a scatter plot of I_c against u_* showing the number of instationary observations decreasing with increasing u_* : 19 instationary observations when $u_* < 0.2$ m s^{-1}, 5 instationary observations when 0.2 m s^{-1} $\leq u_* < 0.4$ m s^{-1}, 6 instationary observations when 0.4 m s^{-1} $\leq u_* < 0.6$ m s^{-1}, 2 instationary observation when $u_* > 0.6$ m s^{-1}. When u_* is large over several observations, the air will be well mixed and statistics will tend to be stationary, if u_* varies from low to high values between observations, u_* is instationary and other statistics will tend to be instationary and if u_* is small over several observations, the air will not be well mixed and statistics may be intermittently instationary.

4.8 ARMA time constant

EdiSol calculates fluxes by approximating the running mean with an ARMA (AutoRegressive Moving Average) (see Chapter 2). Calculating fluxes by using the arithmetic running mean is expensive in storage and for real time processing an ARMA has been used because it is fast and requires little storage. The ARMA acts as a high pass filter and low frequency information is lost (Moore,1986). A large amount of this lost variation can be estimated by a first order gain function and corrected for (section 4.4) but an ARMA can only use values that were observed before the value being processed and, therefore, there is a phase difference or lag between the observed data and the values of the ARMA which can lead to a further, uncorrected for, loss of variation (Shuttleworth, 1980). As the lag increases the difference between the ARMA and the values of the time series increase and the fluctuations are overestimated. Therefore, to estimate how much the flux is under- or overestimated, the CO_2 flux was calculated for 18:00 CST 31 August to 18:00 CST 1 September 1996 with different τ_r (ARMA time constant): 100 s, 200 s, 400 s (as used for the routine flux calculations), 800 s and 1200 s.

Although the uncertainties in the individual linear regression slopes are large compared with the difference between slopes, the estimates of F_c, after frequency correction as described in section 4.4, increase with τ_r and this effect is larger with increased instationarity (Table 4-1, Figure 4-12 and Figure 4-13).

The computed flux values are a function of the fluctuations estimated using the digital running mean. As τ_r increases, less weight is given to new data and the ARMA lags further behind the true running mean (Equation 3-8). If the running mean is almost stationary the ARMA closely approximates the true running mean and the lag is negligible. However, if there is a trend in the time series the difference between the ARMA and true running mean increases with increasing lag and causes overestimation of the fluctuations and fluxes. Trends in the time series are the cause of instationarity and so overestimation of fluctuations increases with instationarity when an ARMA with large τ_r is used.

When I_c is very small (< 0.05) values of τ_r from 200 s to 1200 s make very little difference to the estimate of F_c, -2.2 to 1 % relative to the value of F_c calculated using an ARMA with τ_r = 400 s (Table 4-1). Because $F_{c,800}$ and $F_{c,1200}$ (the numeric subscript denotes the value of τ_r used) converge they may be more accurate than $F_{c,400}$. The difference in estimates of F_c calculated with different values of τ_r under these, almost stationary, conditions indicate that the frequency corrections do not compensate for the use of small values for τ_r. The use of 400 s for the value of τ_r appears to have been a good compromise with values of $F_{c,400}$ within ca 1 % of $F_{c,800}$ and $F_{c,1200}$ under almost stationary conditions, while avoiding some of the overestimation of variances and covariances caused by larger values for τ_r (Shuttleworth, 1988).

I_c	N	G_{100}	G_{200}	G_{400}	G_{800}	G_{1200}
All	85	0.928±0.012	0.960±0.010	100	1.023±0.024	1.049±0.058
< 0.30	60	0.933±0.015	0.972±0.010	100	1.024±0.018	1.033±0.040
< 0.10	41	0.947±0.013	0.979±0.008	100	1.008±0.018	1.010±0.037
< 0.05	33	0.948±0.016	0.979±0.010	100	1.009±0.020	1.012±0.042

Table 4-1 Gradient of regressions of $F_{c,100}$ against $F_{c,400}$ (G_{100}), $F_{c,200}$ against $F_{c,400}$ (G_{200}), $F_{c,800}$ against $F_{c,400}$ (G_{800}), $F_{c,800}$ against $F_{c,400}$ (G_{800}) for different ranges of I_c (stationarity coefficient) where the subscript denotes the ARMA time constant. All estimates of F_c are corrected for frequency response as described in section 4.4 *Frequency Correction*. Error terms are the standard error.

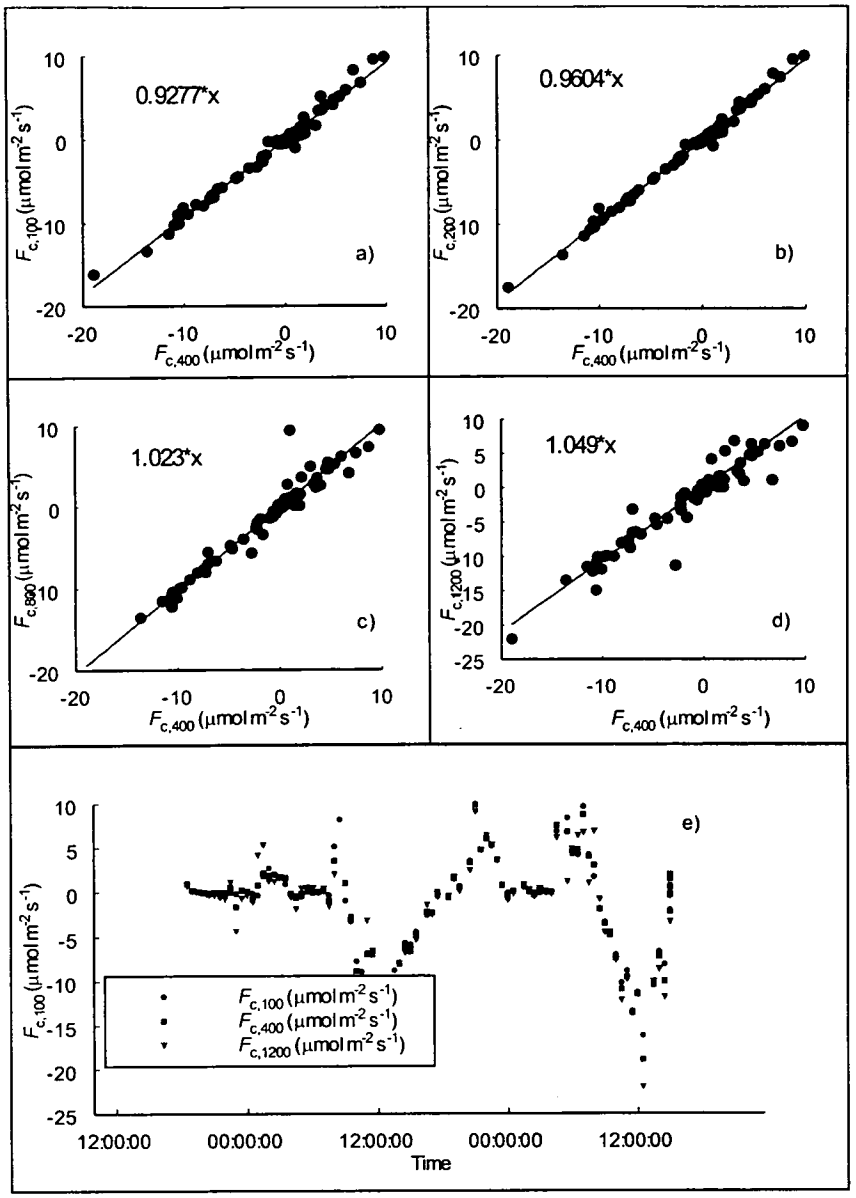

Figure 4-12 Plots a) to d) are scatter plots of F_c calculated using different time constants for the ARMA: a) 100 s [$F_{c,100}$], b) 200 s [$F_{c,200}$], c) 400 s [$F_{c,400}$], d) 800 s [$F_{c,800}$] and e) 1200 s [$F_{c,1200}$] plotted against F_c calculated using a digital running mean time constant of 400s for the 31 August and1 September 1996. e) Time series of $F_{c,100}$, $F_{c,400}$ and $F_{c,1200}$ for the 31 August and 1 September 1996.

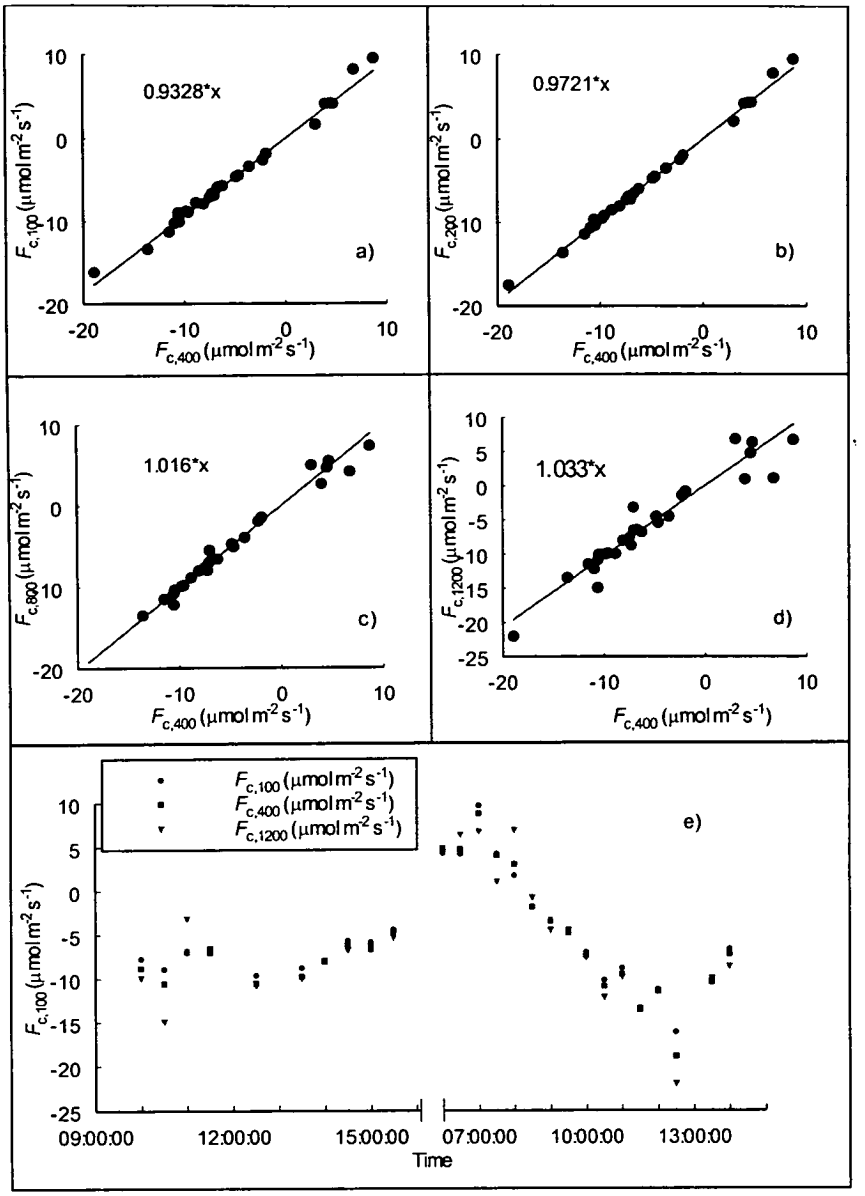

Figure 4-13 Plots a) to d) are scatter plots of F_c calculated using different time constants for the ARMA: a) 100 s [$F_{c,100}$], b) 200 s [$F_{c,200}$], c) 400 s [$F_{c,400}$], d) 800 s [$F_{c,800}$] and e) 1200 s [$F_{c,1200}$] plotted against F_c calculated using a digital running mean time constant of 400s for the 31 August and1 September 1996. e) Time series of $F_{c,100}$, $F_{c,400}$ and $F_{c,1200}$ for the 31 August and 1 September 1996. Instationary data *i.e.* when $I_c > 0.3$ was excluded.

4.9 Summary and conclusions

During March, April and November when vapour pressure and evaporation were close to zero, $H \approx H_s$. For the whole period of the study the average half-hour difference between H and H_s was 2 % H and went up to 10 % H (and higher when $|H| < 0$). The average half-hourly correction as a function of E was $2.7E$ (W m^{-2}) (see Figure 4-1).

The speed of sound calibration (and hence sonic temperature) was different for each Solent 1012R2 compared in this chapter when the temperature of the anemometer was less than 5 °C. The calibration below 5 °C is complicated by hysteresis caused by thermal inertia especially when the calibration is calculated from half-hour averages. This caused increased noise in the derived sonic temperature and hence sensible heat flux estimates when $-10 < T_a < 10$, however, the calibration ensures any bias is small when half-hour values of H are averaged.

The Kaimal cospectral models fitted well with cospectra calculated for SSA OBS and frequency functions accounted for high frequency attenuation by the system. During the night when wind speeds were low (poor mixing) frequency corrections did not work well, at least in part, because the spectra and cospectra were poorly defined.

The mean second rotation angle (around the y axis) for 4 ° bins was between -1 ° and 4 ° and did not increase in variability with wind direction. This indicates there was no increase in flow distortion at any wind direction. The results for the second rotation angle are similar to those reported for the Harvard Forest flux measurements (Goulden *et al.*, 1996) where the mean second rotation angle for 4 ° wind direction bins was between -2 ° and 3 °. The mean third rotation angle for 4 ° wind direction bins was between -5 ° and 5 ° and the standard deviation for the same wind direction bins was 7 °. The third rotation angle is generally more variable than the second and is not well defined at low windspeed and should be limited to 10 ° (McMillen, 1988). The third rotation angle was larger than 10 ° for less than 1 % of the half-hour averages.

Similarity relationships between normalised standard deviations of w, CO_2 and water vapour concentration (σ_w/u_*, σ_c/c_* and σ_q/q_*) with ζ were close to ideal values except when $u_* < 0.2$ m s^{-1} and when the F_c and E were close to zero. Monin-Obukov similarity theory is not valid when u_* is close to zero (Stull, 1988). It is also not valid when fluxes are close to zero when there is no relationship between u_* and the corresponding covariance used to calculate the scaling factor.

Extended periods of stationarity only occur when there is continuous turbulent mixing (quantified by u_*). During the period of the stationarity tests, daytime measurements were stationary from after turbulence had built up in the morning until sunset or a rain event. During calm night measurements, there were sporadic instationary half-hours.

During stationary conditions, the value of the ARMA time constant made little difference to the estimate of F_c. However, F_c calculated using 100 s and 200 s as the value for the time constant, were smaller than F_c calculated using the longer time constants. This indicates that the frequency corrections for loss of low frequency, caused by the ARMA, were not fully compensated for. F_c calculated with a time constant of 400 s was 1 % of F_c calculated using a time constant of 800 s or 1200 s. When data from instationary conditions were included the difference in estimates of F_c with different time constants diverged more. The choice of 400 s as the time constant for the study appears to have been a good compromise. Results in stationary conditions were very close to those when longer time constants were used while avoiding some of the overestimation of variances and covariances caused by using longer time constants (Shuttleworth, 1988).

Chapter 5 Carbon and water vapour exchange

5.1 Introduction

The net carbon exchange of a forest depends on the assimilation of CO_2 by photosynthesis and on CO_2 emissions resulting from respiratory processes. CO_2 assimilation depends on the species, age and physiological activity of the trees. Emission depends on the respiratory cost of maintenance and growth of vegetation and soil microbes involved in decay. Influencing both these processes are soil, climate and weather. During the day in the growing season, photosynthesis will usually dominate respiration and CO_2 will be taken up by the stand. At night, there is no photosynthesis and CO_2 produced by respiration is lost from the stand. During the winter photosynthesis ceases or becomes negligible and the stand loses CO_2 by respiration as at night. Though the rate of respiration will be slow, because of low temperatures, boreal winters are long and the accumulated loss of carbon may be high.

The water vapour lost from a stand depends on energy to drive evaporation and the vapour pressure deficit (VPD). During the day, in the growing season, there is enough solar radiation to drive evaporation and air temperatures are generally high enough that the air is not saturated, therefore, water vapour is lost from the stand. In contrast, at night there is no solar radiation to supply the energy for evaporation and air temperature often falls below the dew point. Therefore, at night the water vapour flux from the stand is approximately zero. During the winter, solar radiation and temperatures are also low in much of the boreal forest, including SSA OBS, where temperatures are well below zero and there is negligible evaporation.

A simplified conservation of mass equation for CO_2 gives:

$$F_c = F_a + F_s + F_g + \Delta S_c \qquad (5\text{-}1)$$

where F_c is the net flux of CO_2 into or out of the stand from the air above, F_a is the canopy assimilation (or respiration at night), F_s is stem respiration, F_g the soil CO_2 efflux (which is the sum of root and soil microbial respiration) and ΔS_c is the change

in storage of carbon dioxide in or out the air of the stand. F_c is measured with the eddy covariance system (the eddy flux) assuming no vertical advection other than that caused by density fluctuations (Webb, Pearman and Leuning, 1980). The ΔS_c is estimated from change in the CO_2 concentration profile over a period and is converted to flux units and loosely termed the "storage flux". The sign convention followed here is that positive fluxes are to the atmosphere and negative fluxes are to the surface. Fluxes into storage in the air below the eddy covariance sensors are positive.

The storage flux, S_c, is calculated as the change in CO_2 concentration in a column of air of unit area below the eddy covariance sensors.

$$S_c = \sum_{n=1}^{8}\left[(h_n - h_{n-1})\left(\frac{\chi_{C,n} + \chi_{C,n-1}}{2}\right)\left(\frac{1000}{V_{Mair}}\right)\right] \quad (5\text{-}3)$$

$$\Delta S_c = S_{ci} - S_{ci-1}$$

where $n = 1 \ldots 8$ are the sample height numbers, h is the sample height in metres, χ_C is the molar ratio of CO_2 in μmol mol^{-1} and V_{Mair} is the molar volume of air, 22.4 dm^3 mol^{-1} at STP. It was assumed that the concentration measured at the lowest sampling point was representative of the concentration between that height and the ground surface. The storage flux for water vapour is calculated similarly by:

$$S_h = \sum_{n=1}^{8}\left[(h_n - h_{n-1})\left(\frac{\chi_{v,n} + \chi_{v,n-1}}{2}\right)\left(\frac{1}{V_{Mair}}\right)\right] \quad (5\text{-}4)$$

where χ_v is the molar ratio of H_2O in mmol mol^{-1} and V_{Mair} is the molar volume of air, 22.4 dm^3 mol^{-1} at STP.

The biotic flux is the diffusive flux at the vegetation/air and soil/air interface (not including air in soil pores) is given by:

$$F_b = F_c - \Delta S_c = F_a + F_s + F_g \quad (5\text{-}5)$$

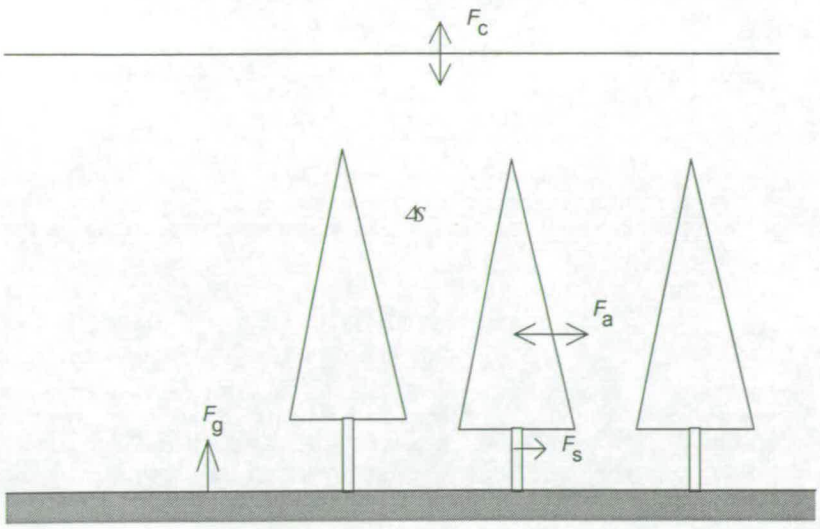

Figure 5-1 Major fluxes of CO_2 in a stand. The direction of the arrows shows the direction of the flux and the line at the top is the plane at the top of the stand as defined by the placement of the eddy covariance sensors. See text for the definition of the symbols.

This chapter addresses questions about the exchange of CO_2 and water vapour at the BOREAS Southern Study Area Old Black Spruce site (SSA OBS) as described in chapter 2. The specific questions addressed are enumerated below.

- Is SSA OBS a sink or source of CO_2?
- What is the sink/source strength for CO_2?
- How does CO_2 exchange respond to PPFD, temperature and VPD?
- How much water is lost by the stand by evapo-transpiration?
- What is the day versus night variation in CO_2 flux and evaporation?

5.2 Concentration Profiles and Storage Flux

Figure 5-2 shows monthly average diurnal curves of CO_2 concentration at each of the heights, 0.5, 1.5, 3.5, 6.5, 9.5, 12.5 18 and 26 m and Figure 5-3 shows the same data but plotted as profiles. The graphs show a seasonal trend in CO_2 concentration when the minimum hourly mean at 26 m decreased from 376 μmol mol^{-1} in March to 350 μmol mol^{-1} in July and then increased to 370 μmol mol^{-1} in November. The diurnal variation of hourly mean CO_2 concentration at 26 m was also seasonal: being smallest in March and November, ± 1 μmol mol^{-1}, and largest in July when it varied

from 350 μmol mol^{-1} at 19:00 GMT to 373 μmol mol^{-1} at 10:00 GMT. Concentrations below 26 m varied little from that at 26 m during the cold months but the variation increased during the summer when CO_2 concentration increased at night especially at the lower levels. The extreme variation was at 0.5 m in July when the variation was from 351 μmol mol^{-1} at 19:00 GMT to 501 μmol mol^{-1} at 12:00 GMT.

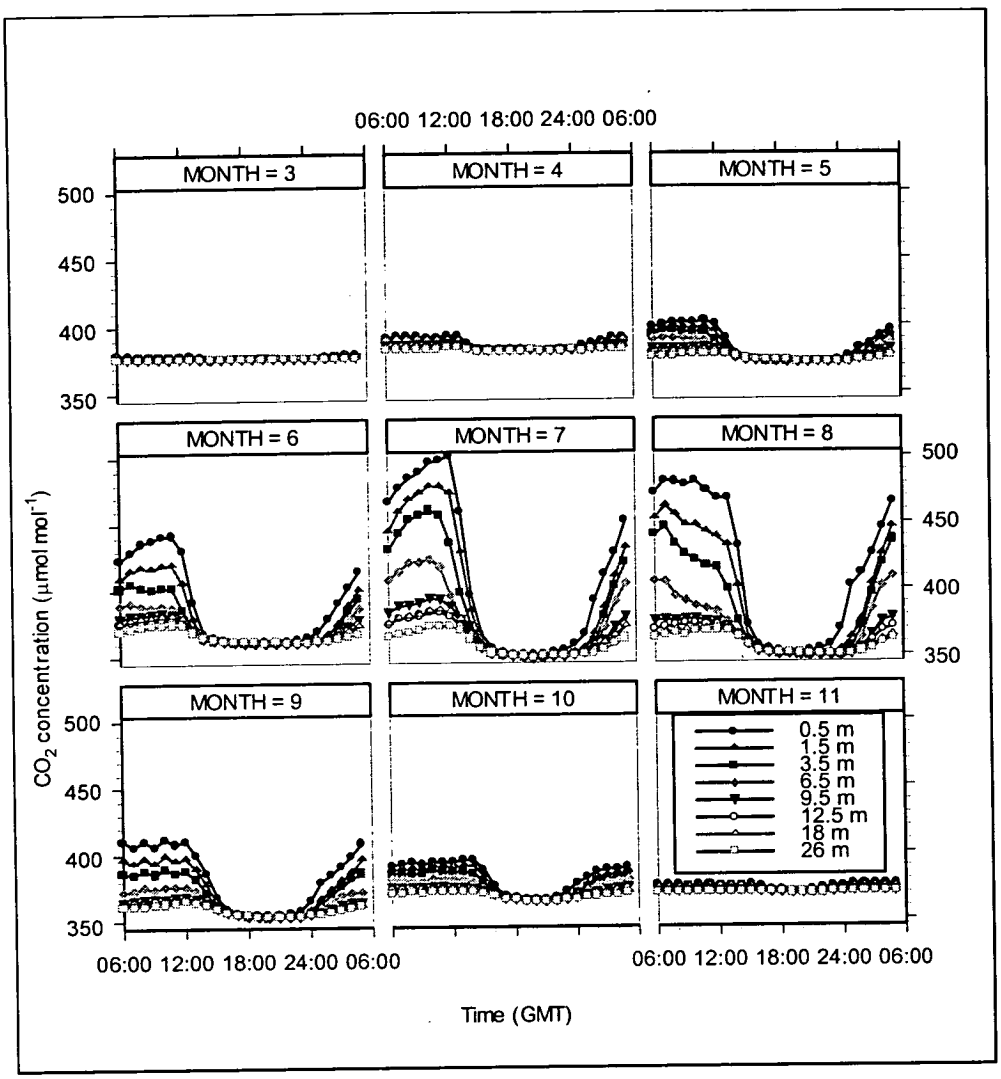

Figure 5-2 Monthly mean diurnal courses of CO_2 concentration. Each point is the mean value for the hour before the time shown for each day of the month on which data was collected. This data is also shown in Figure 5-2 as profiles.

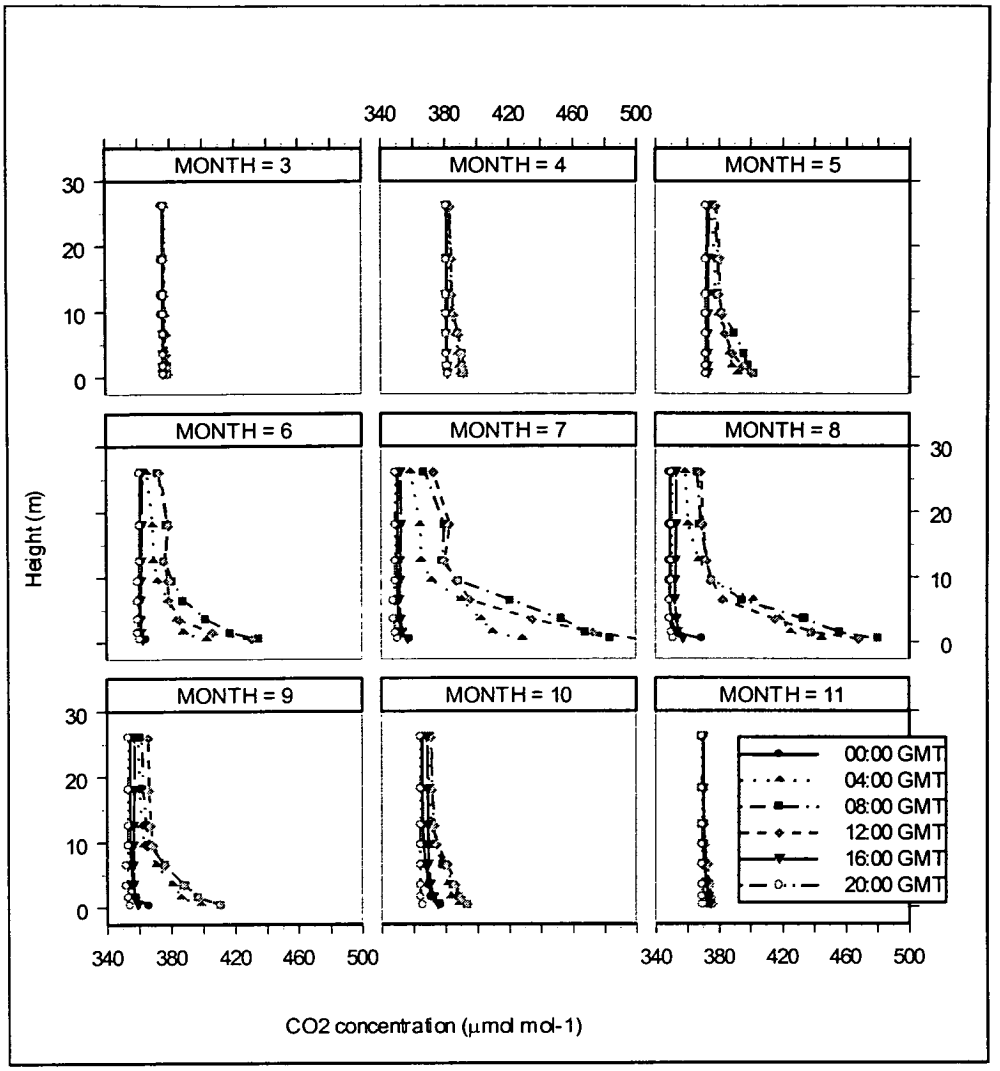

Figure 5-3 Monthly mean CO_2 concentration profiles. Each point is the mean value for the hour before the time given for each day of the month on which data was collected. This data is also shown in Figure 5-1 as monthly mean diurnal time series.

Minimum monthly mean hourly water vapour concentration varied from *ca* 2 mmol mol^{-1} (≈0.2 kPa) in March and November to 10 mmol mol^{-1} (≈1.0 kPa) in August, Figures 5-4 and 5-5. During the colder months variation at all heights was very small (< 2 mmol mol^{-1} in November) but increased to a maximum in July. The most extreme variation was at 0.5 m in July when the variation was from 10 mmol mol^{-1} at 12:00 to 15 mmol mol^{-1} at 19:00 GMT. The largest variation w.r.t. height of over 2 mmol mol^{-1} was also in July.

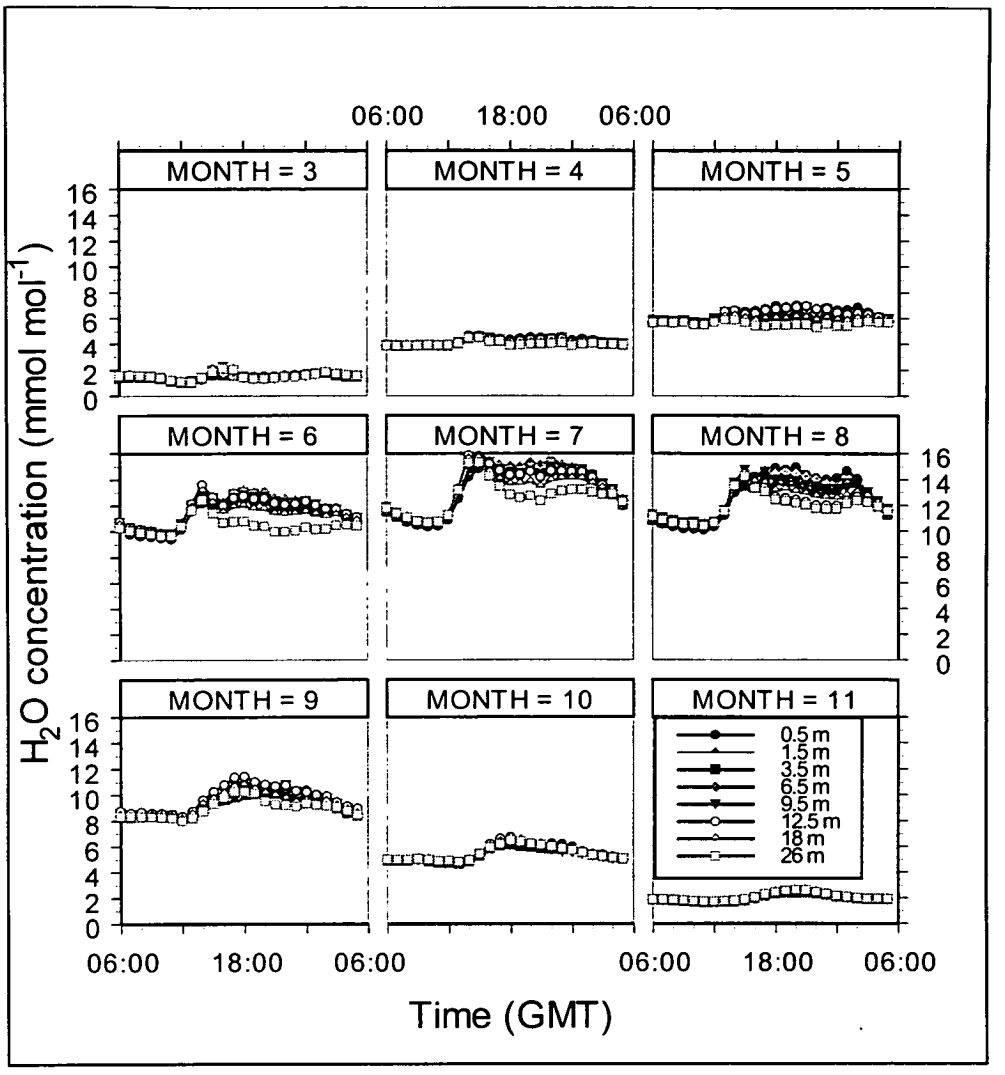

Figure 5-4 Monthly mean diurnal curves of H_2O concentration. Each point is the mean value for the hour before the time shown for each day of the month on which data was collected. This data is also shown in Figure 5-5 as profiles.

Unlike the CO_2 concentrations the water vapour concentrations varied with height during the day. There is no sink in the canopy for the water vapour evaporated during the day, whereas the photosynthesising foliage is a sink for the respired CO_2 and may, together with mixing, prevent CO_2 concentrations varying with height.

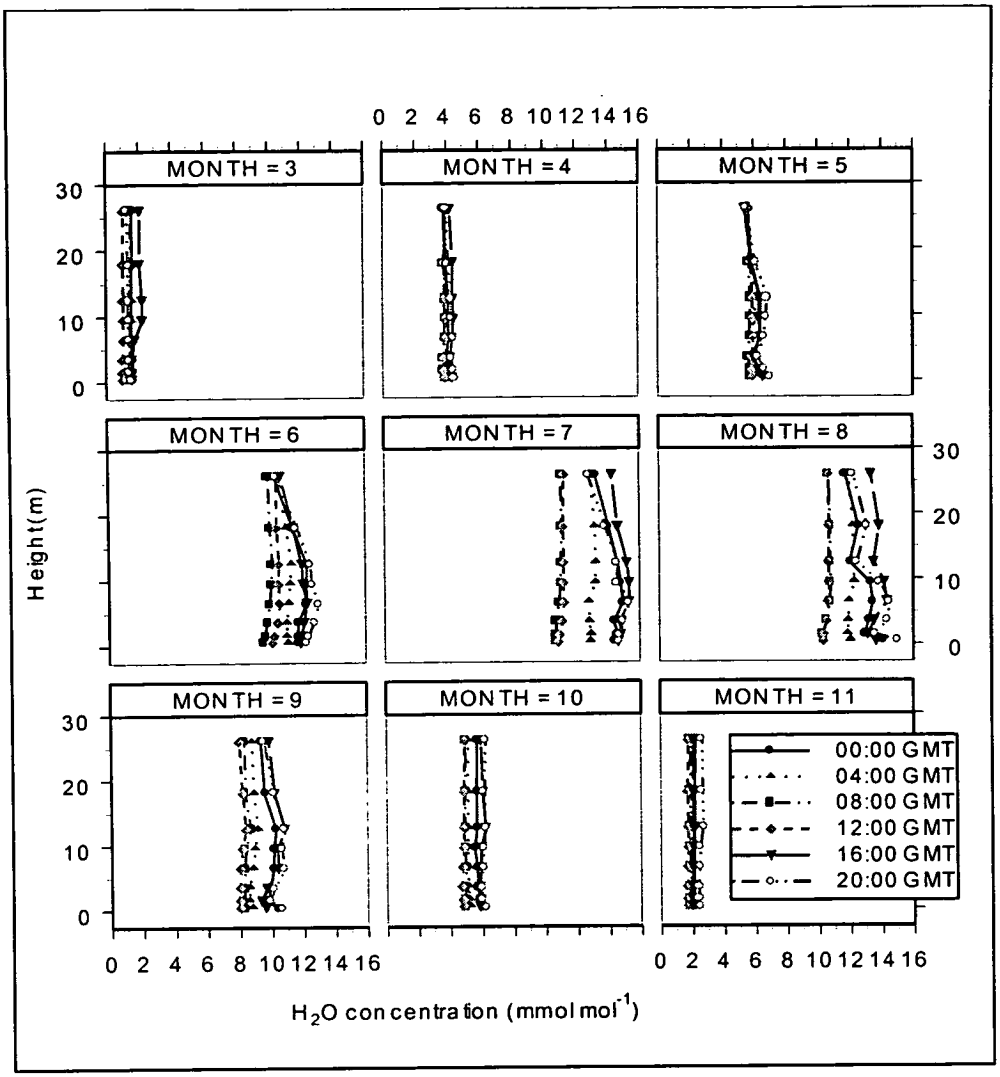

Figure 5-5 Monthly mean H_2O concentration profiles. Each point is the mean value for the hour before the time given for each day of the month on which data was collected. This data is also shown in Figure 5-4 as monthly mean diurnal time series.

5.3 Biotic CO_2 flux and total evapo-transpiration

The eddy and storage fluxes were summed to estimate the biotic CO_2 flux and the diurnal courses of these fluxes are shown in Figure 5-6. The magnitudes of the fluxes changed seasonally but the shapes of the diurnal curves were similar but because of the scale, details of the diurnal curves for March, April and November are not evident. Shortly after dawn but before turbulence had fully developed there was a loss of CO_2 from storage in the air that was not seen leaving the stand in the eddy flux. This indicates that some of the CO_2 respired overnight was reassimilated by

photosynthesis in the morning. Another period when there was a significant storage flux was after sunset, turbulence lessened as convection reduced and there was a gain of CO_2 stored in the air. The storage continued until dawn but at a decreasing rate. If a constant flux layer is assumed, i.e. that the eddy flux was equal to the surface flux (the flux from the vegetation and soil), there would be a significant underestimation of the biotic flux during the early morning and night.

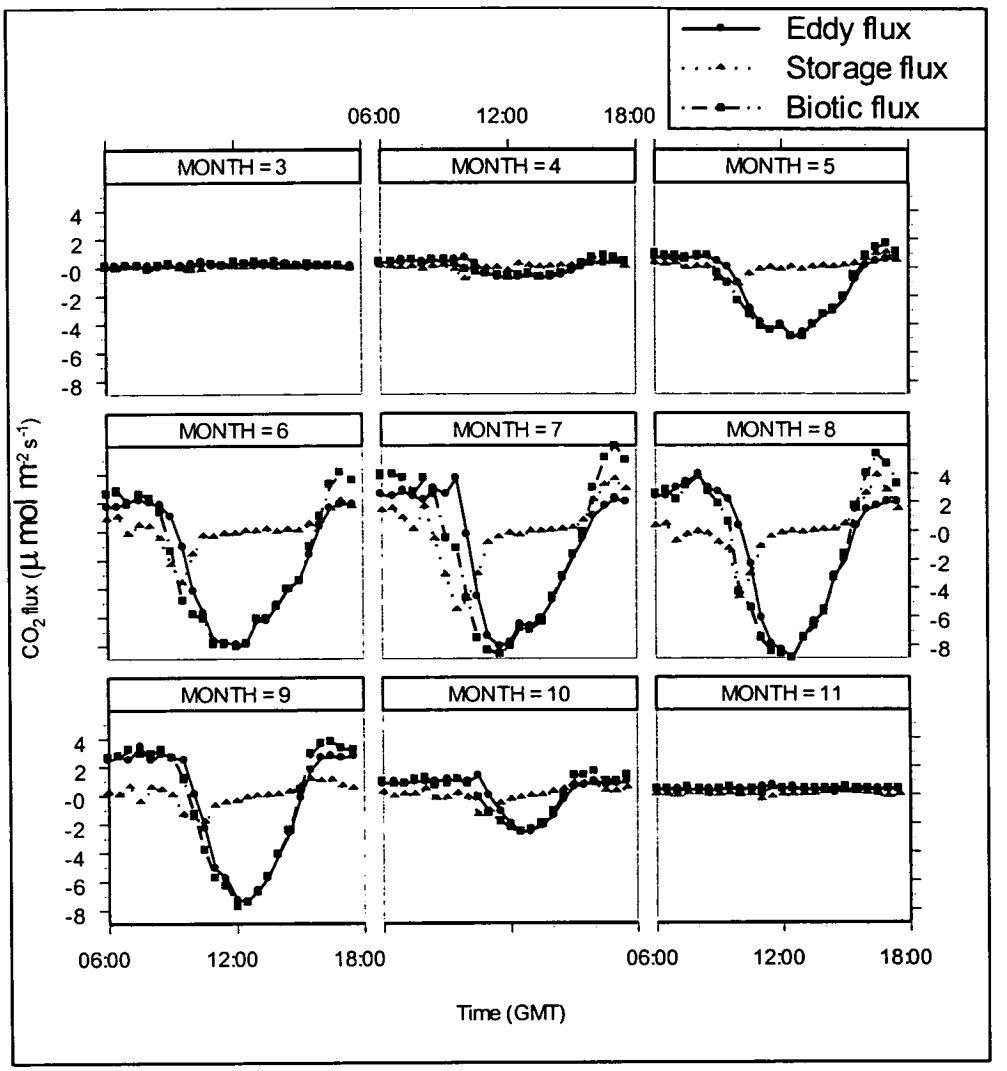

Figure 5-6 Mean diurnal time course of CO_2 fluxes: eddy flux, storage flux plus eddy flux (estimate of biotic flux). Each point is the average flux for the hour before the time shown for each day of the month. No correction has been made for night time underestimation of flux.

The balance between storage and eddy fluxes depends on turbulence. If the air flow is very turbulent the air is well mixed and changes in storage are small. On the other

hand, if turbulence is low the eddy flux (turbulent transport) is small and sinks or sources of CO_2 change the CO_2 concentration in the air and hence the storage flux.

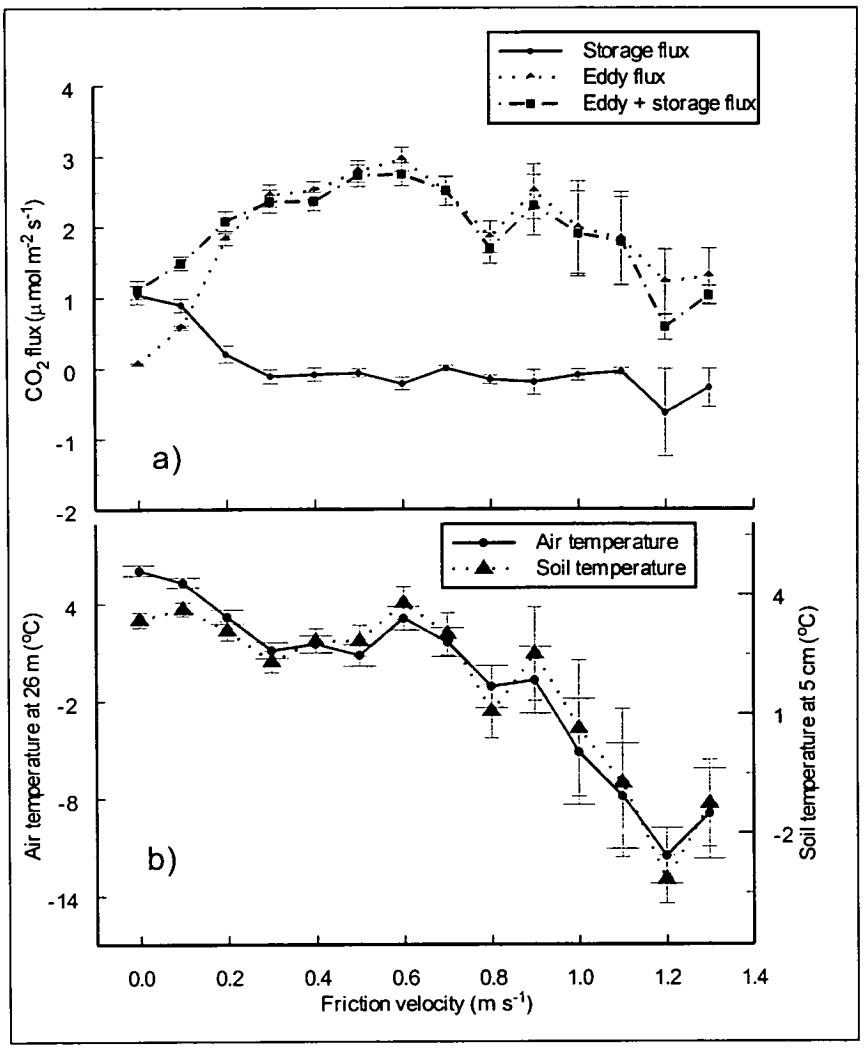

Figure 5-7 a) Eddy + storage flux, eddy flux and storage flux versus friction velocity and b) air temperature at 26 m and soil temperature at 5 cm versus friction velocity at night. Each point is the average value for a 0.1 m s^{-1} interval of friction velocity centred at the friction velocity shown for all half-hourly values from 25 March (day 85) until 28 November (day 333) 1996. Error bars are ± one standard error.

During the day, the storage flux is small because the convection caused by solar heating produces turbulence and there are both sources and sinks for CO_2 below the eddy covariance sensors. To examine the balance of eddy flux to storage flux at night, Figure 5-7a shows eddy + storage, eddy and storage fluxes versus friction velocity, used here as a measure of turbulence. It can be seen that at low values of

friction velocity the eddy flux was close to zero and that almost all the CO_2 flux was accounted for by the storage flux whereas, at high friction velocities the storage flux is very small.

Total evapo-transpiration is analogous to the biotic flux of CO_2. Using the same simplified conservation of mass equation as for CO_2, total evapo-transpiration is estimated by the sum of eddy flux and storage flux. Figure 5-8 shows the diurnal course of water vapour fluxes for each month in which measurements were made. The storage flux was largest during the day with a maximum at 20:00 GMT (one hour after solar noon) and smallest at night. During March, April and November the mean hourly water vapour storage flux was always negative as the air became drier. Mean hourly water vapour storage flux was always negative for at least a portion of the night, just before dawn when the saturation vapour pressure was lowest. During the day in May, June, July and August the water vapour storage flux was positive for some of the day.

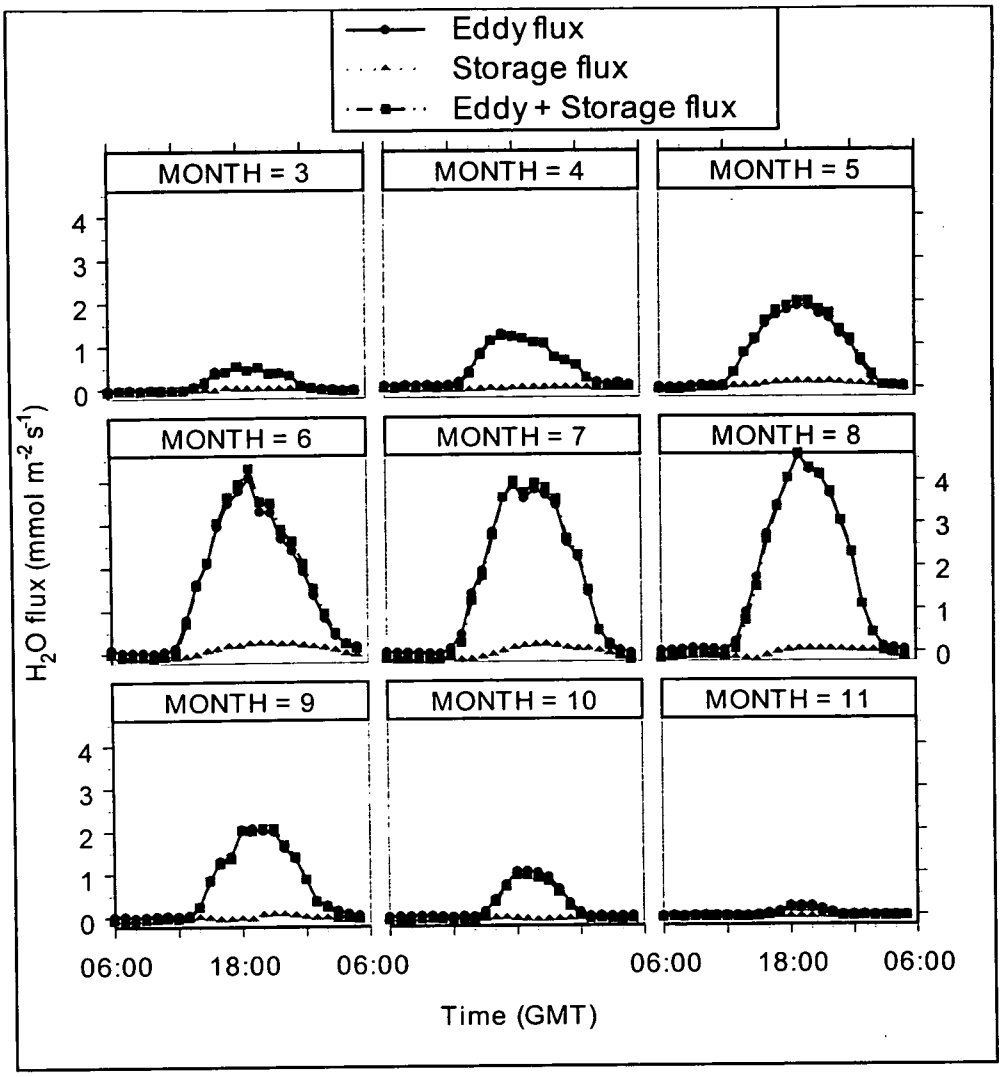

Figure 5-8 Monthly mean diurnal time course of H_2O fluxes: eddy flux, storage flux and eddy flux (estimate of total evapo-transpiration). Each point is the average flux for the hour before the time shown for each day of the month.

5.4 Underestimation of biotic CO_2 flux at night

As shown in Figure 5-6 the CO_2 storage fluxes are important at night, dawn and dusk and Figure 5-7a shows the variation in contribution of the storage and eddy CO_2 fluxes to the biotic CO_2 flux in relation to friction velocity where the fluxes have been averaged over friction velocity interval of 0.1 m s^{-1}. When the friction velocity was close to zero the eddy flux was also close to zero and the storage flux made up all the measured biotic flux. As the friction velocity increased to 0.3 m s^{-1} the eddy flux increased and the storage flux decreased to zero. At friction velocities over 0.3

m s^{-1} the storage flux average was close to zero and almost all the measured biotic flux was made up by eddy flux. The decrease in measured biotic CO_2 flux at high friction velocities can be explained by a decrease in average temperature at which those fluxes were measured, see Figure 5-7b which shows the average air temperature at 26 m and soil temperatures at 5 cm averaged over the same friction velocity intervals as for Figure 5-7a. However, the low measured biotic flux at low friction velocities cannot be explained in the same way because mean temperatures increase at friction velocities below 0.3 m s^{-1}, i.e. the mean measured biotic efflux is negatively correlated with the mean temperatures for the same friction velocity interval. Thus, there is biotic efflux that is apparently not being measured below a friction velocity of about *ca* 0.4 m s^{-1} though the threshold is difficult to determine accurately. Similar underestimation of biotic flux has been found at other sites, e.g. Harvard Forest (Goulden *et al.*,1996) and BOREAS SSA Old Aspen (Black *et al.*, 1996).

This underestimation of night fluxes may be because storage in the soil is assumed to be nil or because of fluxes ignored in the simplified mass balance we are using, ie horizontal flux divergence or vertical advection (non zero mean vertical windspeed).

5.5 Dark respiration

During the night, the biotic CO_2 flux is caused only by respiration because there is no light to drive photosynthesis. If the measurements when the friction velocity was less than 0.4 m s^{-1} are excluded to prevent underestimation of the biotic flux the relationship between dark respiration of the stand, R_d, and temperature can be investigated.

To investigate the seasonality in respiration the data were grouped by month and the R_d regressed against air temperature at 24 m, T_a, and soil temperature at 5 cm depth, T_{s5cm},

$$R_d = R_{0,s} \exp(k_s T_{s5cm}) \qquad (5\text{-}6)$$

$$R_d = R_{0,a} \exp(k_a T_a) \qquad (5\text{-}7)$$

Where $R_{0,s}$ and $R_{0,a}$ the respiration rates at 0 °C w.r.t. T_a and T_{s5cm}, respectively, and k_s and k_a are parameters describing the response to T_a and T_{s5cm}.

The above ground respiration is likely to be driven by air temperature. Similarly, soil plus root respiration is likely to be driven by soil temperature. The combined response of R_d to T_a and T_{s5cm}, equation (5-8), was fitted by non-linear least-squares regression (Proc NLIN, SAS, SAS Institute Inc, Cary, NC, USA).

$$R_d = R_{0s} \exp(k_{Ts} T_{s5cm}) + R_{0a} \exp(k_{Ta} T_a) \qquad (5\text{-}8)$$

The temperature response equation used here is based on the Arrhenius equation. The temperature response is often reported as the increase in respiration with a 10 °C increase in temperature, Q_{10}, this is related to k_x by $Q_{10,x} = \exp(10k_x)$ where the subscript x denotes the medium of which the temperature is used in the relationship. The typical value of Q_{10} is about 2. Lavigne and Ryan (1997) measured black spruce stem respiration at SSA OBS in 1994 and found that Q_{10} varied from 1.8 early in the physiologically active season to 1.7 in the middle and end of the season and rose to 2.2 after the physiologically active season. Goulden and Crill (1997) found the Q_{10} of CO_2 efflux from moss surface (including soil CO_2 efflux) to be 2.29 over feather moss and 2.08 over sphagnum moss. Ryan *et al.* (1997) found the Q_{10} of black spruce foliage at NSA OBS to be 2.1, of conifer stems to be 1.7 and of conifer roots to be 1.9 during the growing season. The Q_{10} estimates above were all made using gas exchange chambers. Over a year at a temperate forest (Harvard forest) Goulden *et al.* (1996) estimated the Q_{10} for the respiration for the stand to be 2.1 and Black *et al.* (1996) estimated the Q_{10} of the SSA Old Aspen (AO) site over a year to be 5.37. Both Goulden and Black used nocturnal eddy covariance data.

Tables 5-1 and 5-2 shows the results of the regressions of the response of R_d to T_a and T_{s5cm}, respectively. Data were collected for only six days in March and during the summer months the nights were short and after removing data when $u_* < 0.4$ m s^{-1} the number of data points left were too few to show a strong relationship because of the noise in eddy covariance and storage flux measurements at night. The regression equation explained less than 50% for March, May, June, July, September and November. Moreover, the regression accounted for less than 20% of the

variation for March, May and July. The response of R_d to T_a was statistically significant ($Q_{10} > 0$ with $p < 0.05$) but shows no statistically significant change in Q_{10} by month.

Month	N	R_0	Q_{10}	R^2
3	15	0.12 (2.73)	0.62 (0.19)	0.02
4	103	0.88 (0.12)	3.77 (1.27)	0.52
5	44	1.23 (0.11)	1.60 (1.35)	0.18
6	79	1.90 (0.18)	1.75 (1.16)	0.42
7	38	2.39 (0.55)	1.99 (1.49)	0.20
8	81	3.43 (0.43)	1.48 (1.36)	0.07
9	183	2.41 (0.08)	1.76 (1.09)	0.49
10	142	1.48 (0.07)	1.70 (1.09)	0.52
11	177	0.92 (0.17)	1.71 (1.13)	0.29

Table 5-1 Regression parameters for equation (5-7) where N is the number of data points, R_0, the respiration rate at 0 °C w.r.t. T_a, Q_{10} is the increase in respiration rate for a 10 °C increase in temperature.

A seasonal change in the response of R_d to T_{s5cm} is suggested but the only significantly different Q_{10} values ($p < 0.05$) are those for March and November compared with those for July, August and September. However, the regression was particularly weak for March, July and August with $R^2 < 0.10$.

Month	N	R_0	Q_{10}	R^2
3	15	0.02(∞)	0.00 (∞)	0.00
4	103	0.80 (0.10)	3640.95 (3.06)	0.67
5	44	1.05 (0.16)	13.52 (4.62)	0.21
6	79	1.25 (0.13)	4.03 (1.19)	0.77
7	38	3.64 (0.63)	1.55 (1.67)	0.07
8	81	3.28 (0.52)	1.62 (1.54)	0.06
9	183	1.90 (0.10)	2.60 (1.14)	0.54
10	142	1.29 (0.07)	4.71 (1.28)	0.53
11	177	1.18 (0.21)	6.75 (1.50)	0.32

Table 5-2 Regression parameters for equation (5-6) where N is the number of data points, R_0, the respiration rate at 0 °C w.r.t. T_s, Q_{10} is the increase in respiration rate for a 10 °C increase in temperature.

Table 5-3 shows the results of the regression using the combined temperature response, equation (5-8). The 95% confidence intervals for the parameters are large

and no seasonal trend is shown. The collinearity between T_a and T_{s5cm} used as independent variables introduces much uncertainty in the results of the regression.

Month	N	R_{0s}	R_{0a}	Q_{10a}	Q_{10s}
3	15	0.72 (88.13)	-2.25(230.17)	7.39 (10.06)	7.39 (∞)
4	103	-0.85 (4.42)	1.82 (4.48)	1.61 (3.28)	1.49 (6.44)
5	44	1.33 (0.67)	-0.14 (0.73)	7.39(110.82)	7.39 (3.90)
6	79	1.71 (2.89)	-0.52 (3.41)	1.75 (7.43)	3.75 (2.77)
7	38	-10.87(223.02)	12.54(210.55)	1.58 (91.99)	1.49(217.02)
8	81	1.53 (3.59)	0.24 (0.99)	7.39 (7.80)	1.49 (4.02)
9	183	NA(NA)	NA(NA)	NA(NA)	NA(NA)
10	142	0.32 (5.84)	1.30 (6.23)	1.78 (10.47)	3.16(6 x 10^6)
11	177	0.53 (0.74)	0.45 (0.62)	7.39 (18.22)	1.62 (6.98)

Table 5-3 Regression parameters for equation (5-8) where N is the number of data points. The regression procedure failed to converge on parameters for month 9.

For the purpose of estimating R_d the best regression was found to be by separating the data into two periods: 1) June, July, August and September and 2) March, April, May, October and November and using equation (5-6) the response of R_d to T_{s5cm} (Figure 5-9). The residuals between predicted and observed values using parameters based on these periods were smaller than those based on the monthly parameters. For period 1) $R_{0,s}$ = 1.83 ± 1.08 μmol m^{-2} s^{-1}, $Q_{10,s}$ = 2.65 ± 1.09 with N = 384, R^2 = 0.59 and root mean squared error (RMSE) = 1.30 μmol m^{-2} s^{-1} and for period 2) $R_{0,s}$ = 1.02 ± 1.07 μmol m^{-2} s^{-1}, $Q_{10,s}$ = 6.03 ± 1.22 with N = 485, R^2 = 0.41 and RMSE = 1.88 μmol m^{-2} s^{-1}. The error terms are 95% confidence intervals.

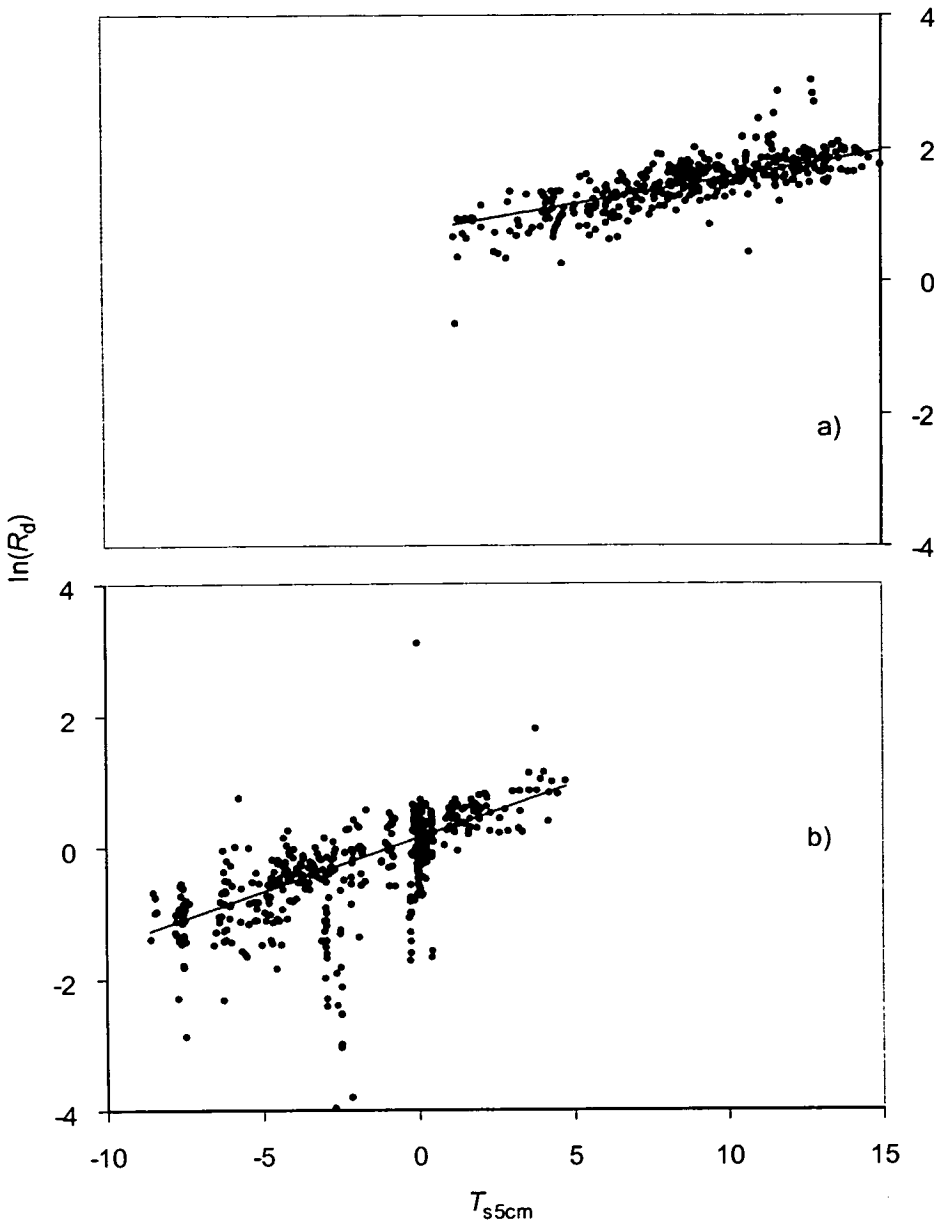

Figure 5-9 Relationship between ln(R_d) and T_{s5cm} a) shows the data from June, July, August and September and b) shows the data from March, April, May, October and November. Each point is a half-hour flux average for data when friction velocity > 0.4 m s^{-1} and Q < 1.0 μmol m^{-2} s^{-1}.

5.6 Response of assimilation rate to environmental variables

Gross photosynthetic rate (CO_2 assimilation rate) for each half-hour period was calculated as $A = -F_b + R_d$ when photosynthetic photon flux, $Q > 0$ μmol m^{-2} s^{-1}. (Positive assimilation is a flux of CO_2 into the plant from the atmosphere.) This assumes that respiration in the light is the same as that at night at the same temperature: R_d was defined in the previous section. Q saturation of assimilation rate was at about 1000 μmol m^{-2} s^{-1} (Figure 5-10) and assimilation rates were reduced when saturation vapour pressure deficit, $D > 1.0$ kPa (Figure 5-10). When the air temperature at 26 m was below -3 °C assimilation rate was zero and increased with temperature from -3 °C to 20 °C (Figure 5-10), however, because at temperatures over 20 °C $D > 1.0$ kPa, 20 °C cannot be inferred to be an optimum temperature. The low temperature limit to assimilation is more likely to be whether the soil temperature was less than the freezing point of water. When the soil is frozen water is unavailable to for uptake by roots. When soil temperature at 10 cm, $T_{s,5cm}$, < 0 °C assimilation rate was zero (Figure 5-10).

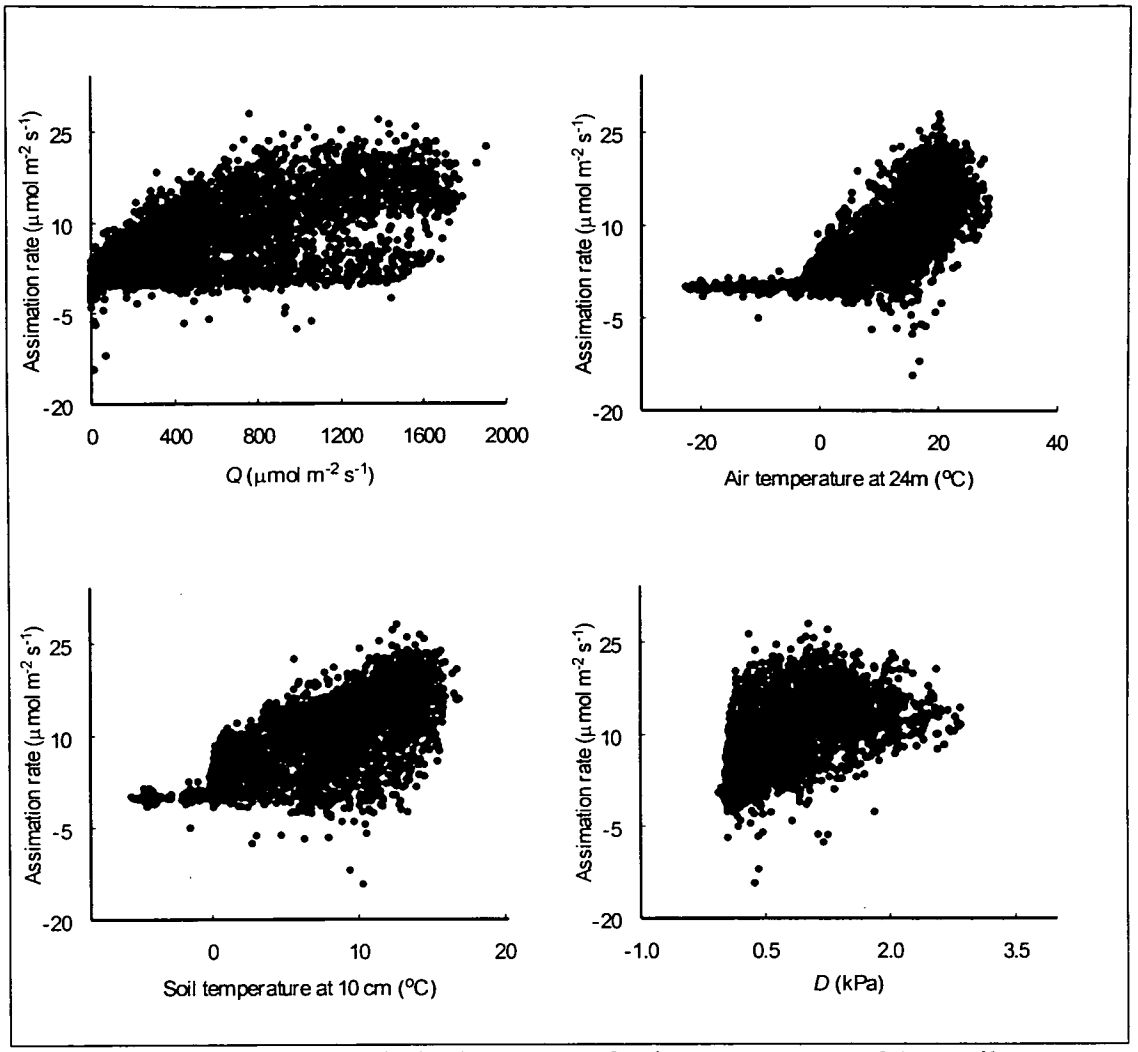

Figure 5-10 Response of assimilation rate to Q, air temperature at 24 m soil temperature at 10 cm and D at 24 m. Each point represents a half hour average when friction velocity > 0.4 m s^{-1} to exclude data from instationary periods (Chapter 4).

Figure 5-10 suggests that assimilation, A, may be modelled as a set of limiting functions of Q, air temperature (T_a) and D (Jones, 1992). The non-rectangular hyberbola equation was used to model the light response, A_Q:

$$A_Q = \frac{(\alpha Q + A_{max}) - \sqrt{(\alpha Q + A_{max})^2 - 4\theta\alpha Q A_{max}}}{2\theta} \qquad (5\text{-}8)$$

where, α is the quantum efficiency (i.e. the initial slope of the curve, moles of CO_2 assimilated per mole of quanta) (mol mol^{-1}), θ is the convexity of photosynthetic light response curve and fixed at the value of 0.8 which is a typical value for spruce (Leverenz and Jarvis, 1974) and A_{max} is the asymptotic maximum value for A_Q.

The beta function was used to model the normalised temperature response, A_T:

$$A_T = \frac{(T_a - T_L)(T_H - T_a)^P}{(T_o - T_L)(T_H - T_o)^P} \qquad (5\text{-}9)$$

$$\text{and } P = \frac{T_H - T_o}{T_o - T_L} \qquad (5\text{-}10)$$

where T_o is the optimum temperature at which A_T is 1.0, T_L is the lower temperature at which A_T is zero and T_H is the upper temperature at which A_T is also zero. A_T has a value between zero and 1.0 and is dimensionless.

The normalised D response, A_D, was modelled as unlimited when $D < D_L$ and when $D \geq D_L$, as a linear response with negative slope:

$$A_D = \begin{cases} 1.0 & \text{when } D < D_L \\ 1.0 - \dfrac{1.0}{(D_H - D_L)(D - D_L)} & \text{when } D_L \leq D \leq D_H \\ 0 & \text{when } D > D_H \end{cases} \qquad (5\text{-}11)$$

where D_L is the threshold below which D is not limiting (1.3 kPa) and D_H is the saturated vapour pressure deficit at which A_D becomes zero (5.0 kPa). A_D has a value between zero and 1.0 and is dimensionless.

The combined model is:

$$A = A_Q A_T A_D \qquad (5\text{-}12)$$

and was fitted by non-linear least-squares regression (Proc NLIN, SAS, SAS Institute Inc, Cary, NC, USA). The model was fitted month by month to allow for seasonal changes of the Q response. However, parameters for the temperature and D response fucntions could not be fitted month by month because monthly data corresponded to only part of the response curves. Hence, the values of D_L and D_H were fixed at 1.3 kPa and 5 kPa, respectively, by eye. When T_L, T_O and T_H were allowed to vary month by month T_L equalled –3 °C but T_O and T_H would exceed 50 °C and 70 °C, respectively. When the temperature response coefficients were restricted to values of

T_L, T_O and T_H of –3 °C, 30 °C and 50 °C, respectively, the model fitted the data well and also corresponded closely to values found from branch bag data (Rayment, 1998). The convexity of the Q response curve was restricted to a value of 0.8 and A_{max} to a value less than 50 μmol m^{-2} s^{-1} which was then returned as 50 μmol m^{-2} s^{-1} by the fitting procedure. The values for α returned by the non-linear regression procedure are shown in Table 5-4. In March and November when assimilation was negligible $\alpha < 0.01$ mol mol^{-1}. α increased from March (0.005 mol mol^{-1}) to July (0.066 mol mol^{-1}) and then decreased to 0.003 mol mol^{-1} in November. The summer values are close to the value that Goulden *et al.* (1997) reported for α of 0.05 mol mol^{-1} over the summer for black spruce at the BOREAS Northern Study Area Old Black Spruce site (NSA OBS) in northern Manitoba. Figure 5-11

Month	α (mol mol^{-1})
3	0.0005
4	0.011
5	0.022
6	0.051
7	0.066
8	0.064
9	0.034
10	0.032
11	0.003

Table 5-4 Values for the quantum flux efficiency (α) found by non-linear least squares fit of equation 5-12 which incorporates equation 5-8.

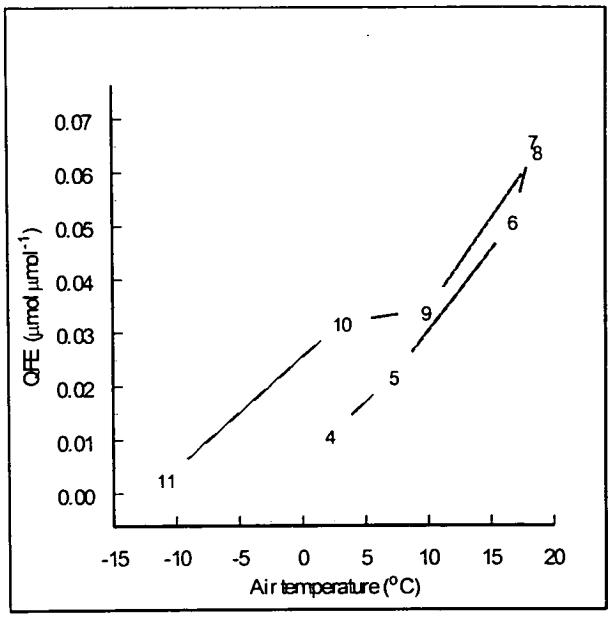

Figure 5-11 Values for the quantum efficiency, α, for each month found by non-linear least squares fit of equation 5-12 (which incorporates equation 5-8) plotted against mean monthly air temperature at 24 m. Each data point is indicated by the number of the month it represents.

5.7 Comparison of the biotic CO_2 flux model with the 1994 data

The models of dark respiration and of assimilation were summed to give a model of biotic CO_2 flux (after changing the sign of the assimilation to conform with the sign convention of the biotic CO_2 flux, positive is to the atmosphere). This model was then used with the parameters derived from the 1996 data and with the Q, D and air temperature data from 1994. This was then regressed against the measured 1994 biotic CO_2 flux (excluding night-time data when friction velocity was less than 0.4 m s^{-1}). The slope of the regression line was 1.09 and the R^2 was 0.65.

This suggests that a very simple statistical model can describe the biotic CO_2 flux at the SSA OBS well as at the BOREAS NSA OBS and Harvard forest (Goulden, 1997).

5.8 Daily biotic fluxes

Figure 5-12 shows the F_b summed over 24 hours with 24 hour sums of photosynthetic Q and mean 24 hour air temperature for the measurement period in 1996. F_b was positive, i.e. the stand was losing carbon and respiration was dominating over photosynthesis, at the beginning and end of the period. F_b was negative (i.e. the stand gained carbon) when soil temperature at 10 cm and 5 cm was above. 0 °C (Figure 5-10). The loss of carbon from the stand at the beginning of the period, just after the vernal equinox, occurred at a time when Q was about 30 mol m^{-2} day^{-1} with maximum half-hourly averages up to ~1500 μmol m^{-2} s^{-1} and there were approximately 12 hours of daylight. In contrast, after the autumnal equinox (day 266) there were several days of carbon gain (negative F_b). The switch between negative and positive F_b is determined by the soil temperature (Figure 5-10).

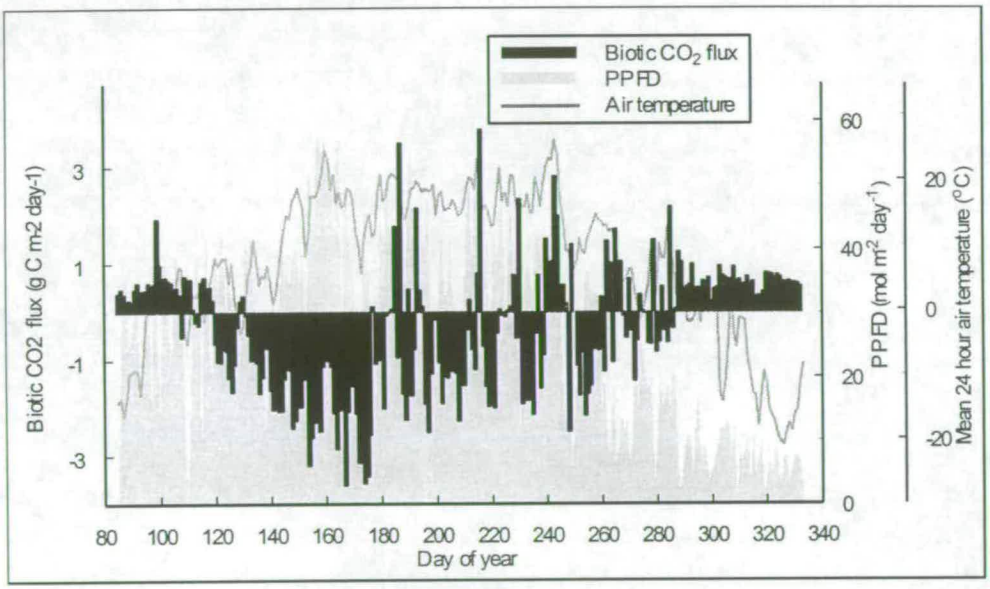

Figure 5-12 Daily totals of F_b corrected for night-time underestimation from March 25 (day 85) to November 28 (day 333) 1996 (positive is to the atmosphere), photosynthetic photon flux density (PPFD) and mean 24 hour air temperature at 26 m.

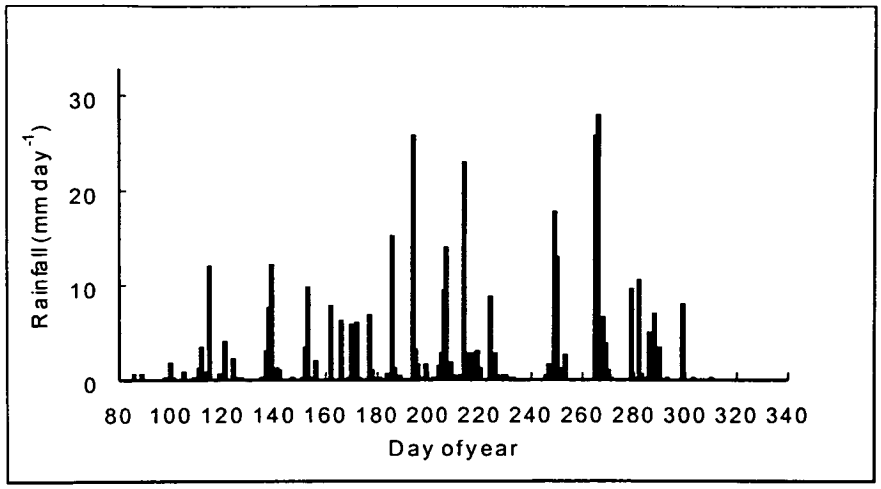

Figure 5-13 Daily totals of rainfall from March 25 (day 85) to November 28 (day 333) 1996.

The air temperature limitation was largest at the beginning and end of the measurements (and we assume, during the winter). The limitation decreased as the temperature increased during the spring until day 160 and then A_T varied usually between 0.6 and 1.0 (with a spike as low as 0.35) until day 245. After day 245 the temperature limitation increased until day 313 after which A_T remained 0 (Figure 5-14).

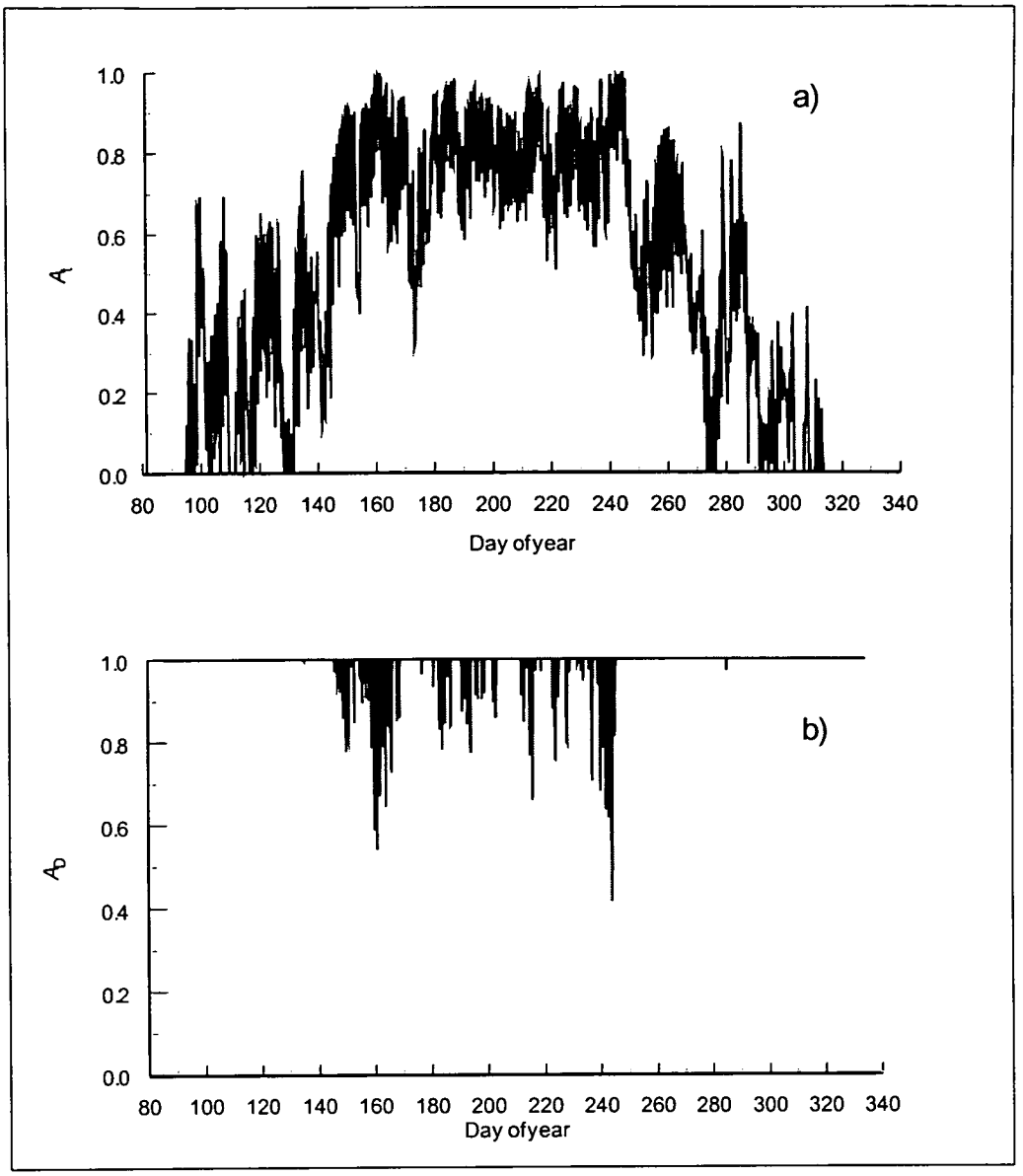

Figure 5-14 a) Normalised response of assimilation to air temperature at 24 m (Equation 5-9) and b) normalised response of assimilation to D (Equation 5-11) both fit by non-linear least squares regression.

Limitation of assimilation by VPD was confined to the summer period of day 143 to 244 when the limitation was highly variable. There were troughs in the value of A_D around day 160 and day 230. The minimum value of A_D was 0.4 but is value was generally much higher.

The evaporation rate (see Figure 5-15) was low at the beginning of the measurement period despite high net radiation but some mean 24 hour temperatures were still below freezing. At the end of the measurement period, the evaporation rate was

higher for the same net radiation than in the spring. This corresponds closely with the F_b largely because net radiation and Q were closely correlated (see Chapter 6). There were periods of high net radiation and high temperature around day 160 and 230 but then evaporation appears to have been limited by D which peaked at over 1 kPa. The peak in evaporation on day 162 occurred on a day when a total of 7.2 mm of rain (see Figure 5-15) fell in two separate events of less than 30 minutes each during the previous night. Net radiation was high during the day although there was some cloud in the afternoon and D at 24 m reached 2.0 kPa. Thus, the vegetation was wet with surface water from the rain events during the night, and the following by high net radiation and high D supplied the energy for evaporation and the atmosphere provided a strong sink for water vapour.

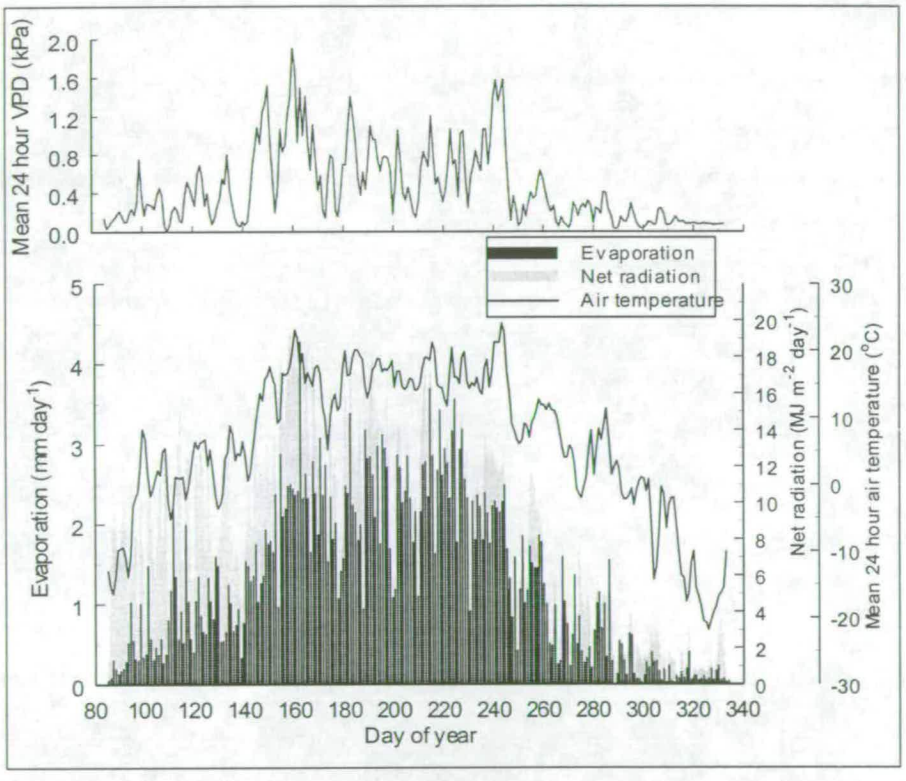

Figure 5-15 Daily totals of evaporation from March 25 (day 85) to November 28 (day 333) 1996 (positive is to the atmosphere), net radiation and mean 24 hour air temperature and D at 24 m.

5.9 Annual cumulative exchanges of carbon and water vapour

Any gaps in the F_b were filled using the regression model. No eddy covariance or profile measurements were made over the winter (December, January, February and 1 to 24 March), however, soil temperature measurements were made from 15 November 1995 until the end of the main 1996 measurement period on 28 November. By using the relationship between F_b and soil temperature, F_b over the winter may be estimated from the soil temperatures over this period. A relationship between respiration and soil temperature only was found by using half-hour night time data from March, April and November. The error terms are 95% confidence intervals (CI):

$$\ln R_d = (-0.1792 \pm 0.0971) + (0.1327 \pm 0.0242) T_{s5cm.} \quad (5\text{-}13)$$

This equation was used to estimated F_b from 29 November 1995 to 24 March 1996 using this relationship.

The cumulative exchange of carbon from 29 November 1995 until 28 November 1996 was calculated in four different ways, by summing:

1) the estimated winter biotic CO_2 flux and the measured biotic CO_2 flux with night-time correction,
2) the estimated winter biotic CO_2 flux using the lower 95% confidence interval of the coefficients and the measured biotic CO_2 flux with night correction, also using the lower 95% confidence interval of the coefficients,
3) the estimated winter biotic CO_2 flux using the upper 95% confidence interval of the coefficients and the measured biotic CO_2 flux with night-time correction, also using the upper 95% confidence interval of the coefficients,
4) the estimated winter biotic CO_2 flux and the measured biotic CO_2 flux with no night correction.

Method 1 assumes that the missing night time biotic CO_2 flux (section 5-5) is caused by an unmeasured flux, i.e. advected vertical flux caused by a mean vertical windspeed or by horizontal flux divergence. Methods 2 and 3 are the 95% confidence interval for the night time correction of method 1. Method 4 assumes that

there is no unmeasured true flux but that storage of CO_2 is underestimated because CO_2 storage in the soil is assumed to be nil. The results are shown in Figure 5-16.

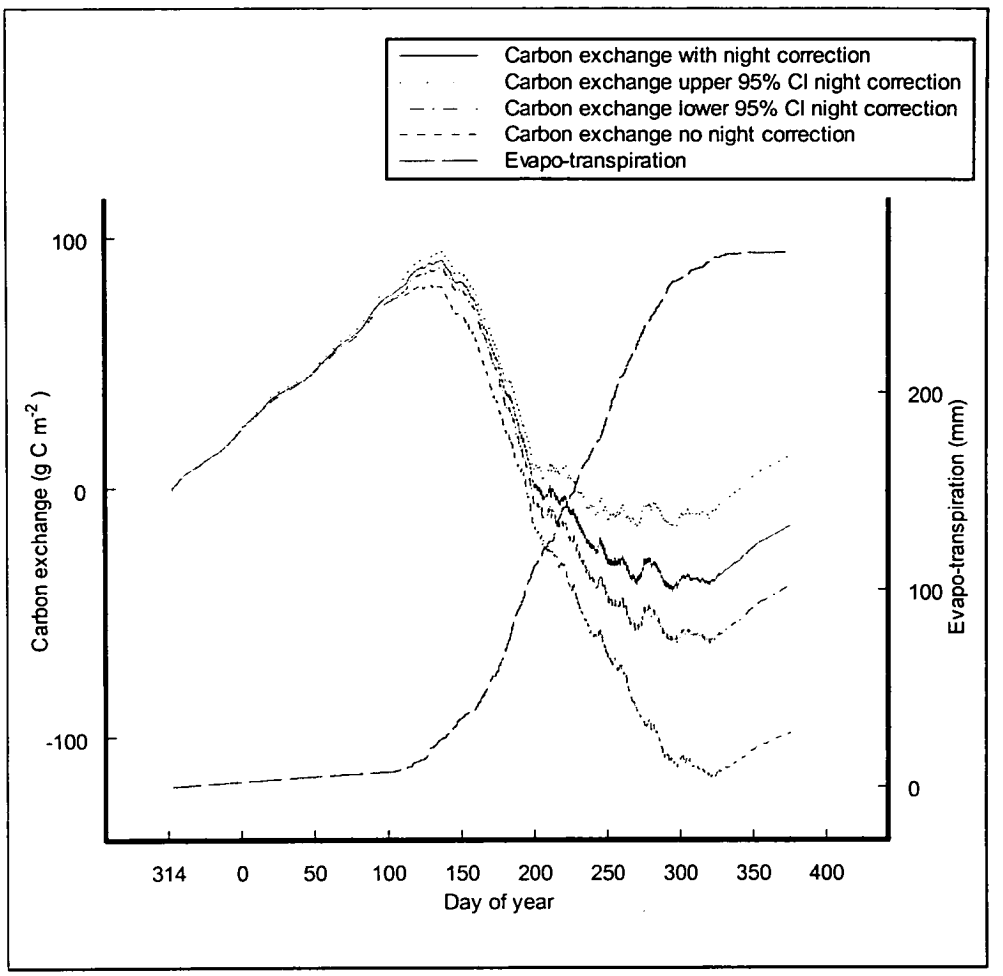

Figure 5-16 Cumulative exchange of carbon and evapo-transpiration from 29 November (day 333) 1995 to 28 November (day 334) 1996. Evapo-transpiration from 29 November 1995 to 25 March 1996 was assumed to be at the average rate for March and November 1996. Carbon exchange (net CO_2 fluxes) was not measured from 29 November 1995 to 25 March 1996 (winter) but was estimated from a regression equation for respiration against soil temperature at 5 cm depth. Carbon exchange was estimated in four ways: 1) using the estimated winter biotic CO_2 flux and the measured summer biotic CO_2 flux with night correction, 2) using the estimated winter biotic CO_2 flux and the measured summer biotic CO_2 flux with night correction using the upper 95% CI for the respiration regression coefficients, 3) using the estimated winter biotic CO_2 flux and the measured summer biotic CO_2 flux with night correction using the lower 95% CI for the respiration regression coefficients and 4) using the estimated winter biotic CO_2 flux and the measured summer biotic CO_2 flux with no night correction.

There is little difference between results of the methods during the winter. Method 1 and 4 share the same estimation equation, including coefficients, and the 95% CI as shown by the results of method 2 and 3 is small. The loss of carbon from day 333 in 1995 to day 70 in 1996 was 0.61 g C m^{-2} day^{-1} for all methods of estimation of F_b.

Method 4 (no night corrections) estimates the biggest uptake –97.63 g C m^{-2} $year^{-1}$. When the night-time correction is applied the uptake of carbon (CO_2) is reduced to -15.47 g C m^{-2} $year^{-1}$. The main difference between the results of 1 and 4 occurs from early June to September when the temperatures were high: the uptake rate (slope of the accumulation curve) for the night corrected curve, reduces overall, and includes short periods of carbon (CO_2) loss. At the end of September all four curves behave similarly and indicate carbon being lost at the same rate. The two extremes of the 95% CI for the night correction show a slow divergence through the winter and through spring. In early June, however, the divergence becomes much larger and the results of method 3 (upper 95% CI) estimates a loss of carbon through the summer at much the same rate as through winter and a final carbon exchange (a loss) of 12.62 gC m^{-2} $year^{-1}$. The results of method 2 (lower 95% CI) in contrast estimates uptake of carbon during the summer at almost the same rate as method 4 (no night-time correction) and a final carbon exchange of –39.41 g C m^{-2} $year^{-1}$.

The cumulative water vapour exchange (evaporation from the forest floor, transpiration and evaporation of water intercepted by the canopy) was calculated (with no night time corrections because evaporation is negligible at night [Figure 5-7]) and is shown in Figure 5-16. As with CO_2 fluxes, water vapour fluxes were not measured during the winter (December, January, February and 1 to 24 March). Evaporation of snow intercepted by the canopy is often a major loss of water during the winter (Golding, 1982). Evaporation was estimated for over the period is was not measured by taking the average evaporation rate measured in March and November 1996 which was 0.115 mm day^{-1}. The cumulative water vapour exchange curve is almost sigmoid. The slope is close to zero (0.115 mm day^{-1}) at the beginning and end of the flux measurements (and though the winter) and there was a steady loss of water at approximately 2 mm day^{-1} over the summer. The estimated loss over the

whole year was 271 mm. The total evaporation measured was 264 mm and over the same time the total rainfall was 378 mm.

5.10 Summary and conclusions

Night-time F_b was underestimated when friction velocity was less than about 0.4 m s^{-1}. There are several possible explanations for this at present unresolved: not measured CO_2 storage in the soil, horizontal advection, vertical advection (because mean vertical windspeed was not zero) and/or errors in the eddy covariance analysis.

Night biotic flux was "corrected" by substituting the measured values, when friction velocity was less than about 0.4 m s^{-1}, with an estimate using an exponential regression equation of respiration as a function of air temperature and soil temperature at 5 cm depth.

68 % of the variation in assimilation (estimated by adding the respiration estimated by the regression equation to the measured eddy flux) was explained by a regression model (equations 5-8 to 5-12) using Q, air temperature and D as the explanatory variables.

The combined regression equations for respiration and assimilation parameterised with 1996 data fit the 1994 data with a slope of 1.05 and R^2 of 65%.

The annual carbon exchange from 29 November 1995 to 28 November 1996 was –15.47 g C m^{-2} a confidence interval based on the 95 % confidence interval of the regression equation for respiration is –39.41 to 12.62 g C m^{-2}. The estimate for evapo-transpiration for the same period was 271 mm.

Chapter 6 Energy exchange

6.1 Introduction and theory

During the day the earth receives shortwave radiation from the sun and exchanges longwave radiation continuously with the atmosphere. This radiation balance can be written as:

$$R_n = S_{in} - S_{out} + L_{in} - L_{out} \qquad (6\text{-}1) \text{ or}$$

$$R_n = (1 - a)S_{in} + L_{in} - L_{out} \qquad (6\text{-}2)$$

where R_n is net radiation, S_{in} is shortwave radiation to the surface, L_{in} is longwave radiation to the surface, S_{out} is shortwave radiation from the surface and L_{out} is longwave radiation from the surface and a is the reflection coefficient of shortwave radiation (albedo) (Monteith and Unsworth, 1990). By convention, energy fluxes where direction is not specified are positive when the flux is to the surface and negative when the flux is from the surface. Net shortwave radiation, S_n, can be defined as S_{in} - S_{out} and net longwave radiation, L_n, as L_{in} - L_{out}.

The heat input to a system must be balanced by the heat loss and any heat stored in the system. This energy balance may be written:

$$R_n = H + \lambda E + G + B + S + A \qquad (6\text{-}3)$$

where R_n is net radiation, H is sensible heat flux, λE is latent heat flux (λ is the latent heat of vaporisation of water and E is the rate of evaporation), G is soil heat flux, B is biochemical energy stored by photosynthesis, S is heat storage within the stand and A is the energy removed by horizontal advection (Thom, 1975). Assuming a flat, horizontally homogenous and infinite fetch A is zero (Businger, 1986; Baldocchi et al., 1988; Moncrieff *et al.*, 1996). Figure 6-1 shows a diagrammatic representation of the energy balance components. The methods used to measure net radiation, sensible and latent heat flux and soil heat flux are described in Chapter 2.

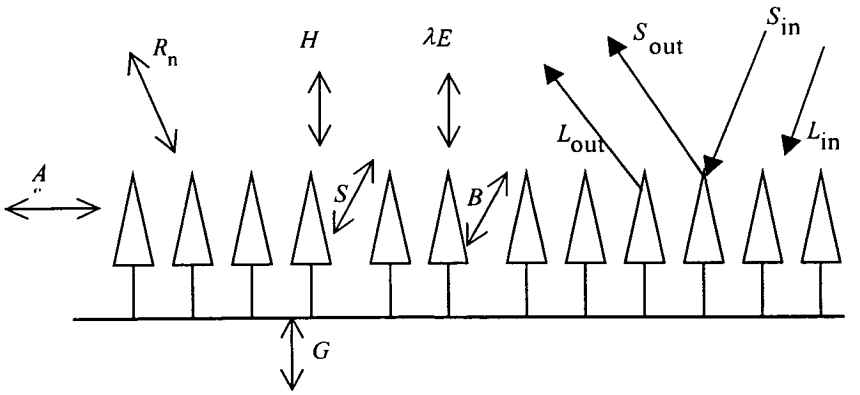

Figure 6-1 Representation of the heat (energy) and radiation budget components of a vegetated surface. R_n is net radiation, H is sensible heat flux, λE is latent heat flux, G is soil heat flux, B is biochemical energy stored by photosynthesis and released by respiration, S is heat storage within the stand and A is the energy removed by horizontal advection. S_{in} is short wave radiation in to the surface, L_{in} is long wave radiation in to the surface, S_{out} is short wave radiation out from the surface and L_{out} is long wave radiation out from the surface.

The storage term in equation (6-3) can be separated into the following three components (Thom, 1975; Lee and Black, 1993):

$$S = S_H + S_{\lambda E} + S_b \qquad (6\text{-}4)$$

where S_H is the rate of change sensible heat stored in the air, $S_{\lambda E}$ is the rate of change latent heat stored in the air and S_b is heat stored in the biomass. The above components can be given as:

$$S_H = \int_{z=0}^{z_m} \rho c_p \frac{\partial T_a}{\partial t} dz \qquad (6\text{-}5)$$

$$S_{\lambda E} = \int_{z=0}^{z_m} \lambda \frac{\partial \rho_q}{\partial t} dz \qquad (6\text{-}6)$$

$$S_b = \int_{z=0}^{z_m} \rho_{veg} c_{veg} \frac{\partial T_{veg}}{\partial t} dz \qquad (6\text{-}7)$$

where ρ_{veg} is the mass of vegetation per unit volume, c_{veg} is the heat capacity of the vegetation T_{veg} is the vegetation temperature and z_m is measurement height of H and E.

Following Thom (1975) and McCaughey (1985) the heat capacity of the vegetation was assumed to be 70 % that of water so that:

$$S_b = 0.7 c_q m_{veg} \Delta T_b \qquad (6\text{-}8)$$

where m_{veg} is the biomass, c_q is the heat capacity of water and ΔT_b is the average change in temperature over time of the biomass (K s^{-1}). The biomass of the stand was estimated to be 8.8 kg m^{-2} (Halliwell and Apps, 1997) and ΔT_b was approximated by measured tree bole temperatures which were made in addition to the measurements described in Chapter 2. Wood temperature was measured at ~1.5 m and 6 m at and two depths (5 mm 10 mm) in two trees from 10 April until November 28 using copper-constantan thermocouples referenced to a thermistor connected to a data logger (Delta-T Devices, Cambridge, UK) where half averages were calculated.

Biochemical storage is the energy required for carbon fixation and following Thom (1975) is given by:

$$B = \mu F_b \qquad (6\text{-}9)$$

where μ is the specific energy fixation of CO_2 (5.06 x 10^5 J mol^{-1}) and F_b is the biotic CO_2 flux.

Measurements, of air temperature and water vapour concentration profiles were used to calculate S_H and $S_{\lambda E}$. The air temperature measurements are not described in chapter 2 but air temperature was measured from 13 May until November 28 at the following heights:1.50 m, 3 m, 6 m 9 m12 m 18 m in addition to the weather station air temperature measurement at 24 m. The measurements were made using copper-constantan thermocouples referenced to a thermistor connected to a data logger (Delta-T Devices, Cambridge, UK) where half hour averages were calculated.

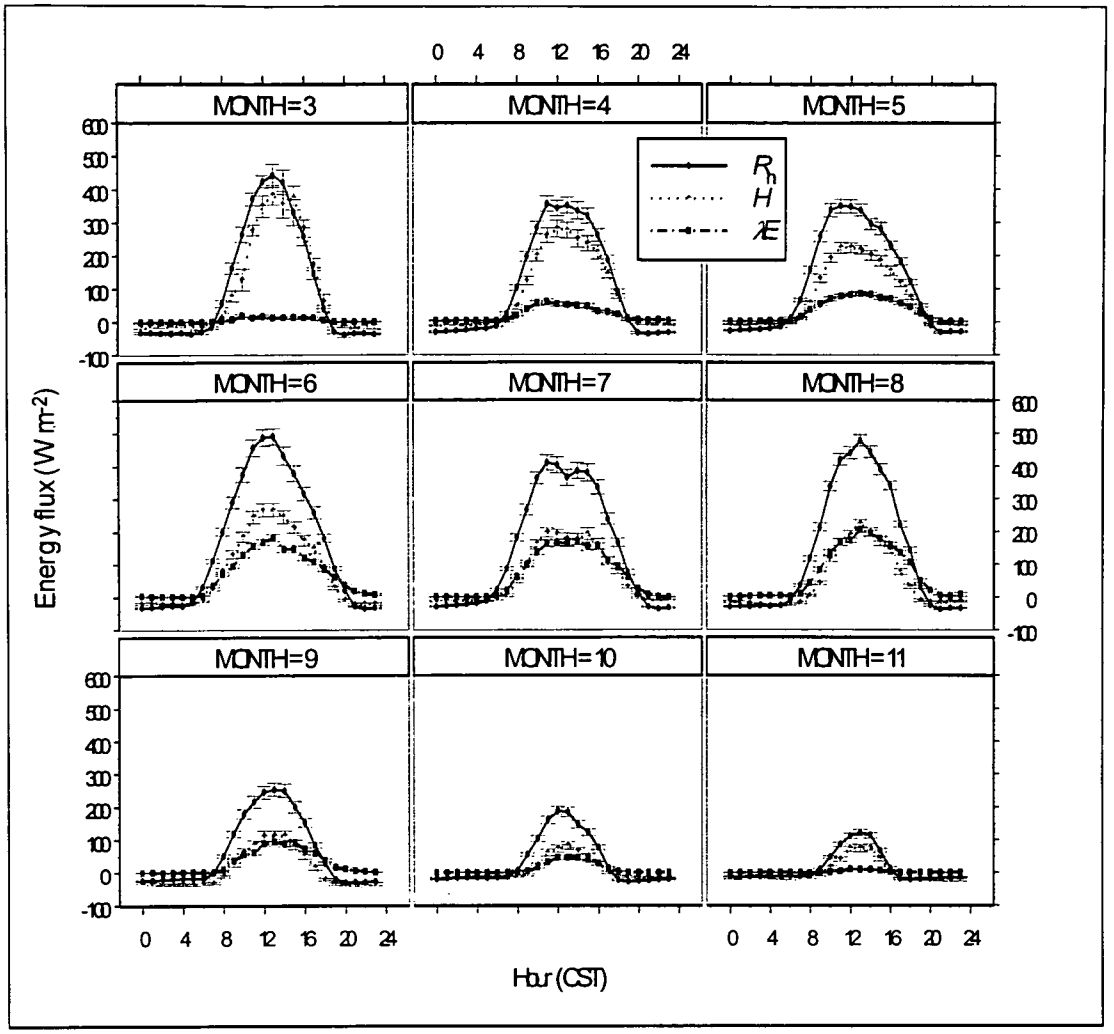

Figure 6-2 Average daily course of net radiation, R_n, sensible heat flux, H, and latent heat flux, λE. Each point is the mean value for the hour before the time shown. Error bars show ± 1 standard error. N.B. The data for March covers only 7 days when there was little cloud.

6.2 Components of the energy balance

The sums of sensible and latent heat fluxes were 80 to 95 % of net radiation over 24 hours and the partitioning of energy between these two fluxes varied seasonally (Figure 6-2). In March λE was close to zero because the water was frozen (Figure 6-3) and H was 80 % of R_n. From March to July the Bowen ratio ($\beta = H/\lambda E$) fell and reached 1.0 in July (Figure 6-2, Figure 6-14). During July, August and September $\beta \approx 1.0$ but increased again in October and November.

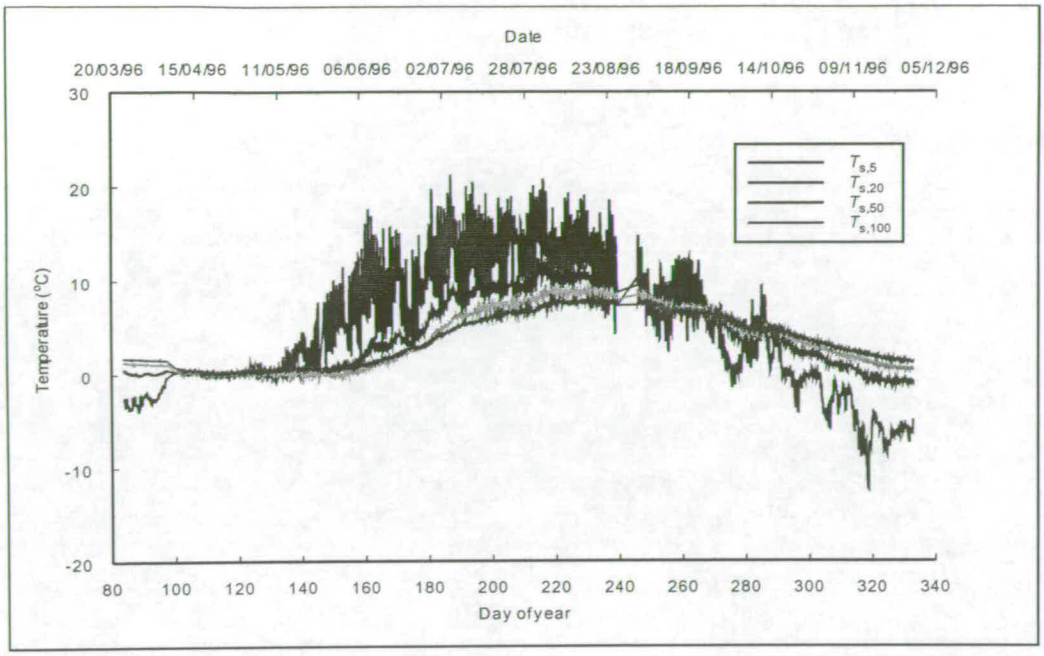

Figure 6-3 Half hour averages of soil temperature at 5, 20, 50 and 100 cm depth ($T_{s,5}$, $T_{s,20}$, $T_{s,50}$, $T_{s,100}$, respectively).

S_b was the largest storage component (Figure 6-4) with extreme values of ±15 W m^{-2} during April to August when the stand was warming or cooling at the beginning and end of the day when it reached 10 % of net radiation. B was directly proportional to the net ecosystem CO_2 flux and reached 4 W m^{-2} in June to August but was zero in March and November (Figure 6-5). S_H (Figure 6-6) was very small (±1 W m^{-2}) with loss of heat during the night increasing towards dawn after which heat was stored more or less steadily through the day until sunset. $S_{\lambda e}$ (Figure 6-7) was of similar magnitude to S_H (±1 W m^{-2}) but was more variable. There was no diurnal cycle but values varied least around midnight and most at noon. Soil heat flux, G, (Figure 6-5) was seasonal. In the coldest months of March and November, G was -5 W m^{-2} with very little diurnal variation when the surface was covered with an insulating layer of snow and was colder than the soil lower down (Figure 6-3). The diurnal variation became more pronounced in the summer months and heat was stored continuously from May to August. The maximum soil heat flux was at solar noon in June when G averaged 10 W m^{-2}.

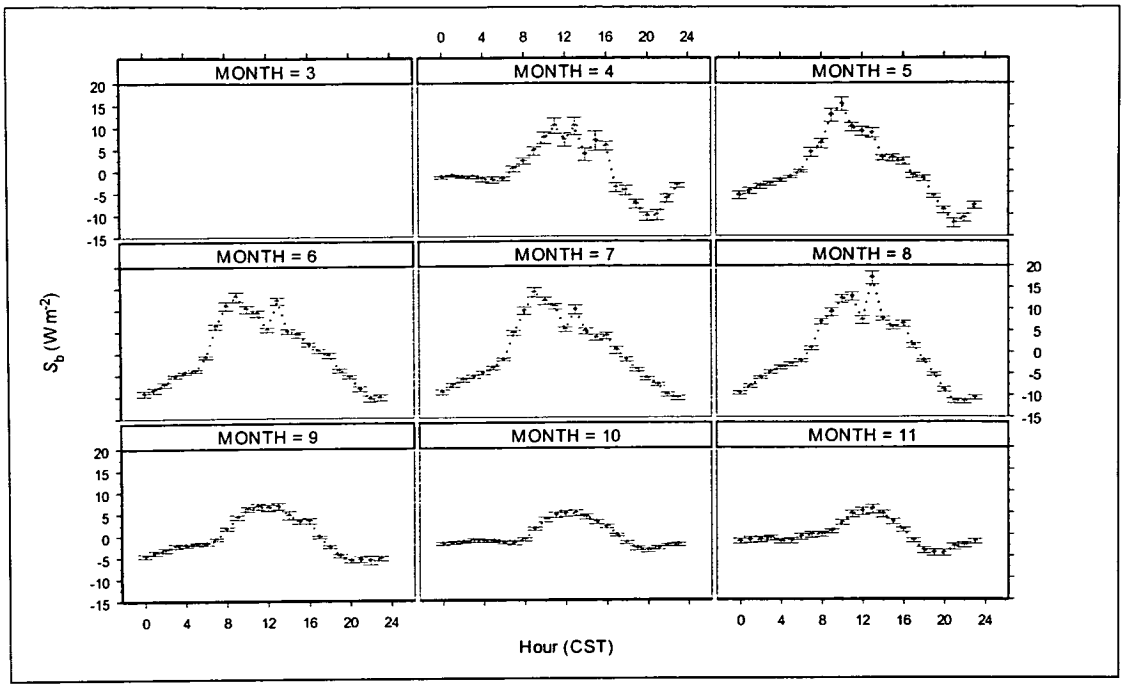

Figure 6-4 Average daily course of heat storage in the vegetation, S_b. Each point is the mean value for the hour before the time shown. Error bars show ± 1 standard error.

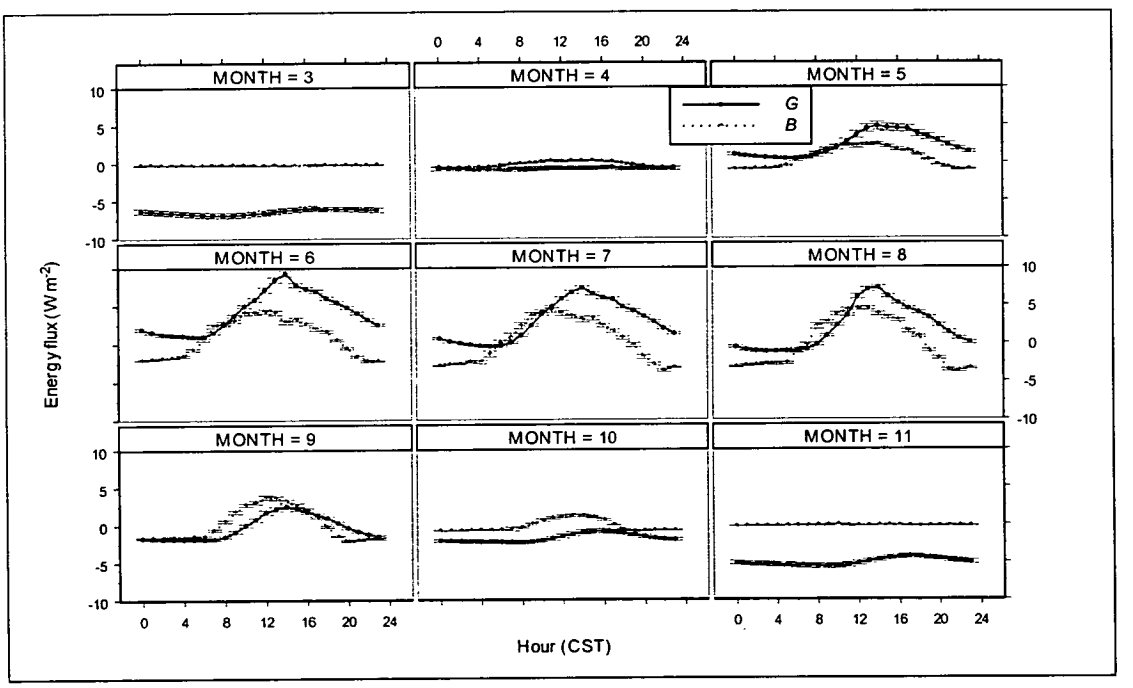

Figure 6-5 Average daily course of soil heat flux, G, and biochemical energy storage, B. Each point is the mean value for the hour before the time shown. Error bars show ± 1 standard error.

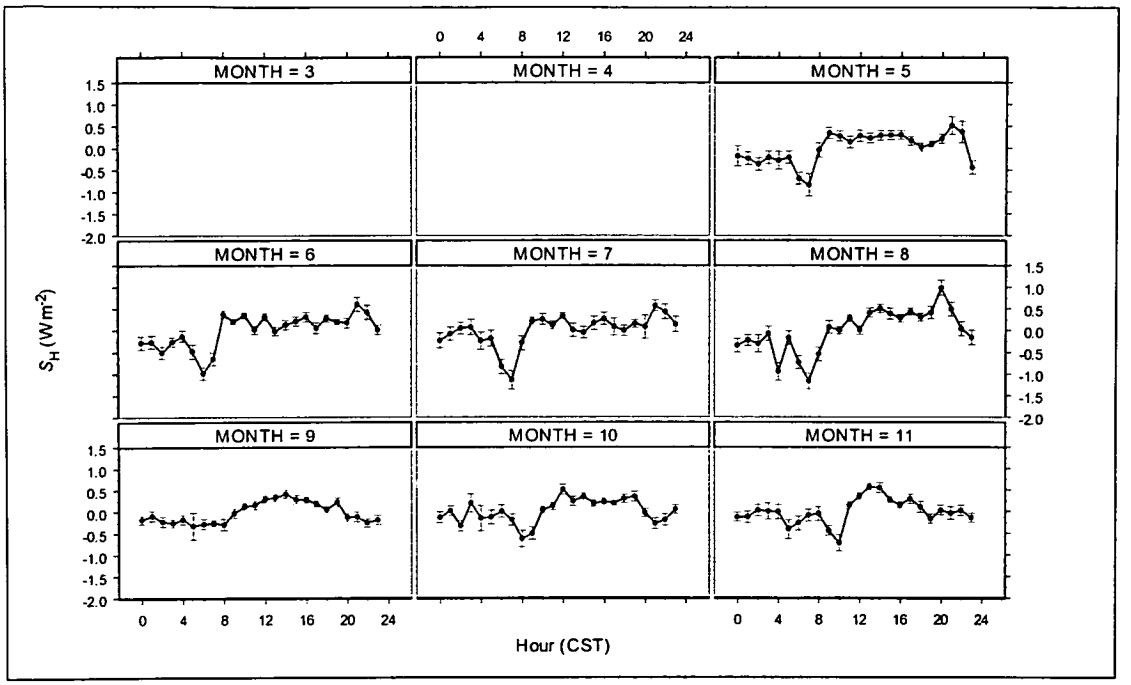

Figure 6-6 Average daily course of sensible heat storage in the air, S_H. Each point is the mean value for the hour before the time shown. Error bars show ± 1 standard error.

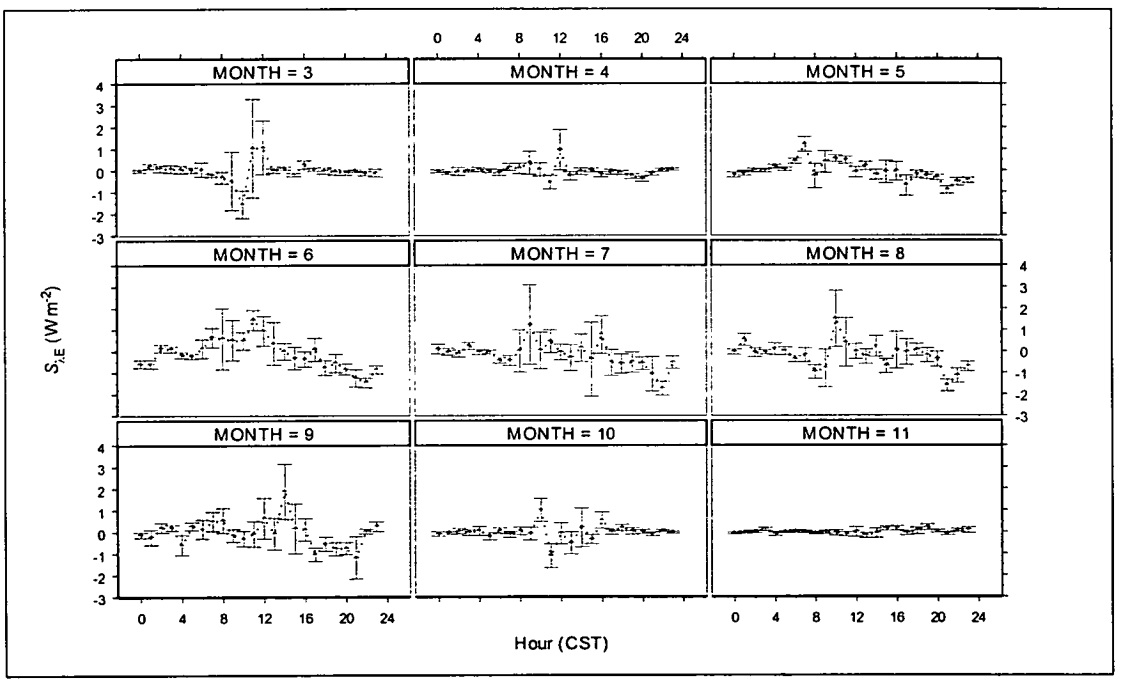

Figure 6-7 Average daily course of latent heat storage in the air, $S_{\lambda E}$. Each point is the mean value for the hour before the time shown. Error bars show ± 1 standard error.

6.3 Energy balance closure

The energy balance closure was analysed by regressing ($H + \lambda E$) against net radiation minus the storage terms ($R_n - G - B - S$) using half-hour averages. This allows the eddy covariance measurements, H and λE, to be compared with those made by other methods. Most studies fail to close the energy balance and this problem is worse for night data (Lee and Black,1993; Goulden *et al.*, 1996). Therefore, the regression was calculated using all data, day only (when $Q > 0$ μmol m^{-2} s^{-1}) and night only (when $Q = 0$ μmol m^{-2} s^{-1}). At night, under stable conditions when mixing is poor, sensible heat flux becomes closer to zero because of the lack of turbulence. Thus the energy balance regressions were recalculated but using only half-hour averages when $u_* > 0.4$ m s^{-1} to investigate the effect of the lack of turbulence on the energy balance. (This is the same threshold value of u_* as used in Chapter 5 when investigating the failure of $F_C + S_C$ to account for respiration.)

Table 6-1 and Figure 6-8 show the results of the regressions using half-hour averages with all values of u_*. Using all data the slope of the regression is 0.86, this improves when using daytime data only, to 0.88, but the slope of the regression using night time data is only 0.38 and r^2 is only 0.06.

	a	b	r^2	N
Day and night	-5.2 ±0.6	0.86±0.003	0.91	9369
Day	-9.7 ±1.0	0.88±0.004	0.89	5708
Night	-11.2 ±0.5	0.28±0.017	0.06	3632

Table 6-1 Energy balance regression parameters of the form ($H + \lambda E$) = a + b($R_n - G - B - S$) using half hour averages. Error terms are one standard error.

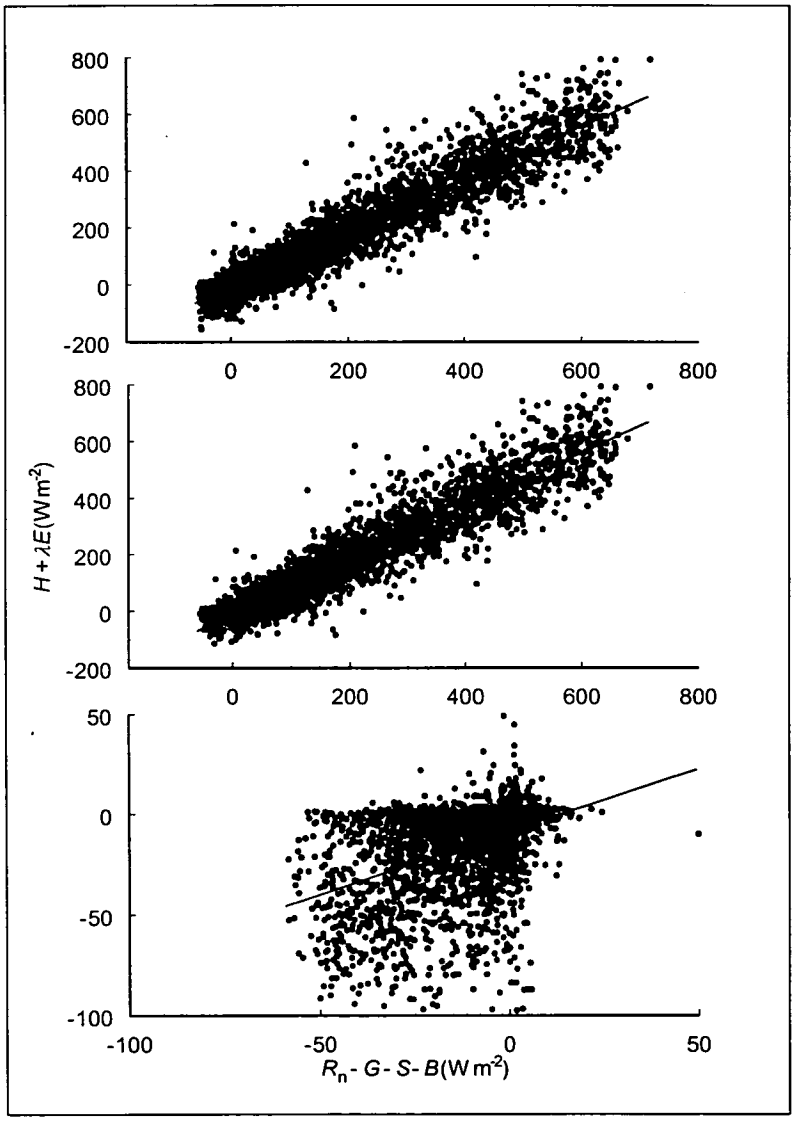

Figure 6-8 Scatter plots with regression lines of ($H + \lambda E$) against (R_n - G - B - S) using observations with all values of u_*, for day and night (top), day only (middle) and night only (bottom). Table 6-1 shows the regression parameters.

When half hour averages with $u_* < 0.4$ m s-^{1} were excluded (Table 6-2 and Figure 6-9) the slope of the regression increased by 0.04 for when day and night data were used and 0.02 for day time only data. For night time only data, the slope was increased by 0.52 to 0.8 and r^2 increased to 0.27.

These results show failure to close the energy balance and the closure is worse when mixing is poor. This imbalance may be caused by underestimation of H, λE, S, G or B, over estimation of R_n or the failure to include a significant component of the energy balance. Energy balance closure is most sensitive to errors in the largest components R_n, H and λE. Efforts have been made to reduce errors in the EC measurements (H and λE, see Chapter 4) and it is unlikely that remaining errors would balance the energy budget. The net radiometers used to obtain R_n were calibrated as part of an intercalibration of BOREAS net radiation measurements against a secondary standard traceable back to international standards (Hodges and Smith, 1997). Although uncertainties in R_n measurement in the field by net radiometers are 5 to 10 % (Smith *et al.*, 1997), R_n is systematically larger than the sum of other components measured in reported studies. This leaves the possibility of having neglected a significant component of the energy balance. Either horizontal advection (Thom, 1975) and/or vertical advection caused by non-zero $\overline{w}$ (Lee, 1997) may be the missing component.

	a	b	r^2	N
Day and night	-12.7±1.3	0.90 ±0.005	0.90	4247
Day	-9.2±1.7	0.90 ±0.006	0.88	3414
Night	-22.8±1.3	0.80 ±0.046	0.27	806

Table 6-2 Energy balance regression parameters of the form ($H + \lambda E$) = a + b(R_n - G - B - S) using half hour averages where $u_* > 0.4$ m s-1. Error terms are one standard error.

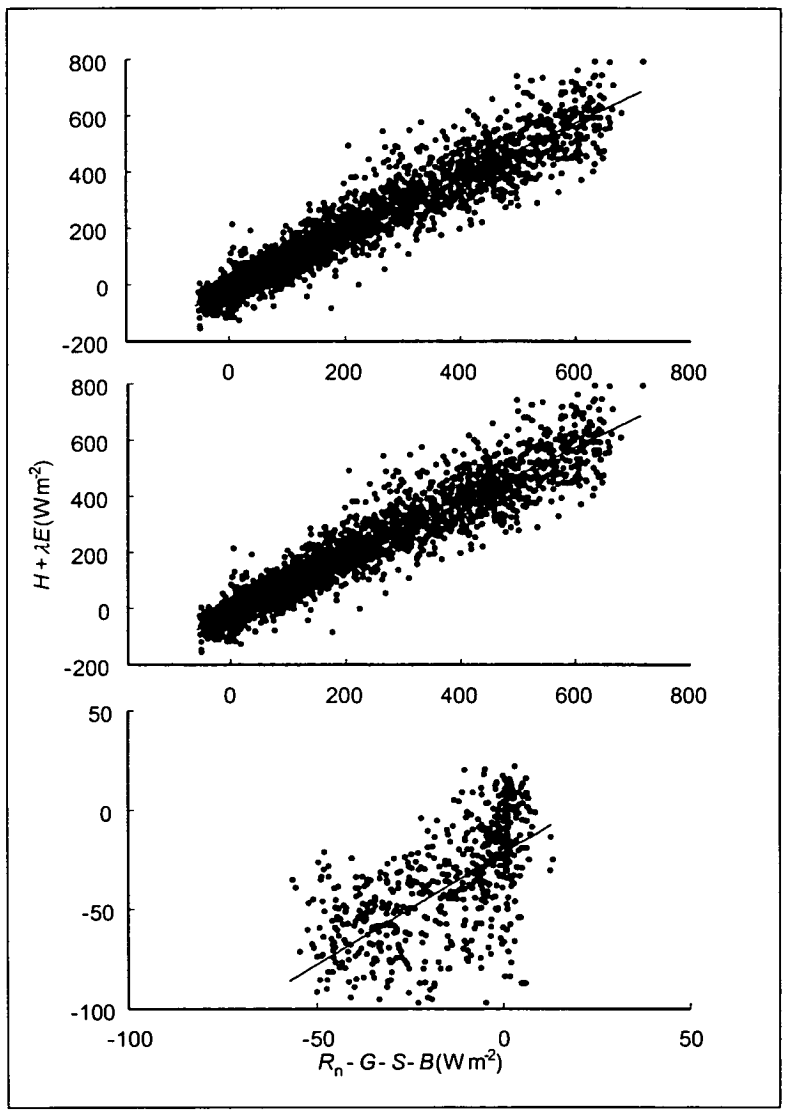

Figure 6-9 Scatter plots with regression lines of ($H + \lambda E$) against (R_n - G - B - S) where $u_* > 0.4$ m s^{-1} for: day and night (top), day only (middle) and night only (bottom). Table 6-2 shows the regression parameters.

6.4 Resistances

Latent heat flux is determined by net radiation, vapour pressure deficit and stomatal and boundary layer resistances as described by the Penman-Monteith equation:

$$\lambda E = \frac{sA_E + \rho c_P D / r_{a,h}}{s + \gamma \left(r_{a,V} + r_{st,v} \right) / r_{a,h}} \qquad (6\text{-}10)$$

where s is the rate of change of the saturated vapour pressure of water with respect to temperature, A_E is the available energy ($H + \lambda E = R_n - G - B - S$), D is the water vapour pressure saturation deficit, γ is the psychrometric constant, $r_{a,h}$ and $r_{a,v}$ are the boundary layer resistances to heat and water vapour respectively and r_{st} is the canopy bulk stomatal resistance to water vapour (Monteith, 1965).

Assuming equality of $r_{a,v}$, $r_{a,h}$, equation (6-10) can be rearranged to give the canopy resistance, $r_{c,v} = r_{st,v} + r_{a,v}$, (Thom, 1975; Jarvis *et al.*, 1976):

$$r_{c.v} = \left[(s/\gamma)\beta - 1 \right] r_{a,v} + (\beta + 1) r_i \qquad (6\text{-}11)$$

where β is the Bowen ratio ($H/\lambda E$) and r_i is the isothermal or climatalogical resistance (Monteith, 1975):

$$r_i = (\rho c_P / \gamma)(D / R_n) \qquad (6\text{-}12)$$

Assuming equality of boundary layer (aerodynamic) resistances to water vapour flux and sensible heat flux with the momentum resistance, $r_{a,m}$, will cause little error in the calculation of $r_{c,v}$ using equation (6-11) because the term including $r_{a,v}$ is much smaller than the term including r_i.

$$r_{a,v} \approx r_{a,h} \approx r_{a,m} = u / u_*^2 \qquad (6\text{-}13)$$

The coupling factor, Ω, (McNaughton and Jarvis, 1983; Jarvis and McNaughton, 1986) quantifies the degree of coupling between the vegetation and atmosphere. If the vegetation is well coupled, D close to the vegetation will the same as that above the canopy and will be independent of transpiration rate, which will be at the

equilibrium rate, E_{eq}. If the vegetation is poorly coupled, water vapour evaporated by the vegetation will not be transported away and D will be dependent on the transpiration rate, which will be at the imposed rate, E_{imp}.

$$E = \Omega E_{eq} + (1-\Omega)E_{imp} \qquad (6\text{-}14)$$

$$E_{imp} = \rho_v D \Big/ r_{c,v} P \qquad (6\text{-}15)$$

$$E_{eq} = \frac{\varepsilon A_E}{\varepsilon + 1} \qquad (6\text{-}16)$$

$$\Omega = \frac{\varepsilon + 1}{\varepsilon + 1 + r_{c,v}/r_{a,h}} \qquad (6\text{-}17)$$

$$\varepsilon = s/\gamma \qquad (6\text{-}18)$$

P is atmospheric pressure and ρ_v is water vapour partial pressure.

McNaughton and Jarvis (1983) suggest Ω has a value between zero and one and a typical value for forest is 0.2 and for short grass 0.8.

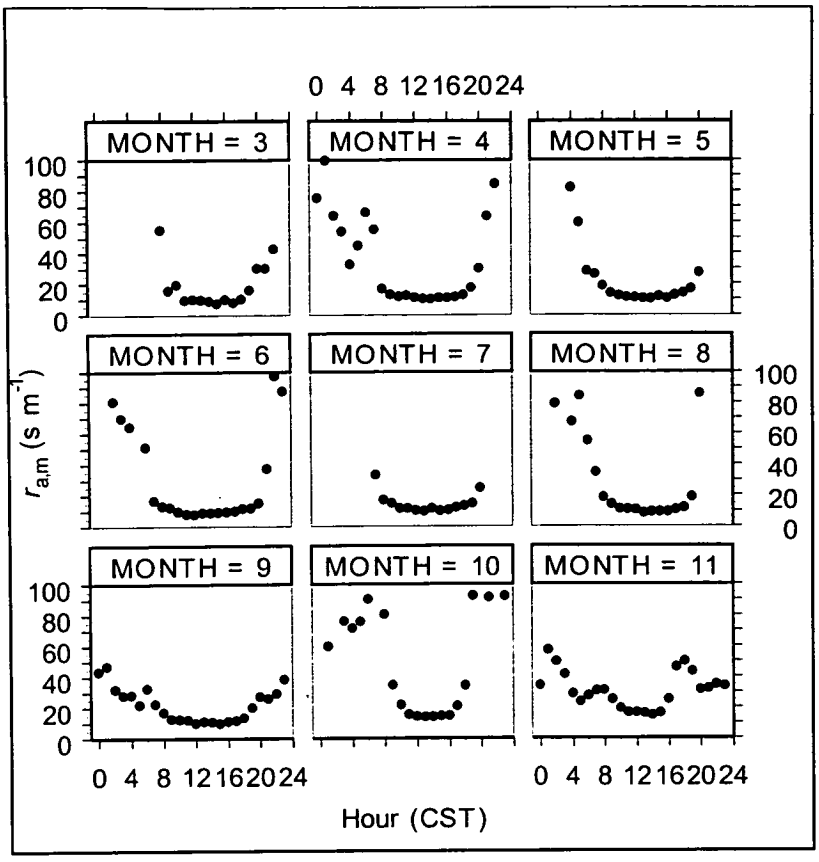

Figure 6-10 Average daily course of boundary layer resistance, $r_{a,m}$, for each month. Each point is the median value for the hour before the time shown. Where points are missing, $r_{a,m} > 100$ s m^{-1}.

Boundary layer resistance was ~10 s m^{-1} during the day for all months except November and December when it was ~15 s m^{-1} (Figure 6-10). At night during stable conditions $r_{a,m}$ was much higher, up to 200 s m^{-1}, because $r_{a,m}$ is a function of turbulent mixing.

The climatological resistance, r_i, followed the diurnal course of $1/R_n$ and so was small during the day and large at night (Figure 6-11). The influence of D was largely seasonal. The smallest r_i during the day, was 4 s m^{-1} in March when D was smallest and increased to 32 s m^{-1} in June. After June, the smallest day time value of r_i fell to 20 s m^{-1} in November as D decreased with temperature through autumn. The average diurnal courses of r_i for summer months reported here lie between similar curves measured in summer in Britain (lowest value ~20 s m^{-1}) and British Colombia (lowest value ~50 s m^{-1}) (Jarvis *et al.*,1976).

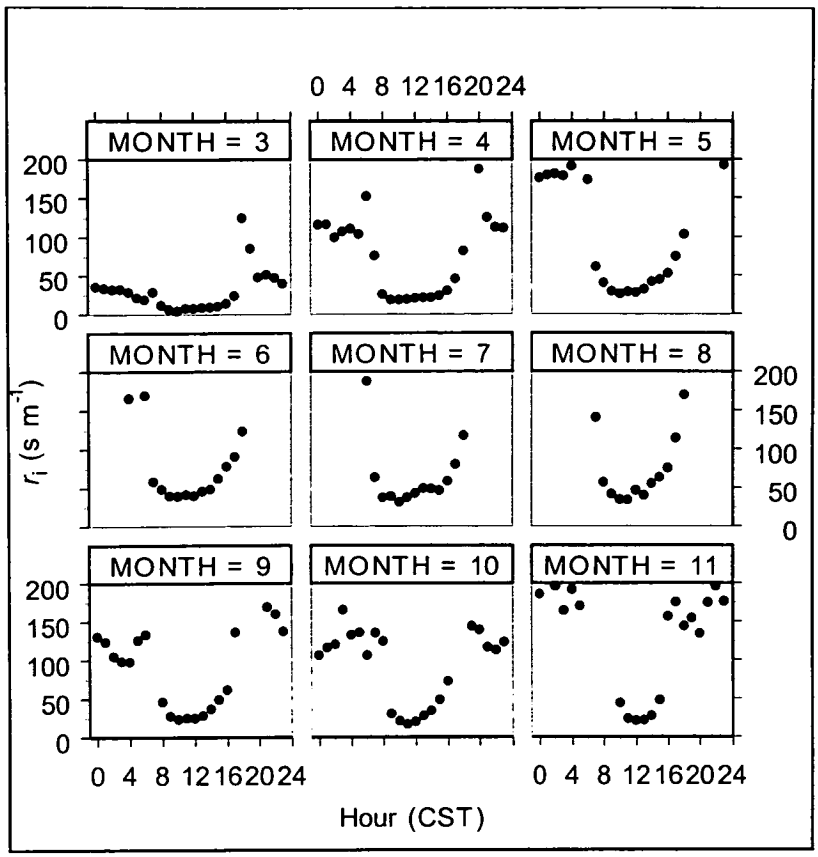

Figure 6-11 Average daily course of climatalogical resistance, r_i, for each month. Each point is the median value for the hour before the time shown. Where points are missing, $r_i > 200$ s m^{-1}.

Shortly after dawn $r_{c,v}$ fell from values over 400 s m^{-1} (presumably when stomata were closed) to values of 100 s m^{-1} or less except in March and November when the lowest mean hourly $r_{c,v}$ was ~200 s m^{-1} (Figure 6-12). Values of $r_{c,v}$ rose through the day to 400 s m^{-1} about two hours before sunset. Lee and Black (1993) reported a similar trend in $r_{c,v}$ for Douglas-fir in July/August, under some water stress, with a low morning value of 200 s m^{-1}. Jarvis *et al.* (1976) also show similar diurnal curves for: Sitka spruce, Scots pine and Douglas-fir. Morning low values of $r_{c,v}$ were 50 to 100 s m^{-1} and increased through the day except for the Sitka spruce, where $r_{c,v}$ remained at ~100 s m^{-1} until the end of the reported sequence at 18:00 hours.

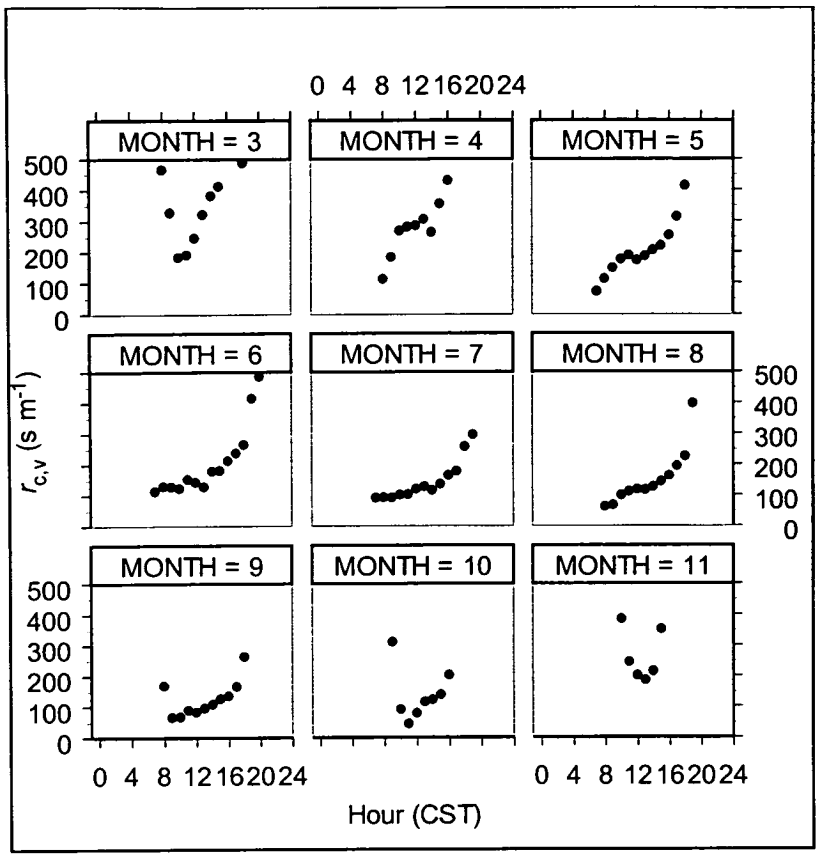

Figure 6-12 Average daily course of bulk stomatal resistance, $r_{c,v}$, for each month. Each point is the median value for the hour before the time shown. Where points are missing, $r_{c,v} > 500$ s m^{-1}.

Early morning values of Ω (Figure 6-13) were high when $r_{a,m}$ was high, in stable or perhaps neutral conditions and values fell through the day as $r_{c,v}$ increased (Figure 6-12). Ω was lower during the early and later months and highest in summer reflecting the seasonal trend in $r_{c,v}$. These values for Ω indicate strong coupling and that transpiration followed D and was controlled by $r_{c,v}$, i.e transpiration was weighted to the imposed rate (equation 6-15).

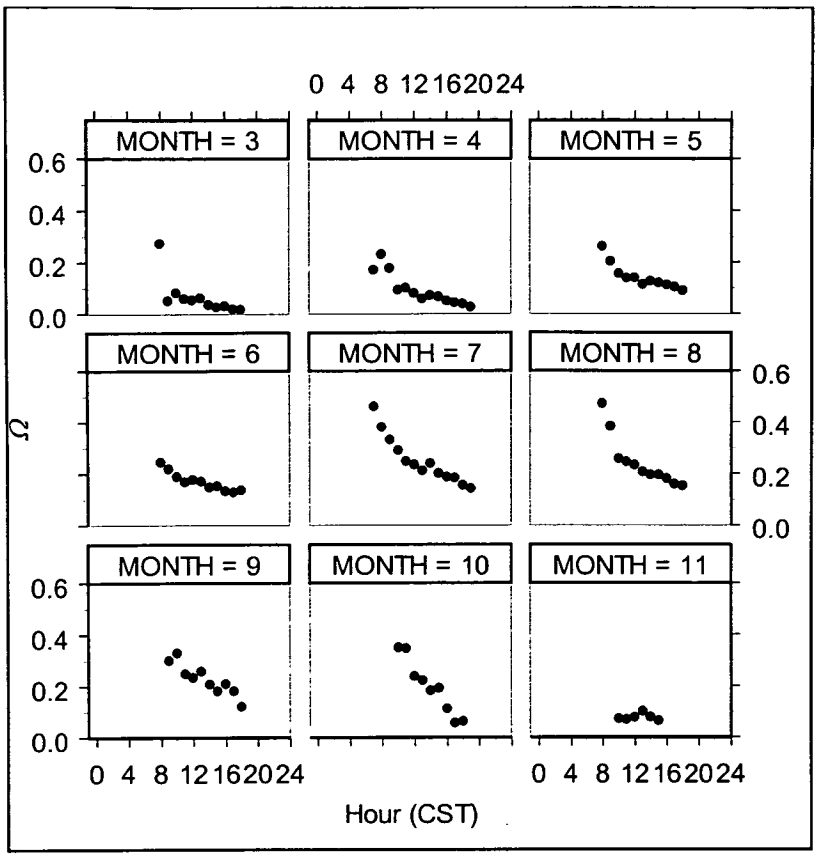

Figure 6-13 Average daily course of the coupling coefficient, Ω, for each month. Each point is the median value for the hour before the time shown.

6.5 Seasonal partitioning of energy between H and λE (Bowen ratio)

Daily values of β for each month are shown in Figure 6-14. At night λE is usually small but positive ($0 < \lambda E < 3$ W m^{-2}) but when dew forms $\lambda E < 0$. When there is a temperature inversion at night H is negative (heat transfer to the surface) and $\beta < 0$. During the day and at night when there is no temperature inversion H is positive and $\beta > 0$. During the day the heat supplied to the surface causes evapo-transpiration if water is available either free standing or when $r_{c,v}$ is small. During March and November, λE was very small because most of the water was frozen (see Figure 6-3 for soil temperatures). β calculated for these periods is very variable because it is the result of dividing by a very small number. At dawn, β was zero when H was zero and then increased to a maximum at noon, as H increased faster than λE (Figure 6-14). After noon, H decreased more quickly than λE and, therefore, β decreased to become

zero when H became zero. After sunset β became negative and during the night was very variable because λE was very small.

As described in section 6.2 *Energy balance components*, β varied seasonally with a mean mid-day value of 17 in March which then decreased to ~1 in July and August and then increased again to 6 in November (Figure 6-14). The mean summer mid-day values were low (~1) but some half-hour averages reached ~2 on sunny days when temperature and D were high. This seasonal variation in β is investigated below.

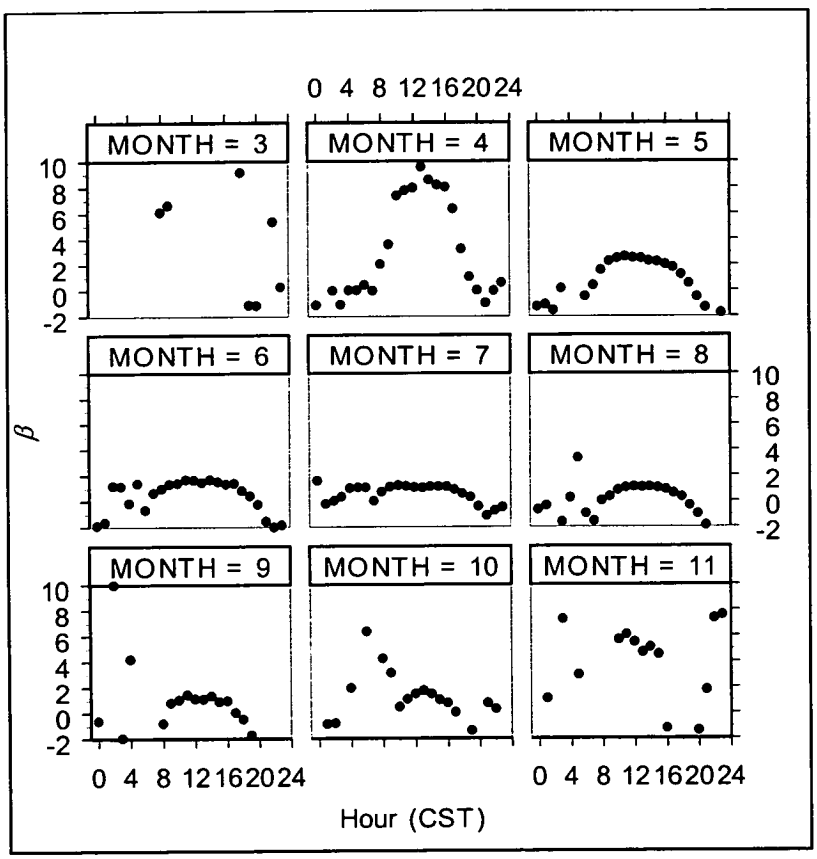

Figure 6-14 Average daily course of Bowen ratio, β, for each month. Each point is the median value for the hour before the time shown. Where points are missing, $\beta > 10$ or $\beta < -2$.

Following Jarvis *et al.* (1976) by combining equation 6-10 and 6-12 and rearranging:

$$\beta = \frac{\varepsilon + 1 + r_{c,v}/r_{a,h}}{\varepsilon + r_i/r_{a,h}} - 1 \quad (6\text{-}19)$$

From equation 6-19 it is evident that β increases with increasing $r_{c,v}$ and decreasing r_i and these resistances are the dominant terms. During the cold months D is low, forcing r_i low (equation 6-12). Also, during the colder months, shoot water potentials went down to –2.5 MPa (P. G. Jarvis, unpublished data). Low shoot water potentials cause high stomatal resistance (Jones, 1992).

As described earlier, $\Omega < 0.2$ during the day (except early in the morning before surface heating forced turbulent mixing) which implies transpiration rate is weighted towards E_{imp} and so is forced by D and controlled by $r_{c,v}$ (equation 6-15). Equation 6-19 and the values of Ω weighting E to E_{imp} both predict that β would be high in March and November when D was low and $r_{c,v}$ high. They also predict that β would decrease in the summer as D increased and $r_{c,v}$ decreased.

6.6 Radiation balance

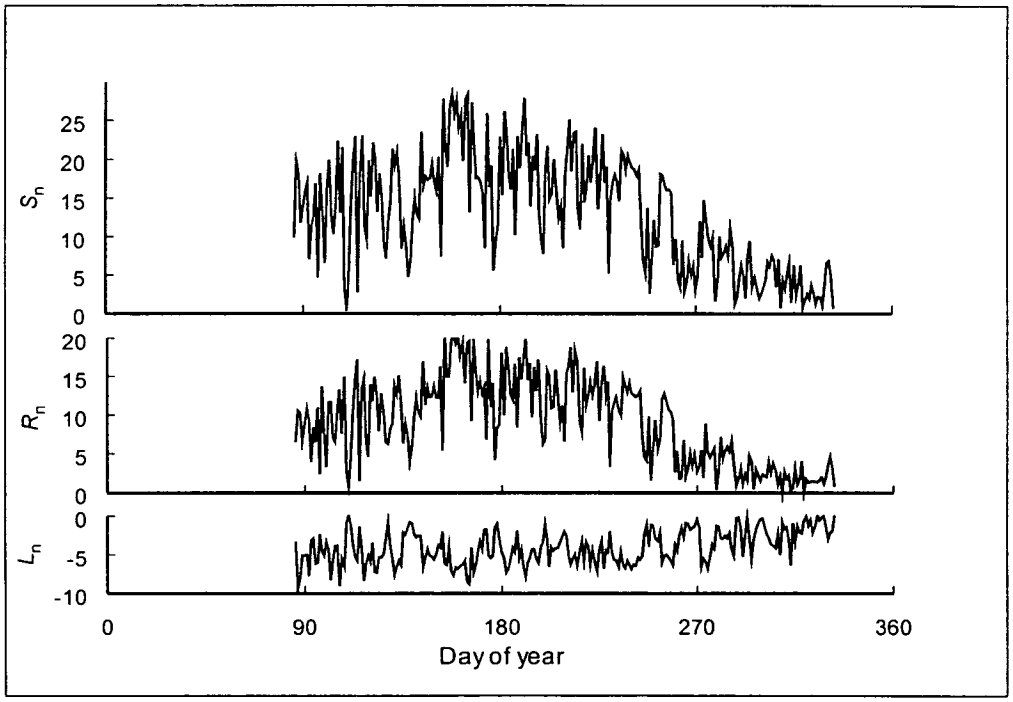

Figure 6-15 Radiation balance for the period 26 March (day 86) to 29 November 1996 (day 334) S_n is net shortwave radiation, R_n is net all wave radiation and L_n is net longwave radiation (MJ m^{-2} day^{-1}). L_n was calculated as $S_n - R_n$.

Measurements began just after the vernal equinox and solar radiation was already quite high at 20 MJ m^{-2} day^{-1} (Figure 6-15). A cloudy, rainy period in May reduced

S_n substantially and even in June and July S_n was reduced to ~7 MJ m^{-2} day^{-1} on very cloudy days, when on cloudless days in June and July S_n reached 26 MJ m^{-2} day^{-1}.

After the summer solstice S_n became less as the mid-day zenith angle increased. R_n followed S_n very closely. Linear regression between R_n and S_{in} showed that R_n was 73 % of S_{in} with an r^2 of 0.98 (Figure 6-16). A linear regression showed R_n to be 80 % of S_n with an r^2 of 0.98 (Figure 6-17). These results agree well with a study of the same relationships using data collected at the Saskatchewan Research Council Automated Meteorological System sites throughout the BOREAS area (Kaminsky and Dubayah, 1997). 24 hour totals of L_n showed no overall trend from day 86 (26 March) to about day 200 (18 July) despite the increase in S_n during the same period. Half hour averages of L_n were ~200 W m^{-2} on cloudless days over the same period. After day 200, 24-hour totals of L_n became higher (less negative) as S_n decreased and nights became longer (Figure 6-15).

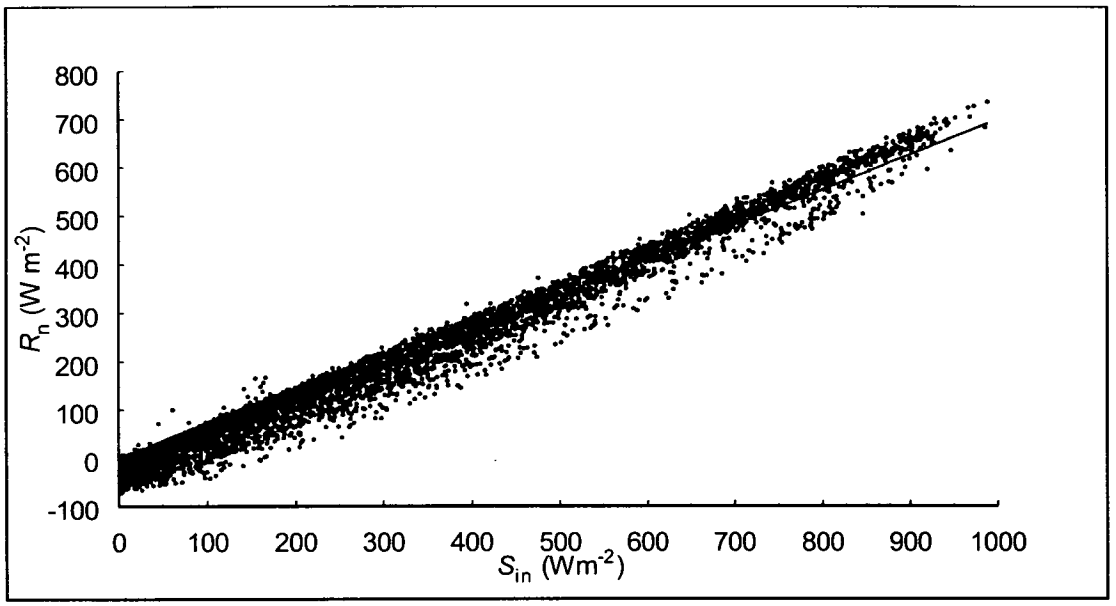

Figure 6-16 Scatter plot of R_n versus S_{in}. The linear regression equation is $R_n = (-27.51 \pm 0.52) + (0.73 \pm 0.0018)\ S_{in}$; $r^2 = 0.98$; N = 11736; RMSE = 22.98 Error terms are 95 % confidence intervals.

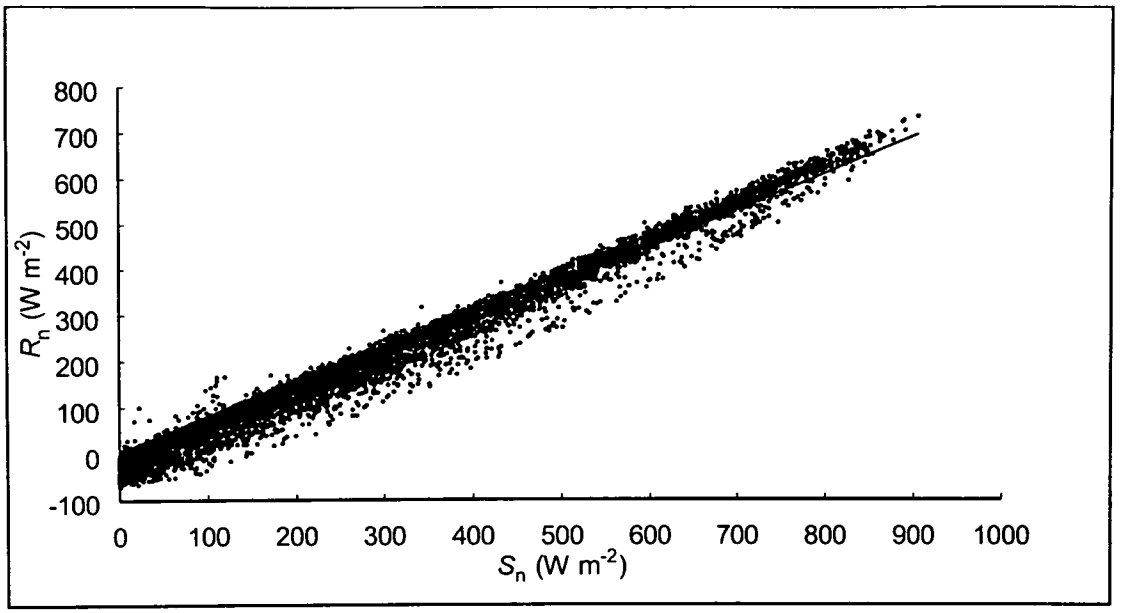

Figure 6-17 Scatter plot of R_n versus S_n. The linear regression equation is $R_n = (-25.45 \pm 0.51) + (0.80 \pm 0.0020)\ S_n$; $r^2 = 0.98$; N = 11736; RMSE = 22.49 Error terms are 95 % confidence intervals.

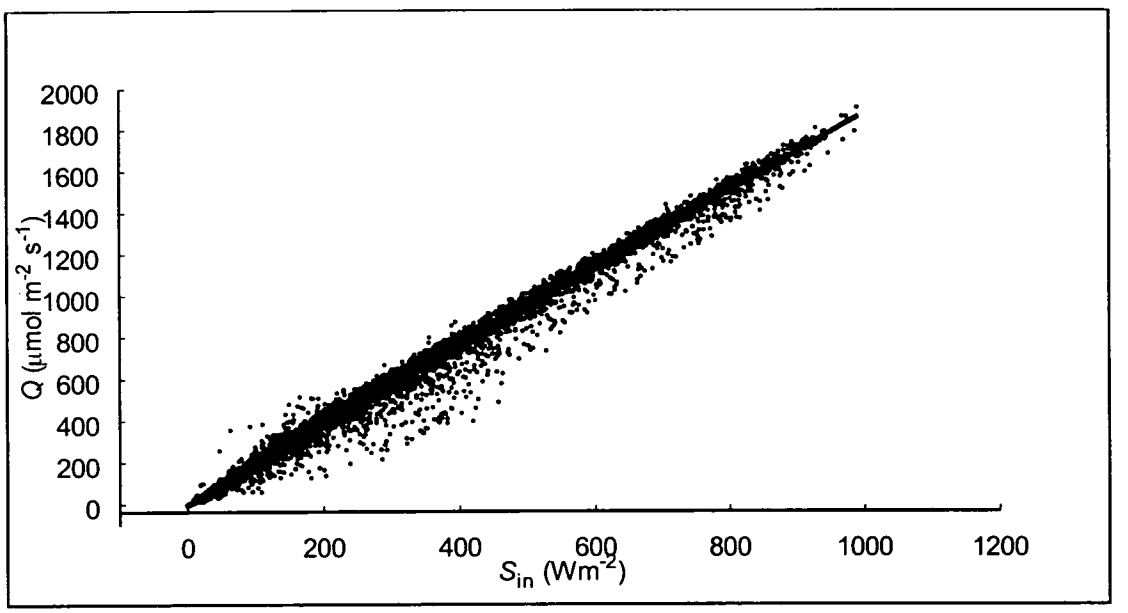

Figure 6-18 Scatter plot of S_{in} versus PPFD, Q, the linear regression equation is $S_{in} = (-3.28 \pm 0.84) + (1.89 \pm 0.028)\ Q$; $r^2 = 0.99$; N = 11693; RMSE = 36.88. Error terms are 95 % confidence intervals.

The relationship between S_{in} and Q was also investigated by linear regression for the period day 85 to day 334. The relationship was found to be, 1 W m^{-2} = 1.89 µmol m^{-2} s^{-1} (Figure 6-18), whereas Jarvis (1993) found the relationship to be 1

W m^{-2} = 2.06 μmol m^{-2} s^{-1} for 300 hours of summer data measured over Sitka spruce in Scotland. This difference could lie in calibrations or in the degree of cloudiness (it is likely to have been more cloudy in Scotland). Table 6-5 shows 1 W m^{-2} = 2.11 μmol m^{-2} s^{-1} on a very cloudy day at SSA OBS and in Scotland 1 W m^{-2} > 2 μmol m^{-2} s^{-1} has been observed (P.J. Jarvis, pers. comm.).

To investigate the variability of these relationships, two cloudless days and two cloudy days were selected in March, June and September. Data from these days were used to calculate linear regression equations for R_n versus S_{in}, R_n versus S_n and S_{in} versus Q. Figure 6-19 shows the time series of S_{in}, L_n and R_n for these days. Values of S_{in} reach 800 W m^{-2} on 27 and 28 March, 900 W m^{-2} on 6 and 8 June and 700 W m^{-2} on 13 and 14 September. The values of S_{in} for 13 and 14 September seem low because those dates were close to the autumnal equinox and so were not expected to be less than the values on 27 and 28 March. Although 13 and 14 September were selected as cloudless days there was some smoke from forest fires in the atmosphere. Nevertheless, these were the best days that could be selected for autumn.

R_n followed S_{in} closely. L_n reached values of ~-200 W m^{-2} on the cloudless days and in March, L_n is lowest at -235 W m^{-2} and in September the lowest value was -150 W m^{-2}. On cloudy days S_{in} was reduced and the sinusoidal shape of the time series graph was disrupted. L_n increased (became less negative) presumably because L_{in} increased as a result of radiation from cloud at a higher temperature than the sky (Stefan's Law).

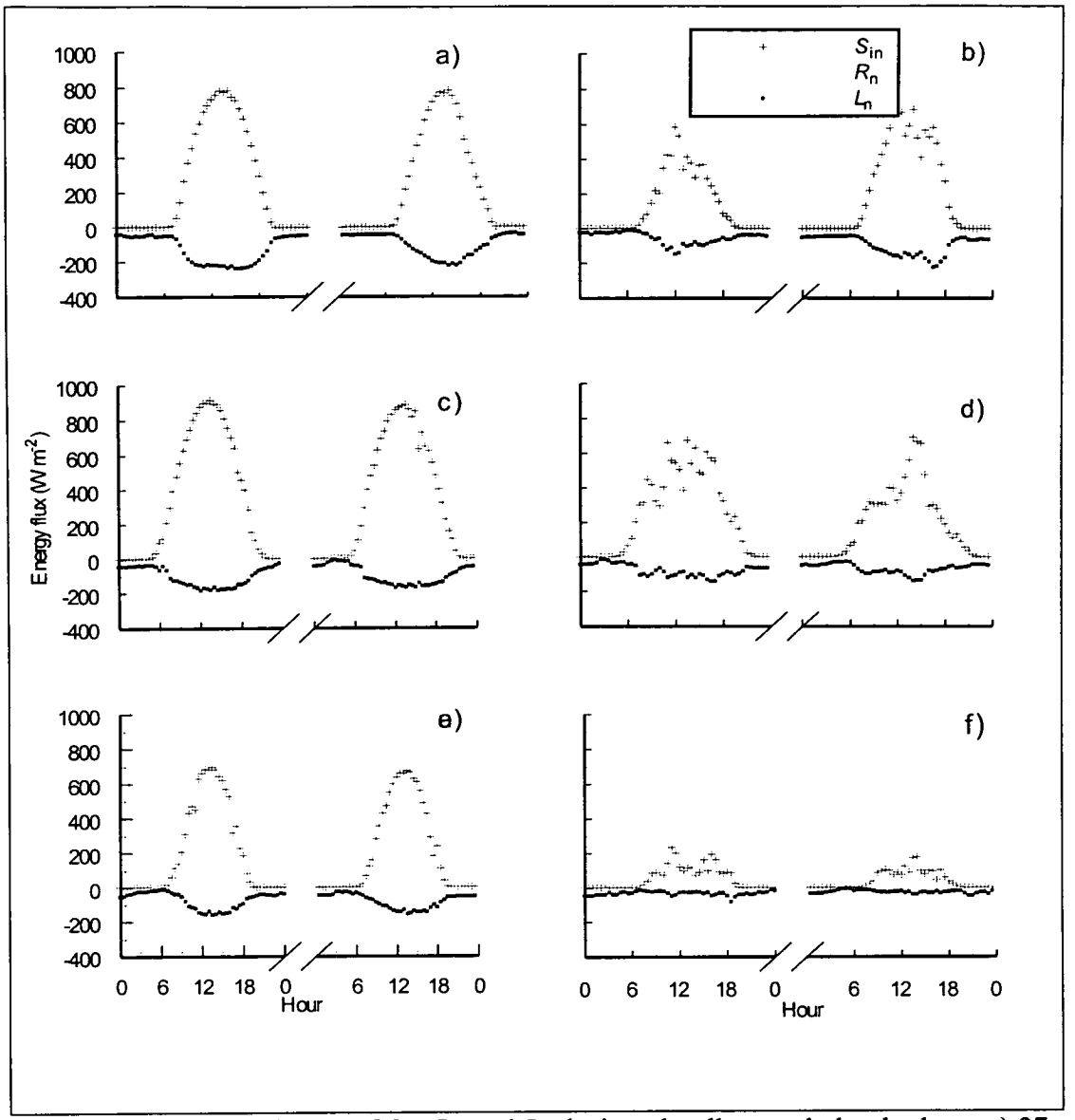

Figure 6-19 Diurnal fluxes of S_{in}, R_n and L_n during cloudless and cloudy days: a) 27 and 28 March [cloudless], b) 26 March and 1 April [cloudy], c) 6 and 8 June [cloudless], d) 11 and 23 June [cloudy], e) 13 and 14 September [cloudless] and f) 18 and 19 September [cloudy].

Correlations of R_n against S_{in} and S_n for the same days (Table 6-3 and Table 6-4) were equally good ($r^2 \geq 0.98$, $p < 0.0001$). The slope of R_n against S_n was generally ~8 % higher than that of R_n against S_{in}. Offsets on cloudy days were closer to zero than on cloudless days as expected. The offset was caused by night time L_n which is increased by cloud cover. However, only the difference between cloudy/cloudless in September was significantly different at the 95 % level. Night time L_n was least in March (largest loss) and most (smallest loss) in September as shown by the offset. It may be that this trend was driven by the temperature difference between surface and

sky that would decrease from March to September as the surface warmed the atmosphere. Differences in the slopes of the regression between cloudy and cloudless days in the same month were not significantly different at the 95 % level.

Date	Cloud less	Offset	Slope	r^2	N
March 27,28	Yes	-51.38±3.00	0.77±0.009	0.99	96
March 26, April 1	No	-34.06±3.14	0.80±0.013	0.98	96
June 6,8	Yes	-42.81±2.92	0.88±0.006	0.99	96
June 11,23	No	-41.24±2.22	0.90±0.008	0.99	96
September 13,14	Yes	-37.47±2.32	0.86±0.008	0.99	96
September 18,19	No	-19.51±1.85	0.98±0.027	0.93	96

Table 6-4 Table of linear regression parameters of R_n versus S_n during cloudless and cloudy days. The error term is ± 1 standard error. Figure 6-20 shows scatter plots of R_n versus S_n.

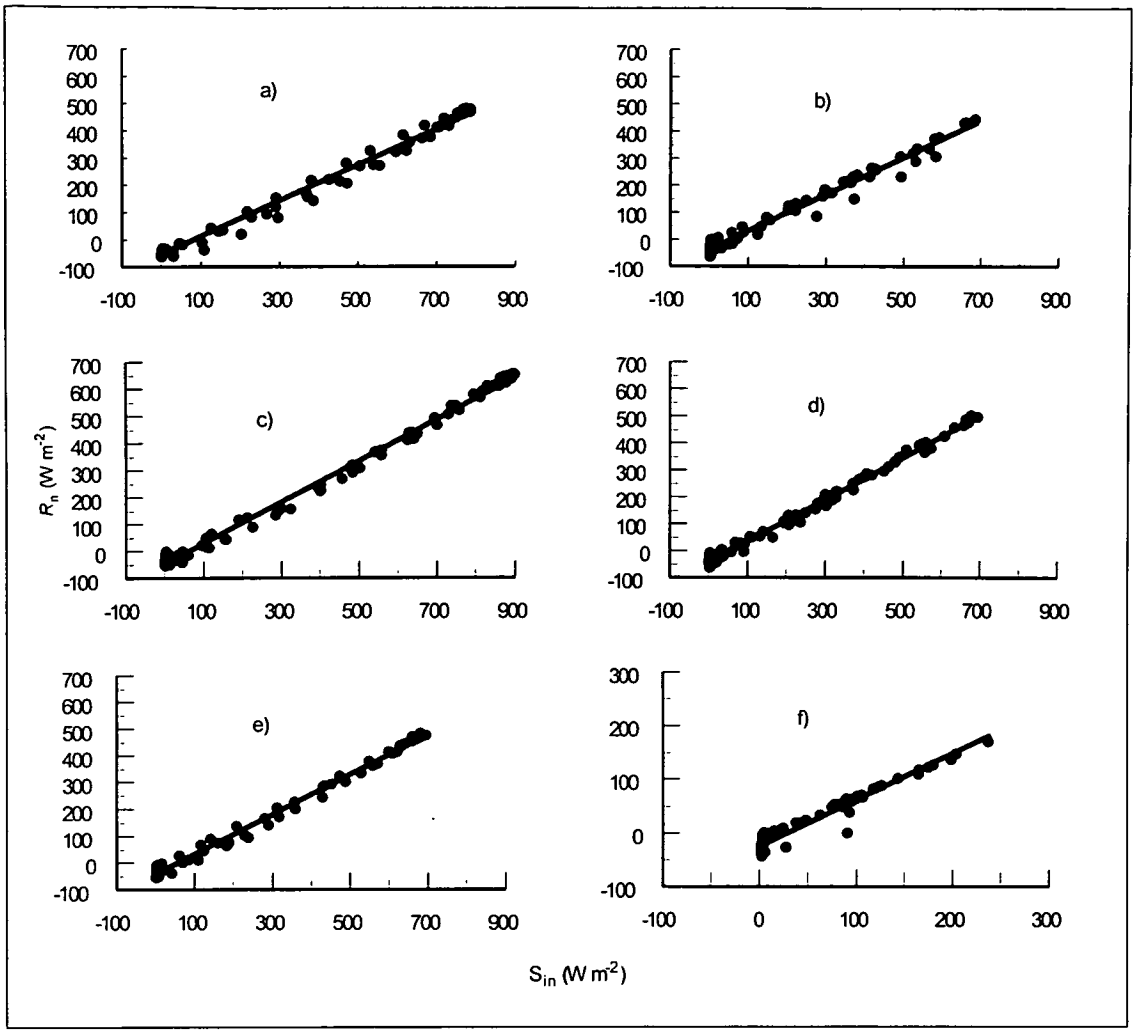

Figure 6-20 Scatterplots of R_n versus S_{in} during cloudless and cloudy days: a) 27 and 28 March [cloudless], b) 26 March and 1 April [cloudy], c) 6 and 8 June [cloudless], d) 11 and 23 June [cloudy], e) 13 and 14 September [cloudless] and f) 18 and 19 September [cloudy]. Table 6-3 shows the regression parameters.

Date	Cloudless	Offset	Slope	r^2	N
March 27,28	Yes	-52.60±2.87	0.69±0.007	0.99	96
March 26, April 1	No	-36.92±2.98	0.72±0.011	0.98	96
June 6,8	Yes	-45.14±3.10	0.80±0.006	0.99	96
June 11,23	No	-43.20±2.33	0.82±0.007	0.99	96
September 13,14	Yes	-39.63±2.42	0.78±0.007	0.99	96
September 18,19	No	-21.20±1.91	0.90±0.025	0.93	96

Table 6-3 Table of linear regression parameters of R_n versus S_{in} during cloudless and cloudy days. The error term is ± 1 standard error. Figure 6-20 shows scatter plots of R_n versus S_{in}.

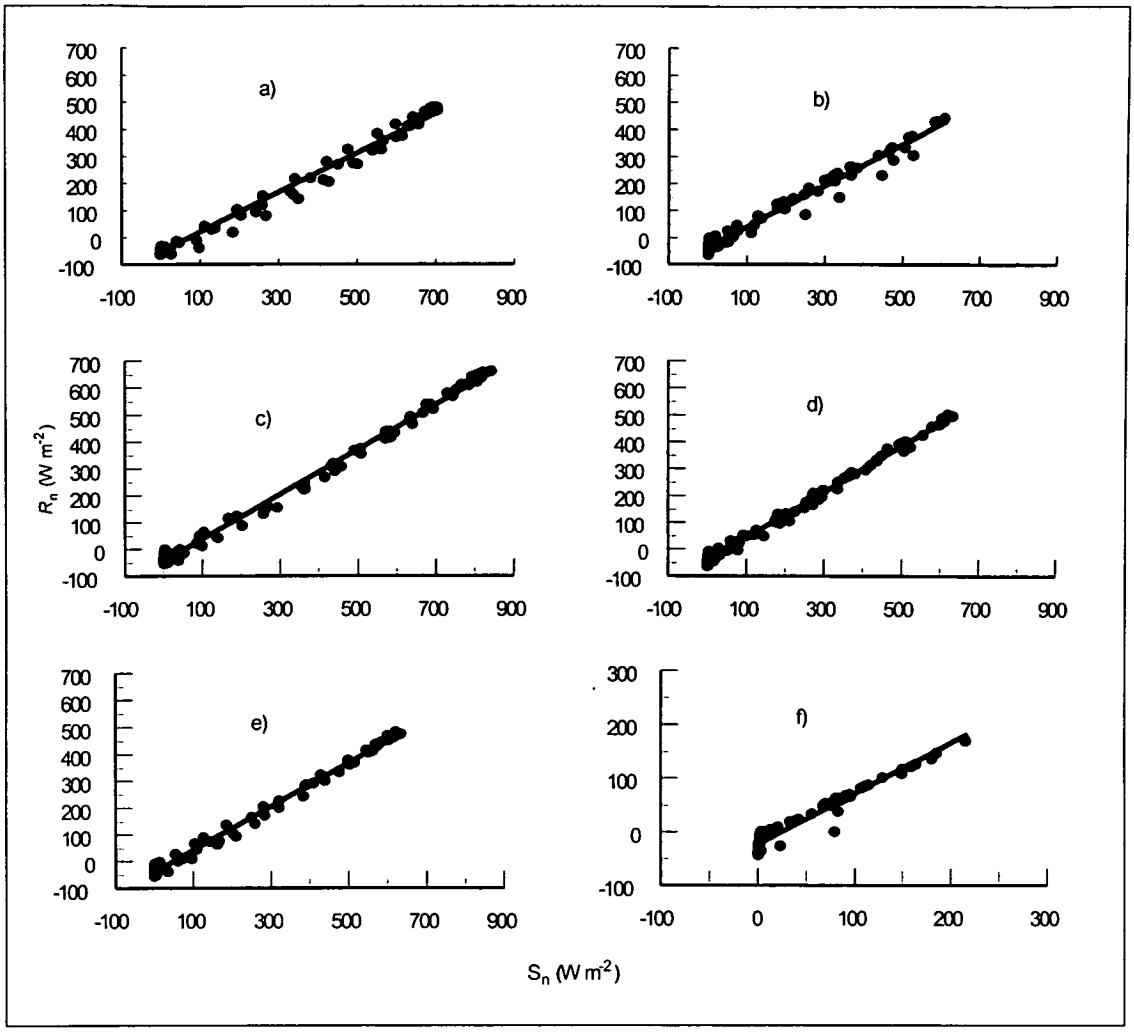

Figure 6-21 Scatterplots of R_n versus S_n during cloudless and cloudy days: a) 27 and 28 March [cloudless], b) 26 March and 1 April [cloudy], c) 6 and 8 June [cloudless], d) 11 and 23 June [cloudy], e) 13 and 14 September [cloudless] and f) 18 and 19 September [cloudy]. Table 6-4 shows the regression parameters.

Date	Cloudless	Offset	Slope	r^2	N
March 27,28	Yes	-14.79±5.49	1.74±0.014	0.994	96
March 26, April 1	No	-4.44±4.82	1.85±0.017	0.992	96
June 6,8	Yes	-2.47±3.52	1.91±0.007	0.999	96
June 11,23	No	-2.26±2.94	1.98±0.009	0.998	96
September 13,14	Yes	-8.59±2.18	1.89±0.007	0.999	96
September 18,19	No	-7.86±0.79	2.11±0.010	0.998	96

Table 6-5 Table of linear regression parameters of Q versus S_{in} during cloudless and cloudy days. The error term is ± 1 standard error. Figure 6-22 shows scatter plots of Q versus S_{in}.

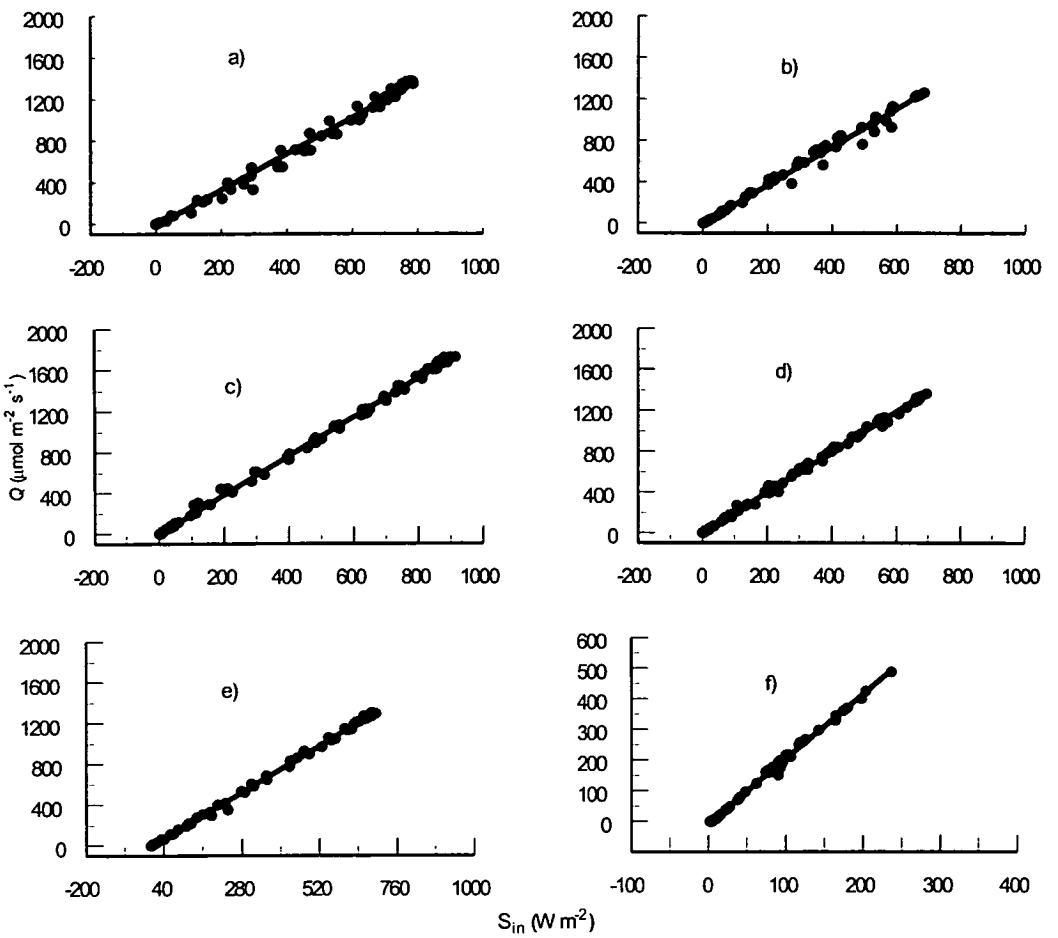

Figure 6-22 Scatter plots of Q versus S_{in} during cloudless and cloudy days: a) 27 and 28 March [cloudless], b) 26 March and 1 April [cloudy], c) 6 and 8 June [cloudless], d) 11 and 23 June [cloudy], e) 13 and 14 September [cloudless] and f) 18 and 19 September [cloudy]. Table 6-5 shows the regression parameters.

The relationship between of Q and S_{in} was also found by linear regression for the same set of cloudless/cloudy days (Table 6-5 and Figure 6-22). The offsets were small and probably represent small calibration differences, but in any case made very little difference to the slope. Q/S_{in} increased on cloudy days and was higher on cloudless June days than on cloudless March or September days. A possible explanation for the increase on cloudy days is that the water absorbs infra-red and thereby increases the fraction of photons to lower frequency quanta (Monteith and Unsworth, 1990).

6.7 Albedo

Values of the albedo (S_{out}/S_{in}) were remarkably consistent throughout the year despite snow cover. Values for the albedo of snow, range from 0.4 to 0.95, depending on how fresh it is, and typical albedos for conifer forest (without snow) are 0.05 to 0.15 (James *et al.*,1976). Figure (6-23) shows the mean albedo for each hour for the months March to November. During the snow-covered months of March, April and October the mid-day albedo was about 0.11 and during the snow free months its value was about 0.09. The stand is very open and snow quickly falls off the trees leaving them uncovered and radiation reflected by the snow is scattered and absorbed by the dark boles and crowns of the trees. These values are typical of boreal conifer forest (Betts and Ball, 1997). In November, however, there were several nights when the atmosphere was very stable and the temperature in the canopy dropped to <-30 °C. On these nights there were heavy frosts and the trees were coated in ice crystals which remained on the trees for many hours, sometimes all day, and caused some half hourly albedos of up to 0.5. This appears to have affected the results in Figure 6-23 for November when the mid-day albedo reached 1.4. The albedo was higher at the beginning and end of the day when the solar elevation is low and the angle of interception angle with the canopy becomes nearer to smaller. However, because of the structure of coniferous forest canopies, this increase in albedo at low solar elevations is much less than with the more uniform, planar surface of crops (Jarvis *et al.*,1976).

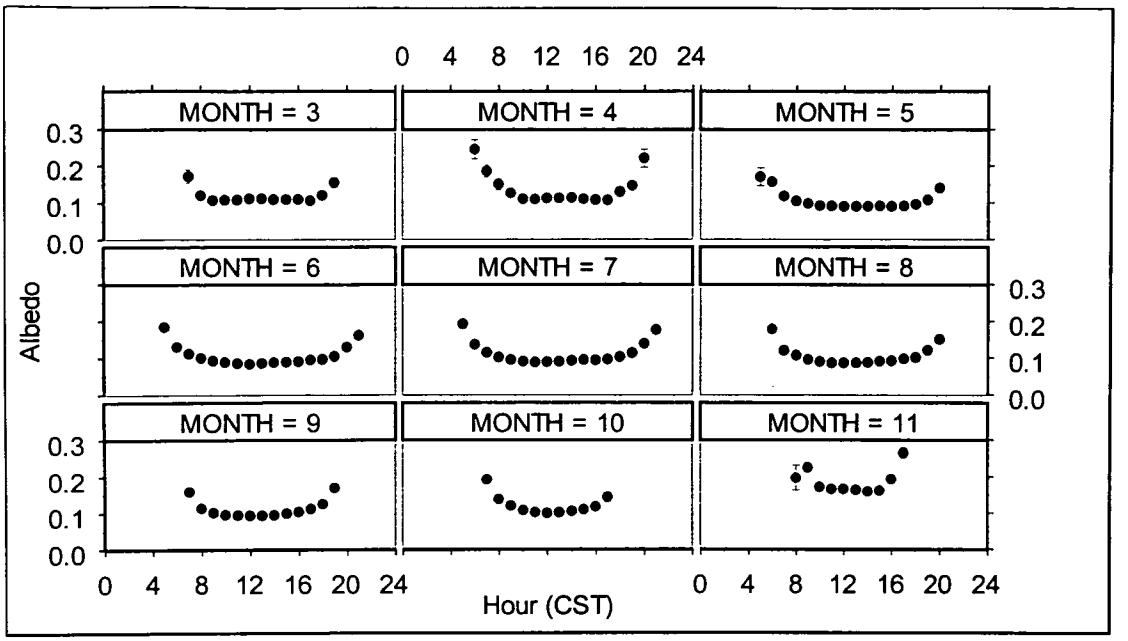

Figure 6-23 Average daily course of albedo, a, for each month. Each point is the mean value for the hour before the time shown. Error bars of ±1 S.E. are plotted but are of the same size as the points.

6.8 Photon flux reflectance

As with the albedo the photon flux reflectance (Q_{out}/Q_{in}) showed little seasonal variation. Midday values in the snow-covered months, were 0.07 in March, 0.05 in April and October. In the summer months of June to September, midday values were 0.04. In March the needles were chlorotic and became less so through April and May. During the same period the photosynthetic apparatus repaired and the quantum efficiency increased (Chapter 5). In October the oldest age class of needles senesced and discoloured. This change in colour of the needles may explain in part the change in photon flux reflectance. The breakdown of chlorophyll pigmentation may be visible from the ground or from satellites (Yoder and Waring, 1994). In November, the midday value was 0.13 and this high value may be caused by hoar frost on the trees. In contrast to the albedo, the canopy photon flux reflectance remained almost constant thoughout the day and did not increase, but often decreased, with lower sun angles. The lower photon flux reflectance than the solar radiation albedo, and the lower sensitivity to low sun angles are the result of the high absorption of the photon wavelengths by the tree crowns irrespective of solar position.

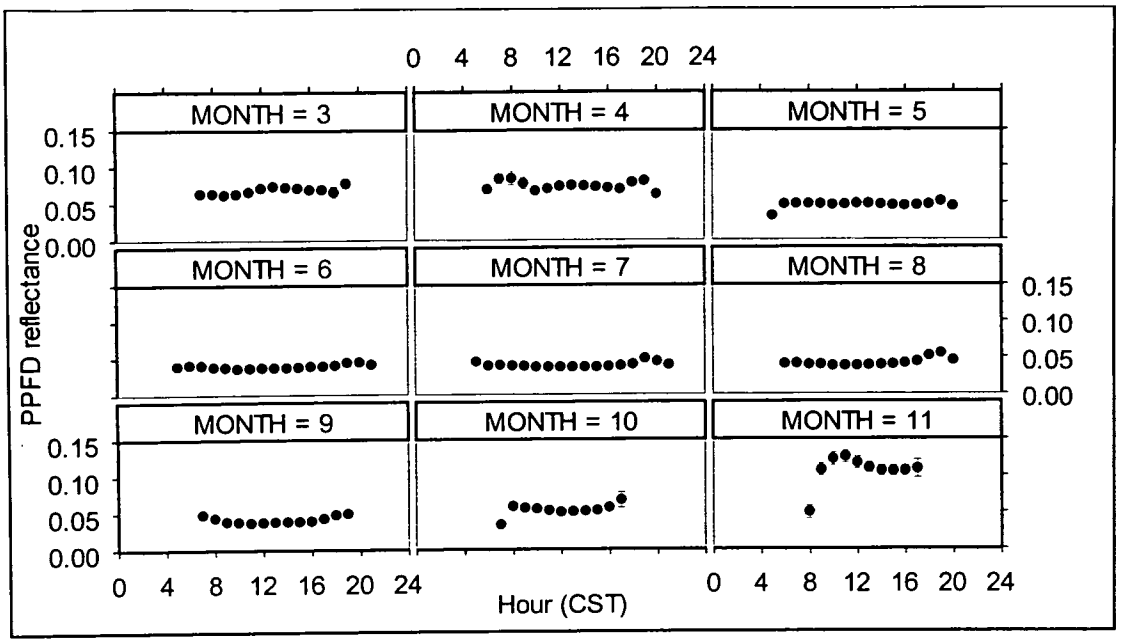

Figure 6-24 Average daily course of PPFD reflectance for each month. Each point is the mean value for the hour before the time shown. Error bars of ±1 S.E. are plotted but are of the same size as the points.

6.9 Summary and conclusions

$H + \lambda E$ comprised 80 to 95 % of R_n but mid-day β varied from 17 in March when the system was frozen to ~1 in July to September and then increased to 6 in November. S_b was the largest component after H and λE accounting for up to 10 % of the energy balance when the stand was warming or cooling at the end and beginning of the day. Soil heat flux account for 5 % at times and S_H and $S_{\lambda E}$ were negligible.

Energy balance closure using all day and night half hour averages was 0.86 $[(H + \lambda E)/(R_n - G - S - B)]$. Using day only half-hour averages, the closure was 0.88 and for night only was 0.28. Excluding half-hour averages when $u_* < 0.4$ m s^{-1} increased closure to 0.90 using day and night data and day only data, and increased to 0.80 for night only data. Errors in the measured energy balance components are unlikely to account for the lost energy flux that may be unmeasured horizontal and/or vertical advection fluxes.

Climatalogical resistance was high during the colder months because D was low, even in March when R_n was relatively high. Minimum canopy resistance decreased from March (~200 s m^{-1}) to October (~50 s m^{-1}) but increased again from October to November (~200 s m^{-1}). After the onset of turbulent mixing aerodynamic resistance was consistently ~10 s $^{m-1}$ until a few hours before sunset. Middle of the day values of the coupling factor, Ω, were ~0.2 or less after the onset of turbulent mixing. This indicates that E was forced by D and controlled by $r_{c,v}$ and was not strongly forced by R_n.

The midday Bowen ratio was 17 in March when temperatures were well below freezing but decreased to ~1 in July as the soil thawed and D increased. During July and August mean midday β was remained ~1 but on some hot days reached ~2. After August, midday β increased to ~6 in November.

Net radiation was 73 % of incoming shortwave radiation or 80 % of net shortwave radiation with offsets of 27.5 and 25.5 W m^{-2} and a root mean squared error of 23.0 and 22.5 W m^{-2} respectively. The offset was decreased by cloud cover. The average relationship between Q and S_{in} was: 1 W m^{-2} = 1.89 μmol m^{-2} s^{-1}. Compared with clear conditions cloud cover increased the value by 5%.

Middle of the day albedo varied little seasonally with extreme values of 0.2 when there was some snow on the trees and to consistent 0.09 when there was no snow or frost present. Photon flux reflectance decreased from 0.07 in March to 0.04 in September and then increased to 0.05 in October. In November albedo and photon flux reflectance were ~0.15 and ~0.10 respectively, possibly influenced by hoar frost or snow on the canopy.

Chapter 7 Conclusions and recommendations

7.1 Introduction

This thesis presents work which is part of BOREAS, an international study to investigate the role of the boreal forest biome in the global carbon and energy cycles. Specifically, a design was produced and implemented for a real-time eddy covariance system and this system was used to measure sensible and latent heat, CO_2, water vapour and momentum fluxes over a key vegetation type of the boreal forest: black spruce. Aspects of the eddy covariance technique and meteorological theory were examined to help interpret the flux measurements. CO_2, water vapour, heat and radiation fluxes were investigated to elucidate the controls of the exchange processes. Both lack of energy balance closure and underestimation of CO_2 fluxes at night indicate unresolved measurement errors.

7.2 Summary and conclusions

7.2.1 Eddy covariance system and measurements

Sonic temperature was derived from the speed of sound. This after correction for vapour pressure provides true temperature. Although the Solent 1012R2 works well down to -40 °C (Peters *et al.*, 1993; Grelle *et al.*, 1994) for wind velocity measurements, below a temperature in the range of 5 °C down to 0 °C depending on the individual anemometer the speed of sound measurement is in error. The calibration below this threshold also varied between the three Solent 1012R2 anemometers used in the investigation. A fifth-order polynomial calibration equation may be used to correct for this problem.

When using closed path eddy covariance systems, especially low power systems where the flow in the sample tube is laminar, the frequency corrections make up a large fraction of the final flux estimate. The Kaimal cospectral models and transfer function for the eddy covariance system fitted well with cospectra calculated for SSA OBS. During the night when wind speeds were low (poor mixing) frequency corrections did not work well, at least in part, because the spectra and cospectra were poorly defined. This is not particularly important as flux estimates when friction

velocity is low at night (0.4 m s^{-1} in this case) are usually discarded (Goulden *et al.*, 1996; Black *et al.*, 1996).

7.2.2 Carbon and water exchange

Night-time CO_2 exchange was underestimated when $u_* < 0.4$ m s^{-1}. There are several possible explanations for this at present unresolved: not measured CO_2 storage in the soil, horizontal advection, or vertical advection (because mean vertical windspeed was not zero).

The annual carbon exchange from 29 November 1995 to 28 November 1996 was -15.47 g C m^{-2}. A confidence interval based on the 95 % confidence interval of the regression equation for respiration is -39.41 to 12.62 g C m^{-2}. Goulden *et al.* (1998) found the annual carbon at the NSA OBS to be 30 ± 50 g C m^{-2} y^{-1} from1994 to 1997. The estimate for evapo-transpiration for the same period was 271 mm.

During the summer months, assimilation followed Q but net CO_2 exchange during the summer was also strongly controlled by temperature as respiration is an exponential function of temperature. Summer CO_2 uptake was strongly reduced by high temperatures. During the winter CO_2 assimilation was negligible and CO_2 was lost by respiration steadily at ~0.76 g C m^{-2} day^{-1}. This winter respiration loss changed little with temperature because the temperatures were at the temperature insensitive end of the response function. The start up of assimilation in the spring and cessation of assimilation in the autumn was controlled by the soil temperature. When the soil was unfrozen assimilation could occur. This sensitivity to spring thaw and winter freeze up may have significant effects on the annual carbon uptake (Goulden *et al.*, 1998). Saturation vapour pressure deficit was found to have a small effect on assimilation at the beginning and end of the summer by reducing assimilation.

7.2.3 Radiation and heat exchange

Sensible and latent heat flux were the largest components of the energy balance accounting for 80 to 95 % of net radiation. However, heat storage in the biomass was the next largest component accounting for up to 10 % and soil heat flux accounted for up to 5 %.

The midday Bowen ratio was 17 in March when temperatures were well below freezing but decreased to ~1 in July as the soil thawed and D increased. During July and August mean midday β was remained ~1 but on some hot days reached ~2. After August, midday β increased to ~6 in November. The seasonal change in the Bowen ratio was controlled by the climatalogical resistance which was high during the colder months because D was low, even in March when R_n was relatively high. During the warmer months middle of the day values of the coupling factor, Ω, were ~0.2 or less after the onset of turbulent mixing indicating that E was forced by D and controlled by $r_{c,v}$ and was not strongly forced by R_n.

Energy balance closure using all half-hour values was 0.86 $[(H + \lambda E)/(R_n - G - S - B)]$. Using day only half-hour averages, the closure was 0.88 and for night only was 0.28. Excluding half-hour averages when $u_* < 0.4$ m s^{-1} increased closure to 0.90 using day and night data and day only data, and increased to 0.80 for night only data.

Middle of the day albedo varied little seasonally compared with agricultural land (Betts and Ball, 1997) with extreme values of 0.2 when there was some snow on the trees and to consistent 0.09 when there was no snow or frost present. Photon flux reflectance decreased from 0.07 in March to 0.04 in September and then increased to 0.05 in October. In November albedo and photon flux reflectance were ~0.15 and ~0.10 respectively, possibly influenced by hoar frost or snow on the canopy.

7.3 Recommendations for further work

7.3.1 Surface mass and heat balance

Both the CO_2 and energy flux measurements indicate that there is apparently unmeasured flux during the night. The lack of energy balance closure in the day indicates that there is also apparently unmeasured energy flux during the day and because the transport for CO_2 and energy fluxes is the same the same might be true for CO_2 as well. The problem with CO_2 flux measurements at night is common (e.g. Black *et al.*, 1996; Goulden *et al.*, 1996, 1997; McCaughey *et al.*, 1997). The problem of systematic underestimation of energy components to balance net radiation is also common (e.g. Lee and Black,1993; Goulden *et al.*, 1996).

Either eddy fluxes are systematically underestimated or the assumptions of zero horizontal flux divergence and zero mean flux of dry air (Webb, Pearman and Leuning, 1980) are invalid or not all storage is measured.

Underestimation of the eddy fluxes may be caused by any part of the data analysis that underestimates the corresponding covariance. Causes of underestimation of high frequency fluctuations (low frequency response) and loss of synchronisation between the covariates by separation of sensors have been discussed in section 4.4. Loss of low frequency fluctuations was also partly discussed in the same section with relation to the transfer function for the ARMA. However, the ARMA introduces a lag that varies with rate of change of the variable (Gash and Culf, 1996). Also, any detrending will remove low frequency variation that is part of the covariance. In the past detrending was necessary for signals from sensors with unstable calibrations but with stable sensors such as the LI-6262 gas analyser detrending may not be necessary. There remains a question though as to whether offsets in signals from anemometers should be detrended.

The storage fluxes of heat are measured but in the case of the CO_2 mass balance storage in the soil air space is not and may account for a substantial amount of CO_2 and this should be investigated, e.g. by measuring soil CO_2 concentration profiles. The process of CO_2 efflux from the soil pores to the free air is also important and worth study when measuring CO_2 fluxes over short periods (e.g. half-hour).

Thom (1975) showed that horizontal advection, though very difficult to measure, could be a significant proportion of the heat balance (and therefore of a mass balance). More recently Lee (1993) showed that non-zero mean vertical windspeed could cause horizontal flux divergence and that this would be more pronounced as the measurement height increased and the vertical concentration gradients increased.

Without advances in the measurement of the mass and heat balance components not generally accounted for, it may not be able to improve the accuracy or precision of surface flux measurements.

7.3.2 Eddy covariance

Vertical eddy fluxes are only part of the heat and mass balance equations and, as discussed under certain conditions, improving the estimation of surface fluxes may require the measurement of other fluxes not generally measured. However, it is still useful to discuss the improvement of eddy covariance systems.

Simplification of the sensor array by integrating the optical path (in case of IRGA) and sonic path in the same volume would eliminate sensor separation, lag times down tubes and attenuation of signal as the gas travelled down the tube. The "traditional" drawback to using open path sensors of airflow obstruction is eliminated by incorporating the IRGA sensor head and with that of the anemometer. Application of WPL corrections to open path data is not arduous or less accurate than for closed path systems. The damping of temperature fluctuations in the sample tube of a closed path system may be viewed as a mechanical application of the WPL correction for temperature fluctuations. For water vapour fluctuations, drying the air before it entered the IRGA has been done when measuring fluxes by the flux gradient method and is the mechanical form of the applying the WPL correction for water vapour fluctuations. This has not been used in eddy covariance because interference with the airflow while drying would further damp the desired concentration fluctuations. WPL corrections are probably usually thought of as being applied in the form derived from H and E but may be applied in the form derived from T_a and vapour pressure directly. Users of the LI-6262 usually calculate CO_2 concentration as if measured in dry air thereby applying a form of WPL correction for water vapour fluctuations and the same calculation could be made for open path CO_2/H_2O sensors. Temperature fluctuations can also be corrected for by calculating concentrations at a given constant temperature in a similar way.

References

Anderson, D.E., Verma, S.B. and Rosenberg, N.J. 1984 Eddy correlation measurements of CO_2, latent heat and sensible heat over a crop surface. *Boundary-Layer Meteorol.* 29, 263-272.

Baldocchi, D.D., Verma, S.B. and Anderson, D.E. 1986 Eddy correlation measurements of carbon dioxide efflux from the forest floor of a deciduous forest. *J. Appl. Ecology* 23, 967-975.

Baldocchi, D.D., Hicks, B.B. and Meyers, T.P. 1988. Measuring biosphere-atmosphere exchanges of biologically related gases with micrometeorological methods. *Ecology* 69, 1331-1340.

Betts, A.K. and Ball, J.H. 1997. Albedo over the boreal forest. *J. Geophys. Research.* 102, 28901-28909.

Black, T.A., Denhartog, G., Neumann, H.H., Blanken, P.D., Yang, P.C., Russell, C., Nesic, Z., Lee, X., Chen, S.G., Staebler, R. and Novak, M.D. 1996. Annual cycles of water vapour and carbon dioxide fluxes in and above a boreal aspen forest. *Global Change Biology* 2, 219-229.

De Bruin, H.A.R., Bink, N.J. and Kroon, L.J.M. 1991. Fluxes in the surface layer under advective conditions. In: T.J. Schmugge and J.C. Andre (Editors), Workshop on land surface evaporation measurement and parameterization. Springer, New York, pp 157-169.

Businger, J.A. 1986. Evaluation of the accuracy with which dry deposition can be measured with current micrometeorological techniques. *J. Climate Appl. Meteor.* 25, 1100-1125.

Cellier, P. and Brunet, Y. 1992. Flux gradient relationships above tall plant canopies. *Agric. For. Meteorol.* 58, 93-117.

Chen, J.M., Rich, P.M., Gower, S.T., Norman, J.J.M. and Plummer, S. 1997. Leaf area index of boreal forests: theory, techniques and measurements. *J. Geophys. Research.* 102, 29429-29443.

Conway, T.J., Tans, P.P., Waterman, L.S. and Thoning, K.W. 1994. Evidence for interannual variability of the carbon-cycle from the national-oceanic-and-atmospheric-administration climate-monitoring- and-diagnostics-laboratory global-air-sampling-network. *J. Geophys. Research.* 99, 22831-22855.

Davis, M.B. and Botkin, D.B. 1985. Sensitivity of cool-temperate forests and their fossil pollen record to rapid temperature-change. *Quaternary Research* 23, 327-340.

Foken, Th. and Wichura, B. 1996. Tools for quality assessment of surface-based flux measurements. *Agric. For. Meteorol.*78, 83-105.

Garratt, J. R. 1992. The Atmospheric Boundary Layer. Cambridge University Press, Cambridge.

Gash, J.H.C. and Culf,A.D. 1996. Applying a linear detrend to eddy correlation data in real time. *Boundary-Layer Meteorol.* 79, 301-306.

Gill Instruments Ltd. 1997. Ultrasonic anemometer 1210R3: User guide. Gill Instruments Ltd., Lymington, Hampshire, UK.

Grace, J., Lloyd, J., Mcintyre, J., Miranda, A. C., Meir, P., Miranda, H. S., Nobre, C., Moncrieff, J., Massheder, J., Malhi, Y., Wright, I. and Gash, J. 1995a Carbon-dioxide uptake by an undisturbed tropical rain-forest in southwest Amazonia, 1992 TO 1993. *Science* 270, 778-780

Grace, J., Lloyd, J., Mcintyre, J., Miranda, A., Meir, P., Miranda, H., Moncrieff, J., Massheder, J., Wright, I. and Gash, J. 1995b Fluxes of carbon-dioxide and water-vapor over an undisturbed tropical forest in south-west Amazonia. *Global Change Biology* Vol.1, 1-12

Grelle, A. and Lindroth, A. 1996. Eddy-correlation system for long-term monitoring of fluxes of heat, water vapour and CO2. *Global Change Biology* 2, 297-307.

Golding, D.L. 1982. Snow accumulation patterns in openings and adjacent forest. Proc. Can. Hydrol. Symp. 1982. National Research Council of Canada, Ottawa. Pp 91-112.

Goulden, M.L. and Crill, P.M. 1997. Automated measurements of CO_2 exchange at the moss surface of a black spruce forest. *Tree Physiology* 17, 537-542.

Goulden, M.L., Munger, J.W., Fan, S.M., Daube, B.C. & Wofsy, S.C. 1996. Measurements of carbon sequestration by long-term eddy covariance: methods and a critical evaluation of accuracy. *Global Change Biology* 2, 169-182.

Goulden, M.L., Daube, B.C., Fan, S.M., Sutton, D.J., Bazzaz, A., Munger, J.W. and Wofsy, S.C. 1997. Physiological responses of a black spruce forest to weather. *J. Geophys. Research.* 102, 28987-28996.

Goulden, M.L., Wofsy, S.C., Harden, J.W., Trumbore, S.E., Crill, P.M., Gower, S.T., Fries, T., Daube, B.C., Fan, S.M., Sutton, D.J., Bazzaz, A. and Munger, J.W. 1998. Sensitivity of boreal forest carbon balance to soil thaw. Science 279, 214-217.

Goutorbe, J.P., Lebel, T., Dolman, A.J., Gash, J.H.C., Kabat, P., Kerr, Y.H., Monteny, B., Prince, S.D., Stricker, J.N.M., Tinga, A. and Wallace, J.S. 1997. An overview of HAPEX-Sahel: A study in climate and desertification. *J.Hydrol.* 189, 4-17.

Gower, S.T., Vogel, J.G., Norman, J.M., Kucharik, C.J., Steele, S.J., and Stow, T.K. 1997. Carbon distribution and aboveground net primary production in aspen,

jack pine, and black spruce stands in Saskatchewan and Manitoba, Canada. *J. Geophys. Research.* 102, 29029-29041

Hale, S.E. 1996. Turbulent transport above and within a black spruce forest canopy. Ph.D.Thesis, IERM, University of Edinburgh.

Halliwell, D.H. and Apps, M.J. 1997. BOReal Ecosystem-Atmosphere Study (BOREAS) biometry and auxiliary sites: overstorey and understorey data. Nat. Resour. Can., Can. For. Serv., Cent., Edmonton, Alberta.

Hodges, G.B. and Smith, E.A. 1997. Intercalibration, objective analysis, intercomparison and synthesis of BOREAS surface net radiation measurements. *J. Geophys. Research.* 102, 28885-28900.

Horst, T.W. and Weil, J.C. 1992. Footprint estimation for scalar measurements in the atmospheric surface layer. *Boundary Layer Meteorol.* 59, 279-296.

Houghton, J.T., Meir Filho, L.G., Bruce, J., Hoesung Lee, Callander, B.A., Haites, E. Harris, N. and Maskell, K. 1995 Climate Change 1994: Radiative forcing of climate change and an evaluation of the IPCC IS92 emission scenarios. Cambridge Univ. Press, Cambridge, U.K.

Houghton, J.T., Jenkins, G.J., and Ephraumus,J.J. 1995 Climate Change: the IPCC Scientific Assessment. Cambridge Univ. Press, Cambridge, U.K..

Jarvis, P.G., James, G.B. and Landsberg, J.J. 1976. Coniferous forest. In *Vegetation and the atmosphere* (Monteith, J.L., ed.), Academic Press, London, pp. 151-170.

Jarvis, P.G. 1994. Resource capture of carbon dioxide by a coniferous forest. In *Resource capture by crops* (Monteith, J.L., Scott, R.K. and Unsworth, M.H., eds.), Nottingham University Press, pp. 351-374.

Jarvis, P.G., Massheder, J.M., Hale, S.E., Moncrieff, J.B., Rayment, M. and Scott, S.L. 1997. Seasonal variation of carbon dioxide, water vapour and energy exchanges of a boreal black spruce forest. *J. Geophys. Research.* 102, 28953-28966.

Jarvis, P.G. and McNaughton, K.G. 1986. Stomatal control of transpiration - scaling up from leaf to region. *Advances in Ecological Research* 15, 1-49.

Jones, H.G. (1992). Plants and microclimate: a quantative approach to plant physiology. Cambridge University Press pp. 1-323.

Jones, P.D. 1994. Hemispheric surface air-temperature variations - a reanalysis and an update to 1993. *J. Climate* 7, 1794-1802.

Kaimal, J.C. and Gaynor, J.E. 1991. Another look at sonic thermometry. *Boundary Layer Meteorol.* 56, 401-410.

Kaimal, J.C. and Finnigan, J.J. 1994. Atmosheric Boundary Layer Flows: Their structure and function. Oxford University Press pp. 1-289.

Kaimal, J.C., Wyngaard, J.C., Izumi, Y., and Cote, O.R. 1972. Spectral characteristics of surface-layer turbulence, Q.J.R. Meteorol. Soc. 98, 563-589.

Kaminsky, K.Z. and Dubayah, R. 1997. Estimation of surface net radiation in the boreal forest and northern prairie from shortwave flux measurements. *J. Geophys. Research.* 102, 29707-29716.

Lavigne, M.B. and Ryan, M.G. 1997. Growth and maintenance respiration rates of aspen, black spruce, and jack pine stems at northern and southern BOREAS sites. *Tree Physiology* 17, 543-551.

Leclerc, M.Y. and Thurtell, GW. 1990. Footprint prediction of scalar fluxes using a Markovian analysis. *Boundary Layer Meteorol.* 52, 247-258.

Lee, X. and Black, T.A. 1993. Atmospheric turbulence within and above a Douglas-fir stand. Part II: Eddy fluxes of sensible heat and water vapour. *Boundary Layer Meteorol.* 64, 369-389.

Lee, X.H. 1998. On micrometeorological observations of surface-air exchange over tall vegetation. *Agric. For. Meteorol.* 91, 39-49.

Lenschow, D.H. and Raupach, M.R. 1991. The attenuation of fluctuations in scalar concentrations through sampling tubes. *J. Geophys. Research.* 96, 5259-5268.

Leuning R.and Judd M.J., 1996. The relative merits of open- and closed-path analysers for measurements of eddy fluxes, *Global Change Biology* 2(3), 241-254.

Leuning, R. and King, K.M. 1992. Comparison of eddy-covariance measurements of CO2 fluxes by open- and closed-path CO2 analysers. *Boundary-Layer Meteorol.* 59, 297-311.

Leuning, R. and Moncrieff J. 1990. Eddy-covariance CO2 flux measurements using open-path and closed-path CO2 analysers - Corrections for analyser water vapour sensitivity and damping of fluctuations in air sampling tubes. *Boundary-Layer Meteorol.* 53, 63-76.

Lloyd, C.R., Shuttleworth, W.J., Gash, J.H.C. and Turner, M. 1984. A microprocessor system for eddy-correlation. *Agric.For.Meteorol.* 33, 67-80.

Massman, W.J. 1991. The attenuation of concentration fluctuations in turbulent-flow through a tube. *J. Geophys. Research.* 96, 5269-5273.

McCracken, P.J. (1993). Turbulent exchange of momentum and carbon dioxide of Sitka spruce plantation. Ph.D. Thesis, University of Edinburgh

McCaughey, J.H. 1985. Energy-balance storage terms in a mature mixed forest at petawawa, ontario - a case-study. *Boundary-Layer Meteorol.* 31, 89-101.

McMillen, R.T. 1986. A BASIC program for eddy correlation in non-simple terrain. *NOAA Technical Memorandum* ERL ARL-147.

McMillen, R.T. 1988. An eddy correlation technique with extended applicability to non-simple terrain. *Boundary-Layer Meteorol.* 43, 231-245.

Mitchell, J.F.B. 1983. The seasonal response of a general-circulation model to changes in co2 and sea temperatures. Quart.J.R.Met.Soc. 109, 113-152.

Moncrieff, J.B., Malhi, Y. and Leuning, R. 1996. The propgation of errors in long-term measurements of land-atmosphere fluxes of carbon and water. *Global Change Biology* 2, 231-240.

Moncrieff, J.B., Massheder, J.M., de Bruin, H., Elbers, J., Friborg, T., Heusinkveld, B., Kabat, P., Scott, S., Soegaard, H. and Verhoef, A. 1997. A system to measure surface fluxes of momentum, sensible heat, water vapour and carbon dioxide. *J.Hydrology* 189, 589-611

Monin, A.S. and Obukov, A.M. 1954. Basic laws of turbulent mixing in the atmosphere near the ground. *Tr. Akad. Nauk. SSSR Geophiz. Inst,* 24, 1963-1987.

Monteith, J.L. 1965. Evaporation and the environment. *Symposium for the Society for Experimental Biology* 19, 205-234.

Monteith, J.L. and Unsworth, M.H. 1990. Principles of environmental physics. 2nd edition, Edward Arnold, London.

Moore, C.J. 1986. Frequency response corrections for eddy correlation systems. *Boundary Layer Meteol.* 37, 17-35.

Nicholls, N., Gruza, G. V., Jouzel, J., Karl, T. R., Ogallo, L. A. & Parker, D. E. 1996 in Climate Change 1995: The Science of Climate Change, eds. Houghton, J. T., Meira Filho, L. G., Callander, B. A., Harris, N., Kattenberg, A. & Maskell, K. Cambridge Univ. Press, Cambridge, U.K., pp. 133-192.

Pattey, E., Desjardins, R.L. and StAmour, G. 1997. Mass and energy exchanges over a black spruce forest during key periods of BOREAS 1994. *J. Geophys. Research.* 102, 28967-28975.

Panofsky, H.A. and Dutton, J.A. 1984. Atmospheric Turbulence: Models and Methods for Engineering Applications. John Wiley and Sons New York, pp. 1-397.

Peters, G., Claussen, M., Lohse, H., Grelle, A., Kornblüh, L. and Fischer, B. 1993. Ice floe station. In: ARKTIS 1993. Ber. Nr. 11 Berichte aus dem ZMK, A: Meteorology. Hamburg University, Department of Meteorology, 262 pp.

Philip, J.R. 1963. The damping of a fluctuating concentration by continuous sampling through a tube. *Australian Journal of Physics* 16, 454-463.

Rannik, U., Vesala, T. and Keskinen, R. 1997. On the damping of temperature fluctuations in a circular tube relevant to the eddy covariance measurement technique. *J. Geophys. Research.* 102, 12789-12794.

Ryan, M.G., Lavigne, M.B. and Gower, S.T. 1997. Annual carbon cost of autotrophic respiration in boreal forest ecosystems in relation to species and climate. *J. Geophys. Research.* 102, 28871-28883.

Rayment, M. (1998). Carbon and water fluxes in a boreal forest ecosystem. Ph.D. Thesis, University of Edinburgh

Vallentini, R., Scarascia Mugnozza, G. E., de Angelis, P. and Bimbi, R. 1991 An experimental test of the eddy correlation technique over a Mediterranean macchia canopy. *Plant, Cell and Environment* 14, 987-994.

Scheup PH, Leclerc MY, MacPherson JI, MacPherson,J.I.and Desjardins,R.L. 1990. Footprint prediction of scalar fluxes from analytical solutions of the diffusion equation. *Boundary Layer Meteorol.* 50,355-373.

Sellers, P., Hall, F., Margolis, H., Kelly, B., Baldocchi, D., Denhartog, G., Cihlar, J., Ryan, M.G., Goodison, B., Crill, P., Ranson, K.J., Lettenmaier, D. and Wickland, D.E. 1995. The boreal ecosystem-atmosphere study (Boreas) - An overview and early results from the 1994 field year. *Bulletin Of The American Meteorological Society* 76, 1549-1577.

Schotanus, P., Nieuwstadt, F.T.M. and Debruin, H.A.R. 1983. Temperature-measurement with a sonic anemometer and its application to heat and moisture fluxes. *Boundary-Layer Meteorol.* 26, 81-93.

Shuttleworth, W.J. 1980. Corrections for the effect of background concentration change and sensor drift in real-time eddy correlation systems. *Boundary-Layer Meteorology* 42, 167-180.

Smith, E.A., Hodges, G.B., Bacrania, M., Cooper, H.J., Owens, M.A. Chappell, R. and Kincannon, W. 1997. BOREAS Net Radiometer Engineering Study. Report. Florida State University, Tallahassee, FL, USA.

Solomon, A.M. 1985. Computer-aided reconstruction of late-quaternary landscape dynamics. *Annual Review Of Ecology And Systematics* 16, 63-84.

Stull, R.B. 1988. An introduction to boundary layer meteorology. Kluwer Academic Publishers, London.

Swinbank, W.C. 1951. The measurement of vertical transfer of heat and water vapour by eddies in the lower atmosphere. *J. Meteorol.* 8,135-145.

Tans, P.P., Fung, I.Y. and Takahashi, T. 1990. Observational constraints on the global atmospheric CO2 budget. *Science* 247, 1431-1438.

Taylor, G.I. 1938. The spectrum of turbulence. *Proc. Royal Society of London* A164, 476-490.

Taylor, G.I. 1953. Dispersion of soluble matter in solvent flowing slowly through a tube. *Proc. Royal Society of London, A* 219, 186-203.

Taylor, G.I. 1954. The dispersion of matter in turbulent flow through a pipe. *Proceedings of the Royal Society of London A* 223, 446-468.

Thom, A.S. 1975. Momentum, mass and heat exchange of plant communities. In *Vegetation and the atmosphere Vol. 1* (Monteith, J.L., ed.), Academic Press, London, New York and San Francisco, pp. 57-110.

Tylan General Corp. 1992. Instruction manual FC2900 Series: Mass Flow Controllers. Tylan, Torrance, CA, USA.

Valentini, R., Scarascia Mugnozza, G.E., Angelis, P.d. and Bimbi, R. 1991. An experimental test of the eddy correlation technique over a Mediterranean canopy. *Plant,Cell and Environment* 14, 987-994.

Vickers, D. and Mahrt, L. 1996. Quality control and flux sampling problems for tower and aircraft data. *J. Atmosph. Ocean Technolog.* 14, 512-526.

Webb, E.K., Pearman, G.I. and Leuning R., 1980. Correction of flux measurements for density effects due to heat and water vapour transfer. *Q.J.R.Meteorol.* 106, 85 -100.

Wofsy, S.C., Goulden, M.L., Munger, J.W., Fan, S.M., Bakwin, P.S., Daube, B.C., Bassow, S.L. and Bazzaz, F.A. 1993. Net exchange of co2 in a midlatitude forest. *Science* 260, 1314-1317.

Wyngaard, J.C. 1988. Flow-distortion effects on scalar flux measurements in the surface layer: implications for sensor design. *Boundary Layer Meteorology* 42,19-26.

Yoder, B.J. and Waring, R.H. 1994. The normalized difference vegetation index of small douglas-fir canopies with varying chlorophyll concentrations. *Remote Sensing of Environment* 49, 81-91.

Zeller, K., Massam, W. J., Stocker, D., Fox, D. G., Stedman, D., and Hazlett, D. 1989. Initial results from the Pawnee eddy correlation system for dry deposition research. US Dept. Agric. (Forest Service), Research paper RM-282, Fort Collins, Colarado 80526.